

Atomic Force Microscopy: In Sickness and in Health

Lead Guest Editor: Andreas Stylianou

Guest Editors: Stylianos Vasileios Kontomaris, Colin Grant,
and Eleni Alexandratou





Atomic Force Microscopy: In Sickness and in Health

Scanning

Atomic Force Microscopy: In Sickness and in Health

Lead Guest Editor: Andreas Stylianou

Guest Editors: Stylianos Vasileios Kontomaris, Colin Grant,
and Eleni Alexandratou



Copyright © 2019 Hindawi. All rights reserved.

This is a special issue published in "Scanning." All articles are open access articles distributed under the Creative Commons Attribution License, which permits unrestricted use, distribution, and reproduction in any medium, provided the original work is properly cited.

Editorial Board


Masayuki Abe, Japan
David Alsteens, Belgium
Igor Altfeder, USA
Jose Alvarez, France
Richard Arinero, France
Renato Buzio, Italy
Ovidiu Cretu, Japan
Nicolas Delorme, France
Hendrix Demers, Canada
John R. Dutcher, Canada

Jonathan R. Felts, USA
Marina I. Giannotti, Spain
Sacha Gómez, Spain
Federico Grillo, UK
Anton V. Ievlev, USA
Berndt Koslowski, Germany
Jessem Landoulsi, France
Emanuela Margapoti, Brazil
Alessio Morelli, UK
Daniele Passeri, Italy

Andrea Picone, Italy
Jason L. Pitters, Canada
Michela Relucenti, Italy
Damien Riedel, France
Francesco Ruffino, Italy
Steven R. Schofield, UK
Christian Teichert, Austria
Marilena Vivona, UK
Kislon Voitchovsky, UK
Masamichi Yoshimura, Japan

Contents

Atomic Force Microscopy: In Sickness and in Health

Stylianos-Vasileios Kontomaris, Colin Grant, Eleni Alexandratou, and Andreas Stylianou 
Editorial (2 pages), Article ID 6149247, Volume 2019 (2019)

Atomic Force Microscopy on Biological Materials Related to Pathological Conditions

Andreas Stylianou , Stylianos-Vasileios Kontomaris, Colin Grant, and Eleni Alexandratou
Review Article (25 pages), Article ID 8452851, Volume 2019 (2019)

Conformational Distortions of the Red Blood Cell Spectrin Matrix Nanostructure in Response to Temperature Changes *In Vitro*

Elena Kozlova , Aleksandr Chernysh, Viktoria Sergunova, Ekaterina Manchenko, Viktor Moroz, and Aleksandr Kozlov
Research Article (12 pages), Article ID 8218912, Volume 2019 (2019)


Effect of Fe₃O₄ Nanoparticles on Mixed POPC/DPPC Monolayers at Air-Water Interface

Zhuangwei Xu, Changchun Hao , Bin Xie, and Runguang Sun
Research Article (9 pages), Article ID 5712937, Volume 2019 (2019)

Nonlinear Biomechanical Characteristics of Deep Deformation of Native RBC Membranes in Normal State and under Modifier Action

Elena Kozlova , Aleksandr Chernysh, Ekaterina Manchenko, Viktoria Sergunova, and Viktor Moroz
Research Article (13 pages), Article ID 1810585, Volume 2018 (2019)

AFM Characterization of the Internal Mammary Artery as a Novel Target for Arterial Stiffening

Zhuo Chang, Paolo Paoletti, Maria Lyck Hansen, Hans Christian Beck, Po-Yu Chen, Lars Melholt Rasmussen, and Riaz Akhtar 
Research Article (10 pages), Article ID 6340425, Volume 2018 (2019)

Editorial

Atomic Force Microscopy: In Sickness and in Health

**Stylianos-Vasileios Kontomaris,^{1,2} Colin Grant,³ Eleni Alexandratou,⁴
and Andreas Stylianou ⁵**

¹*Mobile Radio Communications Laboratory, School of Electrical and Computer Engineering, National Technical University of Athens, Iroon Polytechniou, Athens 15780, Greece*

²*Athens Metropolitan College, Sorou 74, Marousi 15125, Greece*

³*Hitachi High-Technologies Europe, Techspace One, Keckwick Lane, Warrington WA4 4AB, UK*

⁴*Biomedical Optics and Applied Biophysics Laboratory, School of Electrical and Computer Engineering, National Technical University of Athens, Iroon Polytechniou, Athens 15780, Greece*

⁵*Cancer Biophysics Laboratory, Department of Mechanical and Manufacturing Engineering, University of Cyprus, Nicosia 2238, Cyprus*

Correspondence should be addressed to Andreas Stylianou; stylianou.c.andreas.1@ucy.ac.cy

Received 25 March 2019; Accepted 26 March 2019; Published 14 May 2019

Copyright © 2019 Stylianos-Vasileios Kontomaris et al. This is an open access article distributed under the Creative Commons Attribution License, which permits unrestricted use, distribution, and reproduction in any medium, provided the original work is properly cited.

During the last decades, Atomic Force Microscopy (AFM) has become a powerful tool able to provide quantitative and qualitative information regarding many pathological issues, based on the determination of proteins', cells', and tissues' mechanical and topographical properties at the nanoscale. This special issue is aimed at exhibiting the latest research achievements, findings, and ideas in the field of AFM research regarding biological materials and pathological conditions. In order to provide a clear introduction and guideline to new researchers into this field, A. Stylianou et al. (2019) offered an overview regarding the basic principles of AFM and its applications in biology and medicine. The imaging and nanomechanical characterization abilities were briefly presented followed by a complete presentation of applications related to pathological conditions such as osteoarthritis, Alzheimer's disease, and cancer. In addition, the ability to provide useful information regarding proteins and viruses was discussed. Among the original researches reported in this special issue, Z. Chang et al. (2019) explored the nanoscale elastic modulus of the tunica media of the internal mammary artery (IMA) in hydrated and dehydrated conditions from the patients with low and high arterial stiffening, as assessed in vivo by carotid-femoral pulse wave

velocity (PWV). Their research was conducted using the AFM PeakForce quantitative nanomechanical mapping (QNM) technique and revealed the utility of AFM methods for arterial stiffening studies.

In addition, E. Kozlova et al. (2019a) used AFM techniques in order to test the ability of membranes of native human red blood cells (RBCs) to bend into the cell to a depth comparable in size with physiological deformations. The significance of the aforementioned investigation is crucial since the results of the work can be used in clinical practice, in assessing the quality of stored donor blood for transfusion, in biophysical studies of RBC properties. Also, E. Kozlova et al. (2019b) used AFM to study the nanostructure of the spectrin matrix of RBCs in response to temperature changes. Their results can be used as the basis for understanding how an increase in body temperature can affect RBC membrane nanostructure, morphology, and, ultimately, blood rheology.

Furthermore, a significant contribution regarding the applications of AFM in the drug industry was performed by Z. Xu et al. (2019) who contributed towards the clarification of the mechanism of action between Fe₃O₄ NPs and biological membranes. Their contribution could

probably have a potential application in designing the targeted drug liposomes.

In conclusion, the objectives of the special issue have been reached in terms of advancing the current state of the art of AFM applications in sickness and in health. Several basic problems in these areas were well addressed, and most of the proposed contributions exhibited very promising results that outperform existing studies in the community.

Conflicts of Interest

The authors declare that there is no conflict of interest regarding the publication of this article.

Acknowledgments

We would like to express our thanks to all the authors who submitted their original works to this special issue and to all the reviewers who helped us ensure the quality of the papers.

Stylios-Vasileios Kontomaris
Colin Grant
Eleni Alexandratou
Andreas Stylianos

Review Article

Atomic Force Microscopy on Biological Materials Related to Pathological Conditions

Andreas Stylianou ¹, Stylianos-Vasileios Kontomaris,^{2,3} Colin Grant,⁴
and Eleni Alexandratou⁵

¹*Cancer Biophysics Laboratory, Department of Mechanical and Manufacturing Engineering, University of Cyprus, Nicosia 2238, Cyprus*

²*Mobile Radio Communications Laboratory, School of Electrical and Computer Engineering, National Technical University of Athens, Iroon Polytechniou, Athens 15780, Greece*

³*Athens Metropolitan College, Sorou 74, Marousi 15125, Greece*

⁴*Hitachi High-Technologies Europe, Techspace One, Keckwick Lane, Warrington WA4 4AB, UK*

⁵*Biomedical Optics and Applied Biophysics Laboratory, School of Electrical and Computer Engineering, National Technical University of Athens, Iroon Polytechniou, Athens 15780, Greece*

Correspondence should be addressed to Andreas Stylianou; stylianou.c.andreas.1@ucy.ac.cy

Received 7 December 2018; Revised 23 February 2019; Accepted 7 March 2019; Published 12 May 2019

Academic Editor: Daniele Passeri

Copyright © 2019 Andreas Stylianou et al. This is an open access article distributed under the Creative Commons Attribution License, which permits unrestricted use, distribution, and reproduction in any medium, provided the original work is properly cited.

Atomic force microscopy (AFM) is an easy-to-use, powerful, high-resolution microscope that allows the user to image any surface and under any aqueous condition. AFM has been used in the investigation of the structural and mechanical properties of a wide range of biological matters including biomolecules, biomaterials, cells, and tissues. It provides the capacity to acquire high-resolution images of biosamples at the nanoscale and allows at readily carrying out mechanical characterization. The capacity of AFM to image and interact with surfaces, under physiologically relevant conditions, is of great importance for realistic and accurate medical and pharmaceutical applications. The aim of this paper is to review recent trends of the use of AFM on biological materials related to health and sickness. First, we present AFM components and its different imaging modes and we continue with combined imaging and coupled AFM systems. Then, we discuss the use of AFM to nanocharacterize collagen, the major fibrous protein of the human body, which has been correlated with many pathological conditions. In the next section, AFM nanolevel surface characterization as a tool to detect possible pathological conditions such as osteoarthritis and cancer is presented. Finally, we demonstrate the use of AFM for studying other pathological conditions, such as Alzheimer's disease and human immunodeficiency virus (HIV), through the investigation of amyloid fibrils and viruses, respectively. Consequently, AFM stands out as the ideal research instrument for exploring the detection of pathological conditions even at very early stages, making it very attractive in the area of bio- and nanomedicine.

1. Introduction

Atomic force microscopy (AFM) belongs to the scanning probe microscopy (SPM) family and was developed following on from the scanning tunnelling microscopy (STM), which was awarded the 1986 Nobel Prize in Physics. AFM is a SPM that records interactions between a sharp probe (the AFM tip) at the end of a small cantilever and the sample surface. Since its invention in the 1980s, it has become a

fundamental technique in the fields of surface science. AFM has several advantages over the other microscopic techniques, such as scanning and transmission electron microscopy (SEM and TEM) and optical microscopy (including fluorescent and confocal laser scanning microscopy). First of all, AFM provides quantifiable and accurate surface height information, down to the Angstrom level—while other microscopes can give topographical contrast, they cannot provide three-dimensional topographies. Measurements

and images captured by AFM can be made in air, aqueous, or vacuum conditions at a range of temperatures. Plus, the sample preparations are considerably easier than those used for TEM. After image acquisition, the AFM user can perform mechanical/electrical/magnetic property characterization of sample surface, offering a combination of qualitative and quantitative information [1]. AFM is characterized as a non-destructive tool that can operate under different conditions (air and liquid) since it requires only the basic sample preparation (e.g., does not require dehydration, labeling with fluorescent dyes or antibodies, or surface coating) [2–5].

AFM was developed in 1986 by Binnig and colleagues [6] and commercial AFMs began to appear in the early 1990s [7]. Since its invention, it has rapidly become a popular method for high-resolution nanoscale imaging and mechanical property characterization of a broad range of samples, especially biological materials [3, 8]. The key requirement for AFM imaging is the probe, a sharp tip mounted on a cantilever (Figure 1). A huge range of tip shapes and geometries are commercially available along with a range of cantilever spring constants (0.001 to 2000 N/m) and cantilever coatings that can allow imaging of delicate soft matter without causing damage or even make indentations in glass.

1.1. Force versus Distance Curves. In this section, the applied forces during the interaction between the AFM tip and the sample’s surface will be presented. These forces are attractive or repulsive depending on the distance between the AFM tip and the sample (Figure 2(a)). More specifically, if the above-mentioned distance is big enough, the resultant force is attractive (van der Waals force) [9]. On the contrary, for small distances, the resultant force is repulsive due to the overlapping of electron orbitals between the tip and sample [9]. The aforementioned forces can be approximated using the Lennard–Jones potential (Figure 2(b)) [10]:

$$V(d) = 4V_m \left[\left(\frac{d_m}{d} \right)^{12} - \left(\frac{d_m}{d} \right)^6 \right], \quad (1)$$

where $V(d)$ and d are the intermolecular potential and the distance between the two atoms or molecules, respectively; V_m is the well depth (a measure of how much the two particles attract each other); and d_m is the distance at which $V = 0$.

As it is presented in Figure 2(a), when the distance between the AFM tip and the sample’s surface is equal to d_{eq} (where d_{eq} is the equilibrium distance), the resultant force on the tip is zero. In addition, in the case that $d > d_{eq}$, the resultant force is attractive (negative net force, $F_T = F_R - F_A < 0$, where F_R is the repulsive force, F_A the attractive force, and F_T the total force on the tip). On the contrary, in the case that $d < d_{eq}$, the resultant force is repulsive (positive net force, $F_T = F_R - F_A > 0$).

1.2. Applied Forces in the AFM Operation Modes. The categorization of the imaging modes is based on the type of the applied forces on the sample. More specifically, in the contact mode, the tip is always in contact with the sample and the resultant force is repulsive. On the contrary, in the

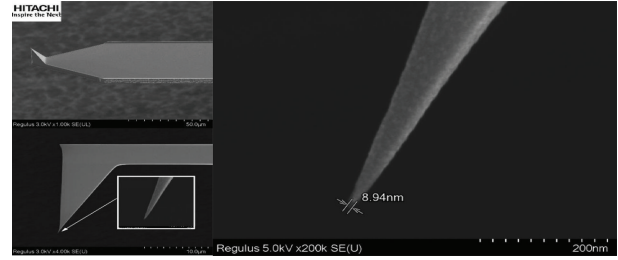


FIGURE 1: AFM tip. SEM images (Hitachi Regulus SU 8230) of an Olympus AC160 AFM probe, with a measured tip diameter of 9 nm (unpublished data obtained by Colin Grant).

noncontact mode, the tip is never in contact with the sample’s surface; thus, the resultant force is attractive. In the tapping mode, the resultant force can be attractive or repulsive since the tip alternately moves toward to or away from the sample’s surface. Last but not least, in the force mode (in which the sample’s mechanical properties must be tested), the sample is moving toward the tip; hence, the net force is initially attractive and then repulsive. The selection of an AFM imaging mode depends on the characteristics of the sample that must be tested. For example, for a nonbiological sample, the contact mode is preferable due to the fact that there is no possibility to cause permanent damage to the sample. In the case of very soft biological samples, the noncontact mode seems to be the preferred choice. However, it presents severe limitations (e.g., it must be applied in a high vacuum environment) [11, 12], and as a result, the tapping mode is mostly used for imaging soft biological samples. In Figure 3, the total force with respect to distance (between the tip and the sample) is presented. The blue box presents the range of interaction forces in the contact region, and the green and grey boxes the range of interaction forces in the noncontact region and the intermittent region (tapping mode), respectively.

The AFM instrument itself consists of a laser beam aligned to the back of a cantilever, which is then reflected onto a position-sensitive detector (Figure 4(a)). The accurate movement of the tip over the surface is achieved with piezoelectric elements in the x, y, z frame. The probe scans over the sample surface where any changes of the laser spot position on the detector are recorded and acted upon by feedback electronics, resulting in the accurate representation of the sample surface (Figure 4(a)).

One of the unique features of AFM is that once the user has found a region of interest or interesting feature, the cantilever tip can be used to apply a user-determined force on the sample. In AFM force spectroscopy, with careful calibration of cantilever spring constant, applied forces can be used to compress the sample, generating a force vs. indentation data. By using the AFM nanoindentation procedure [13–15], the stiffness/elasticity of the specimen can be recorded and Young’s modulus maps of the sample’s surface can be generated [16–20]. Additionally, further research is ongoing for the improvement of the existing mathematical models that are used for the acquisition of quantitative data from AFM modes [21].

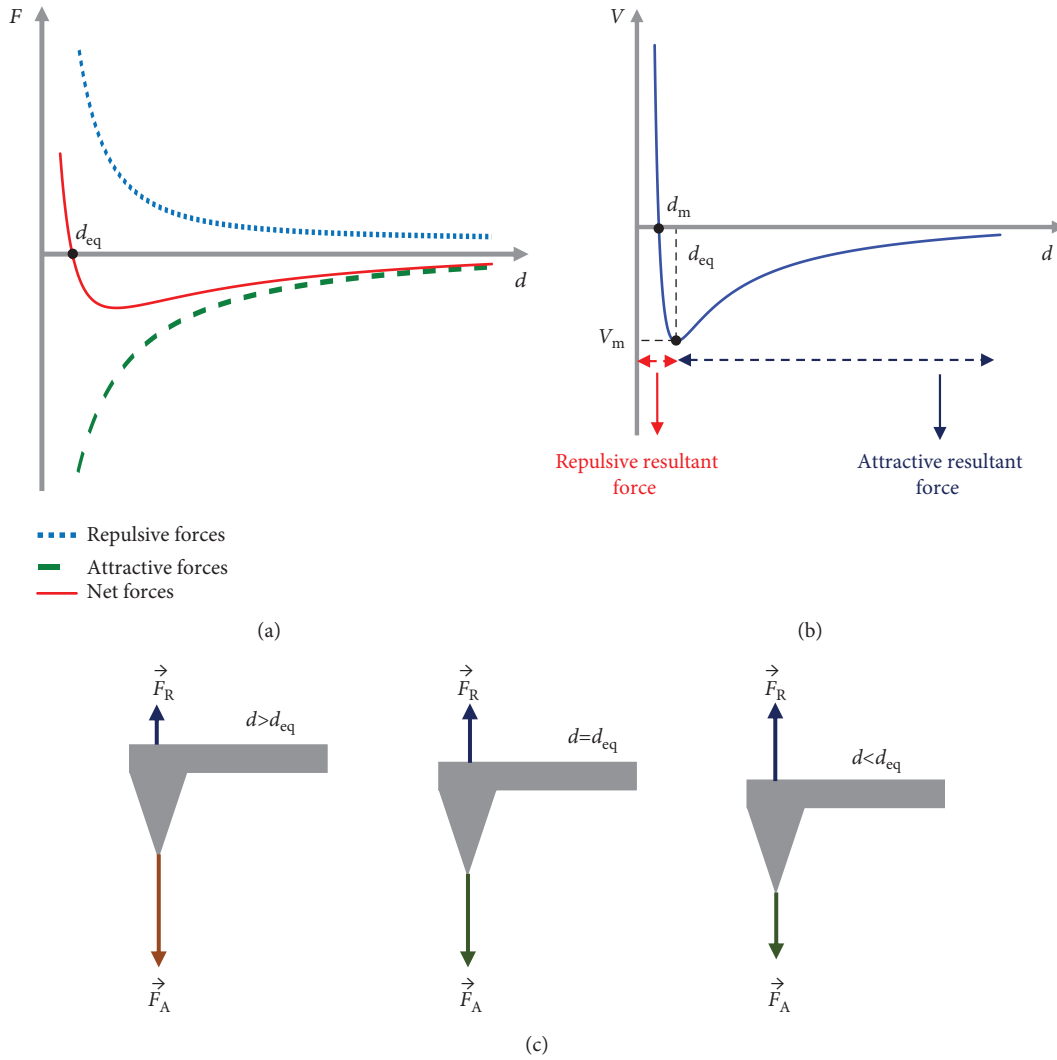


FIGURE 2: (a) Force-distance curves. Interaction forces versus distance between the tip and the sample’s surface. (b) The Lennard–Jones potential. If $d > d_{eq}$, the resultant force is attractive, and if $d < d_{eq}$, the resultant force is repulsive. In the case that $d = d_{eq}$, the resultant force is zero. (c) Repulsive and attractive forces on the tip. Forces applied on the AFM tip in three different regions.

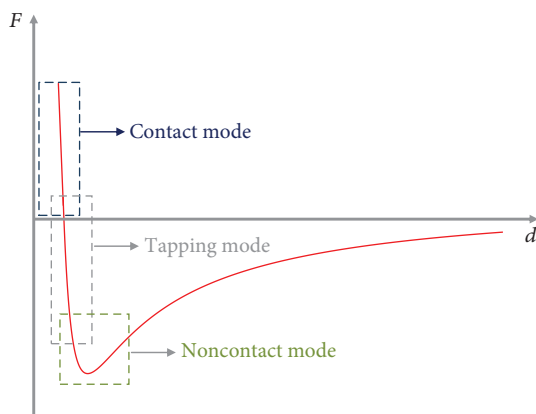


FIGURE 3: Force versus distance: the blue box represents the range of interaction forces in the contact mode (repulsive net force). The grey box and the green box represent the range of the interaction forces in the intermittent and in the noncontact regions, respectively.

2. Atomic Force Microscopy: Imaging Modes

Many other microscopes have different kinds of “modes” in order to extract more information about a surface. For example, SEM utilize secondary or backscattered electrons in order to image and provide information on topography and chemical composition, respectively. Optical microscopes can operate in a brightfield, darkfield, polarized, or phase contrast mode, depending on the optics that are used. Similarly, the AFM can operate in a number of different modes (Figures 4(b)–4(g)).

In the *tapping mode* (also known as intermittent mode, dynamic contact mode, and AC mode), the cantilever is tuned to its resonant frequency at a measured amplitude (Figure 4(b)); any changes in the oscillation amplitude are recorded as the tip scans the surface. Imaging with this dynamic mode is considered very gentle on sample surfaces, capable of high resolution, and almost all lateral forces are eliminated [3, 22].

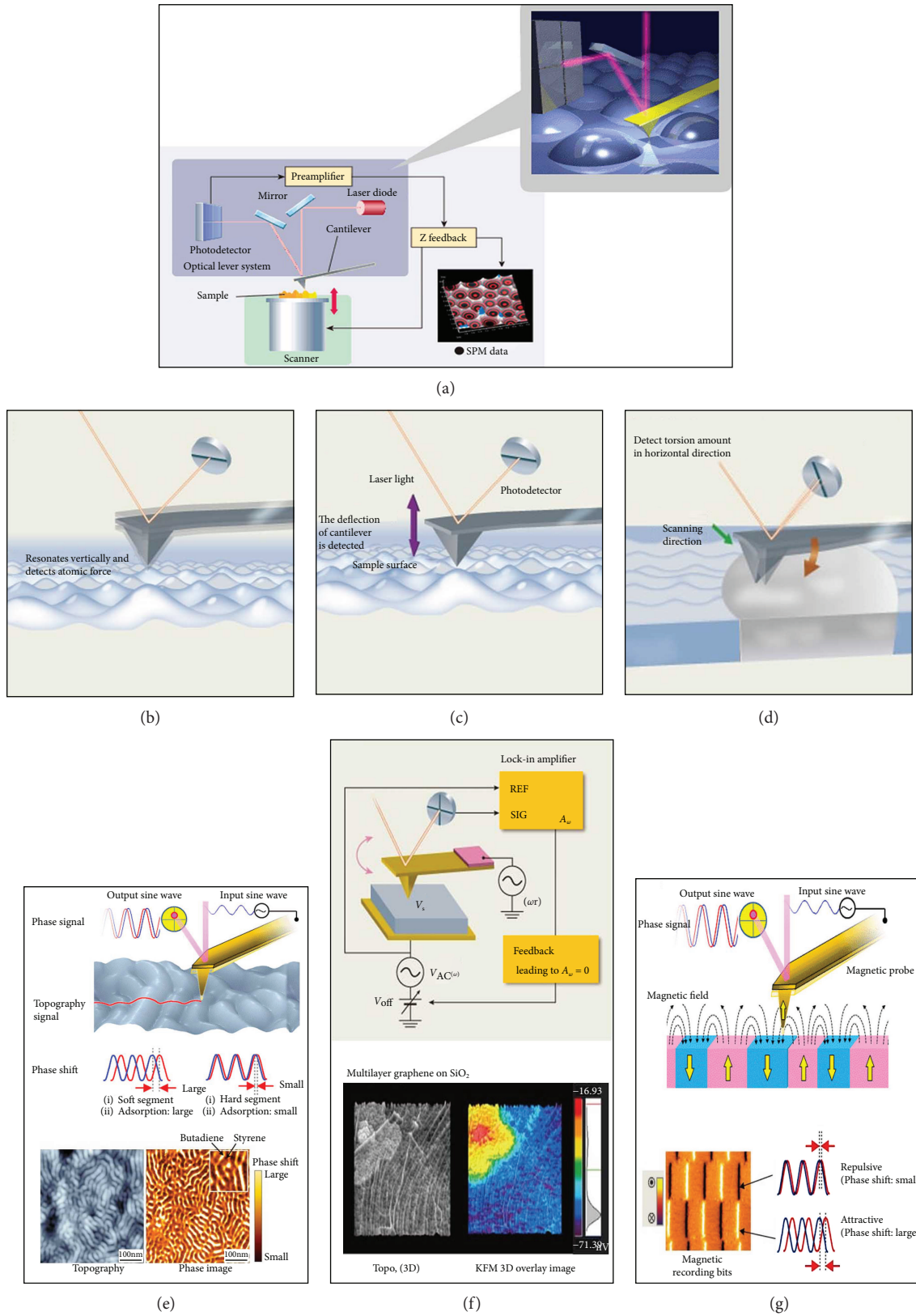


FIGURE 4: AFM working principles and modes: (a) generalized schematic of AFM of cantilever with the laser reflecting onto the photodetector. (b) Tapping/dynamic mode. (c) Contact mode. (d) Friction/lateral mode. (e) Phase imaging from dynamic mode, where the contrast (butadiene/styrene blend) relates to surface properties. (f) Kelvin probe electrical imaging; contrast shows surface potential (work function) of a graphene flake on SiO_2 substrate. (g) Magnetic mode imaging, where a magnetic coated cantilever scans just above the surface and the phase shift relates to attraction/repulsion of magnetic domains (images courtesy of Hitachi High Technology, Tokyo, Japan).

In the *contact mode*, the tip is always in contact with the sample surface at a user-determined constant force (Figure 4(c)). Here, the user can track rougher, stiffer surfaces better and faster than the tapping mode. *Friction mode* imaging (Figure 4(d)) is a form of static mode (contact mode). This mode is appropriate for measuring the friction of a surface as the side to side twisting of the cantilever by a torque, measured as the probe raster scans along the surface. In the frictional force mode, here, the torsional changes (frictional features) in the photodetector are recorded simultaneously with the vertical changes (topographic features). Most AFM users will use this to gain qualitative frictional contrast of their surfaces; however, with appropriate calibration of the lateral cantilever spring constant [23], a surface frictional coefficient can be calculated.

During the tapping mode, simultaneously with topography images, phase images can be acquired [7]. In *phase imaging*, the system monitors the phase lag between the signal that drives the cantilever oscillation and its output signal (Figure 4(e)). Phase images can be used for assessing variations in composition, adhesion, and viscoelastic properties of surfaces [20, 24].

Other tapping mode-based characterizations include the *Kelvin probe* (Figure 4(f)) and *magnetic mode* (Figure 4(g)). Kelvin force microscopy (KFM) is one among a number of electrical characterizations that AFM can carry out. In this technique, a contact potential difference is measured between a conductive AFM probe and the sample of interest. This contact potential difference is negated by the application of a direct external bias of the same magnitude; which is then equal to the difference in work function between the tip and sample [25]. Magnetic imaging mode can image magnetic domain structures of a surface when a magnetic-coated cantilever scans the surface [26]. Here, the oscillating probe first scans the surface to get topographical features, but then, the probe elevates off the surface by a small distance and the attraction/repulsion is recorded.

AFM can also operate in a *noncontact mode* where the AFM tip does not touch at all the sample surface [27], but this mode is not frequently used for biological sample characterization.

In the *mechanical mapping mode*, the AFM measures the sample stiffness, in terms of Young's modulus values, through the nanoindentation technique. In AFM nanoindentation, the AFM collects indentation-force curves on the sample of interest while these curves are fitted using linear-elastic contact mechanical models, such as the Hertz model, in order to estimate Young's modulus [7]. It should be noted that the selection of the contact mechanics models to transform force-indentation curves into elastic moduli is the most fundamental and longstanding issue [28]. Modulus maps can then be formed by indenting in an organized array over a surface [16]. This technique can be very slow, as for example, a 64×64 -pixel modulus map, with one indentation per second would take over an hour. Most AFM manufacturers have developed fast force mapping modes to speed up this procedure where indents are taken at kHz magnitude, meaning a 512×512 mechanical map can be taken in minutes. However, at this level of loading rate, the modulus results

lack accuracy when indenting viscoelastic time-dependent materials. Further, the tip radius, which is vitally important for the modulus calculation, will be increasing during the imaging procedure.

To avoid this tip blunting effect during nanoindentation mapping, new mechanical imaging techniques have emerged. *Contact resonance* is a very useful mechanical mapping technique for materials ranging between 50 MPa and 200 GPa and consists of oscillating the samples, while undertaking a contact mode image. To date, this technique has been used only in few biological materials (for instance, for bone material [29]) although this technique does work well in air or under aqueous conditions [30].

In the *multifrequency*, AFM employs the detection of multiple cantilever frequencies (higher harmonics and/or higher flexural eigenmodes) which provides information concerning the tip-sample nonlinearity [31, 32]. Multiharmonic mode uses alterations in the amplitude, the phase of the oscillator, and other relevant harmonics in order to provide quantitative local property maps [30, 33]. Multiharmonic, like bimodal AFM which requires the simultaneous excitation of the first two eigenmodes of the cantilever, enables the simultaneous mapping of Young's modulus and the deformation and the topography of the sample [34]. As a result, these modes can be used for investigating complex cellular and biomolecular systems, in health and disease, and offering a detailed quantitative multiparametric characterization [35].

Viscoelastic mapping is another very novel mode that has its roots in research on multifrequency and bimodal AFM. This technique is a dynamic force-based mode that provides both imaging of the topography and maps of nanomechanical properties of soft-matter surfaces [36, 37]. Here, the cantilever is oscillated at two eigenmode frequencies—the first mode records the surface features and loss tangent data (amplitude modulation AM), while the second mode records frequency variations (frequency modulation FM) which relates to stiffness. AM-FM offers nanomechanical information of the specimen such as Young's modulus and contact stiffness [38] and has several advantages including fast scanning, high spatial resolution, and low forces applied to the sample. Although these modes are quite new, they have been used for investigating several biological samples, including proteins; small biological fibrils, like amyloid fibrils; lipid membranes; and viruses [39–42]. Also, it has been demonstrated that malign and benign cell lines present significant differences in their viscoelastic response [43].

3. Combined Imaging and Coupled AFM Systems and Their Applications

3.1. General. Although AFM presents high sensitivity and resolution on imaging and investigating biological samples at the nanoscale, it can lack other important information such as cellular components and biochemical functions [4, 44].

For example, optical microscopic imaging, especially using fluorescence, is another high-performance research tool that can provide complementary information. Fluorescence

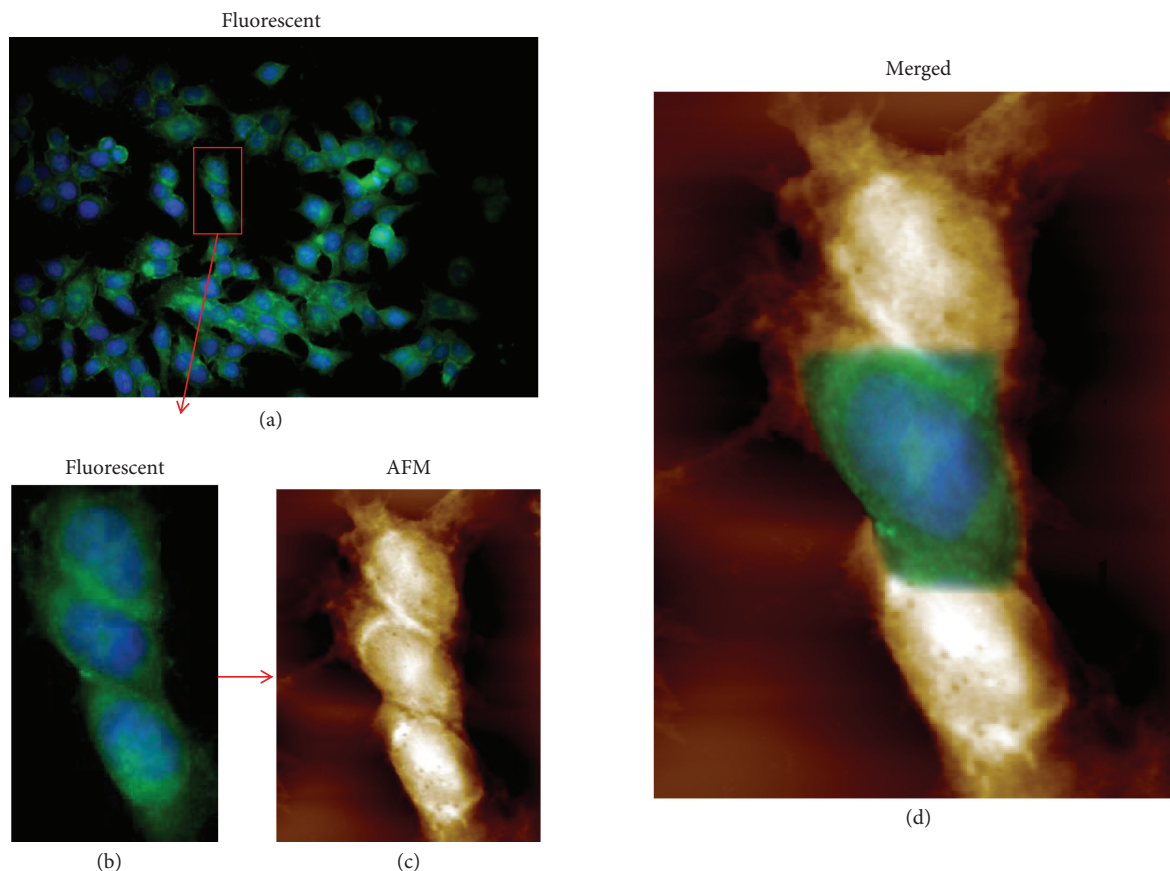


FIGURE 5: Combination of AFM with fluorescent microscopy: (a) MCF-7 breast cancer cells imaged with fluorescent microscopy (the blue color corresponds to DAPI staining that stains the cell nucleus and the green color represents antivasodilator-stimulated phosphoprotein (VASP) antibody. VASP is an actin-polymerization regulator which interacts with cell-ECM adhesion protein Migfilin and regulates cell migration [237]), (b) fluorescent image of three MCF-7 cells, (c) AFM image of the same cells, and (d) merged fluorescent and AFM images (unpublished data obtained by Andreas Stylianou in Cancer Biophysics Laboratory with an Olympus BX53 fluorescent microscope equipment, an Olympus XM10 monochrome CCD camera (1.4 megapixels), an UPlanFL N microscope objective lenses (40x/0.75 and 100x/1.30 oil), and a Molecular Imaging-Agilent PicoPlus AFM system (now known as 5500 AFM, Keysight Technologies)).

imaging can reveal the localization and quantify intracellular molecules and functions even at the level of a single molecule. Using specific fluorescence labelling, images of molecular mechanisms of biological functions can be acquired with high temporal resolution. Also, due to fluorescence intrinsic sensitivity to local microenvironment, valuable information on molecular specificities of cell structure can be obtained. However, as fluorescence imaging spatial resolution is limited by diffraction, its combination with AFM can produce images and provide us with information with high spatiotemporal resolution and biochemical specificity.

Generally, the combination of AFM with other microscopic imaging modalities can produce high-quality scientific information that cannot be achieved by using just one microscope.

3.2. AFM and Optical Microscopic Imaging. Optical microscopic techniques are often used in order to gain access to complementary information to AFM studies [45–47]. Using microscopies that utilize light in order to acquire images, such as simple optical, fluorescent, and laser scanning confocal microscope (CLSM), valuable information can be obtained

concerning cellular process and interactions. Fluorescence microscopy incorporates fluorescent probes that either are accumulated in cellular components or are highly sensitive to environmental changes such as alterations of calcium ions and hydrogen ions. Because of its intrinsic sensitivity, fluorescence microscopy can image even a single fluorescent molecule if the background is not fluorescent [48].

CLSM uses a pinhole approach to spatially limit out-of-focus light or glare from reaching the image detector. In that way, only the image of the focal plane is acquired providing better spatial resolution not only in x - y plane but also across the z -axis [49, 50]. Furthermore, by incorporating machine vision techniques and with the appropriate calibration, not only qualitative but also quantitative data are obtained [51].

In recent years, an increase in the number of studies that combine AFM with optical microscopic techniques has been published. The combination of the two modalities can provide unique information from a single cell (Figure 5) to a tissue level. Staunton et al. have developed a novel technique that combines AFM with a confocal microscope in order to explore the mechanical properties of soft heterogeneous three-dimensional samples [52]. They used metastatic breast

adenocarcinoma cells invading into collagen hydrogels, determining the elastic properties of both the cell and the extracellular matrix. Cells that are actively invading or fully embedded into the collagen matrix were found to be stiffer than cells lying on the matrix surface. This stiffening is Rho-associated protein kinase (ROCK) dependent, indicating that actomyosin contractility is a key player in the first phase of metastasis. On softer gels, enhanced invasion was observed either due to matrix softening by invading cells as a result of active rearrangement or proteolysis of adjacent fibers or because intrinsically softer tissues are preferable for invasion.

Stylianou et al. combined information from AFM with an optical and fluorescent microscope to study the tumor microenvironment such as fibroblasts (FBs) and cancer-associated fibroblasts (CAFs) [53]. In pancreatic tumors, treatment is reported to be blocked by desmoplasia, a cancer-specific type of fibrosis. Desmoplasia is a result of the interaction between stromal cells and tumor microenvironment. According to their results, CAFs express myofibroblast characteristics, such as α -smooth muscle actin expression, cell elongation, and lamellipodia formation, and are softer than FBs. Transforming growth factor beta (TGF- β) increases cell stiffness (Young's modulus) of both types of fibroblasts and elongation, cell spreading, lamellipodia formation, and spheroid invasion only in CAFs. In another study, Cazaux et al. have used AFM to mechanically stimulate, in a controlled manner over time and space, single immune cells and fluorescence imaging to follow the consequences of the contact through calcium fluorescent probes [54]. But they have also used light through a photoactivatable small G protein, Rac protein, to stimulate single T cell while recording cellular mechanical response. Canale et al. presented a review article trying to reveal the toxic interplay between lipid membranes and pathological protein aggregation in neurodegenerative disorders such as Alzheimer's and Parkinson's disease based on AFM studies [55]. In the study of Wegmann et al., neuroblastoma cells (N2a) and scrapie-infected mouse neuroblastoma (ScN2a) cells were studied with both AFM and immunofluorescence microscopy [56]. AFM imaging revealed a smooth surface topography of normal cells while scrapie-infected cells presented fibrillar aggregates on their surface. Immunofluorescence imaging, using a cellular prion protein (PrP) antibody (anti-PrP), revealed that PrP is homogeneously distributed in normal cells while it tended to segregate in preferential domains in ScN2a cells. Combining surface and fluorescence information, the authors concluded that the aggregated signal in SCNa2 cells is due to the structural changes at the cell surface. Finally, Kuyukina et al. using a hybrid imaging microscope, consisted of AFM and CLSM, studied bacterial viability at a single-cell level [57]. Fluorescent microscopy revealed that bacteria had compromised cell membranes when they were exposed to different organic solvent stresses. Combined information showed that changes in size, surface/volume ratio, and roughness were possible resistance mechanisms.

3.3. AFM and Second Harmonic Generation (SHG) Imaging. Except for fluorescence imaging, very promising microscopic modalities for biological imaging are based on nonlinear optics. These microscopic techniques can provide high-

resolution, three-dimensional images without the use of fluorescent labelling. In that way, structural and dynamic images of living cells are acquired in a noninvasive manner. Among them, second harmonic generation (SHG) has been used in combination with AFM for investigation of biological samples. SHG occurs when two photons of the frequency ω interact with a nonlinear medium and are converted into a new photon with twice the energy (2ω). As a nonlinear process, only noncentrosymmetric structures such as collagen are able to emit SHG signals [58]. Stylianou et al. proposed the combined AFM and SHG information as a valuable tool to understand the nonlinear optical properties of collagen and in the long-term SHG to be used as a nondestructive imaging modality to monitor collagen-related diseases [59]. They have developed thin collagen films with controlled characteristics that can help in modelling the collagen matrix in a variety of pathological conditions such as thermal injury or mimic the structure of the collagen matrix in different tissues and conditions. AFM was used for thin film characterization while the SHG signal was correlated and interpreted with the predetermined characteristics of the films. Navab et al. investigated integrin $\alpha11\beta1$, a stromal cell-specific receptor for fibrillar collagens that is overexpressed in CAFs, as a regulator of cancer stromal stiffness and promoter of tumorigenesis and metastasis in non-small-cell lung cancer [60]. Images acquired with SHG signals provided information on the quantification of collagen organization while AFM provided measurements of Young's modulus of the cancer-associated stroma. Their findings showed that the $\alpha11$ signaling pathway in CAFs is closely related with collagen cross-linking, with stiffness and with organization of fibrillar collagen matrices. In another study, Robinson et al. performed a quantitative analysis of 3D extracellular matrix (ECM) remodelling that is involved in a large number of physiopathological processes in biology [61]. Pancreatic stellate cell interactions with ECM were studied in a 3D environment via ECM remodelling. AFM studies provided collagen topography, mechanical properties, and stiffness, while SHG microscopy in combination with image analysis techniques was used to observe and acquire images of collagen structure and topology and to further quantify collagen fiber changes in terms of alignment and thickness. Their results demonstrated that the increased ECM stiffness observed in fibrosis can be correlated with ECM remodelling. Also, Chevalier et al. worked with enteric neural crest cells (ENCCs) *in vitro* and during colonization of the gastrointestinal tract in chicken and mouse embryos [62]. They used AFM to study the influence of the stiffness of the environment on ENCCs both *in vitro* and *in vivo* and SHG to study its structure. The AFM results revealed that although initially the mesenchyme of the gut was soft, its stiffness was gradually increased during ENCC colonization. Complementary to these findings, SHG showed a gradual organization and enrichment of collagen fibers in the developing gut that are associated with the abovementioned stiffness. Furthermore, Liu et al. suggested the use of a cell-based system to generate a mechanoresponsive cell system (MRCS) that responds specifically to mechanoenvironmental cues to sense and kill cancer metastasis [63]. SHG imaging reported high collagen

expression colocalized with cancer metastasis. Collagen networks were observed to be more linearized in cancer regions than in noncancer ones. AFM revealed an increased stiffness in cancer regions that are heterogeneous. Combination of AFM and SHG findings suggest a strong correlation between collagen cross-linking and increased tissue stiffness at the metastatic sites indicating the presence of a distinctive cancer mechanoenvironment.

3.4. AFM and Scanning Electron Microscopy (SEM) Imaging. AFM and SEM are two of the most commonly used nonoptical scanning microscopes that can provide us with surface imaging and characterization with high resolution. SEM has an excellent depth of field while AFM has poor depth of field, but excellent contrast on flat samples. SEM is able to measure the chemical composition of surface features, and AFM can measure its physical properties. If only image acquisition time is taken into account, SEM is faster than AFM but it produces 2D images while AFM can provide us directly with sample height information.

In most of the correlative microscopy research, more detailed information can be obtained by exploiting the advantages of both SEM and AFM [64–66]. For example, Mahmoud et al. performed a comparative study between AFM and SEM on healthy human liver parenchyma [65]. Hepatic architecture was mapped using both imaging modalities. AFM visualized the cellular structure, nucleus, and chromatin granules whereas SEM revealed other structures not observed by AFM. Pavlova et al. used both AFM and SEM to highlight their diagnostic and screening capabilities in kidney cancer based on pathomorphological changes in patient's erythrocytes [66]. Kaul-Ghanekar et al. on another combined study investigated the cellular morphology along with surface roughness [67]. They explored the effect of the tumor suppressor protein SMAR1 on cell lines and on tumor sections of mouse and human breast cancer of different grades. SMAR1 was found out to be a significant modulator of surface roughness and cytoskeletal volume. Finally, they suggested that SMAR1 might be used as a phenotypic differentiation marker between healthy and cancer cells. Also, Iyer et al. found, using combined AFM and SEM, different brush layers on the surface of normal and cancerous human cervical epithelial cells [68]. These brush layers are important for interacting with the environment and can be taken into account in characterization of cancer cells by means of forces and mechanical parameters. In another study, Volakis et al. used a mouse xenograft model to study the effect of myoferlin, a protein involved in membrane dynamics, on tumor formation and local invasion [69]. SEM along with image analysis quantified cell surface area, as well as the number and length of lamellipodia and filopodia. AFM was used to image and determine Young's modulus, a measure of cell stiffness that was found to be reduced in myoferlin-deficient cells and the integrity of the cytoskeletal network.

4. AFM and Collagen

4.1. General. As it was mentioned in the previous sections, AFM provides the ability to acquire topographic images at

the nanoscale combined to the mechanical property determination at specific regions. Hence, the topographical features of surfaces can be simultaneously acquired with its material stiffness. Novel AFM techniques, like bimodal AFM, have increased the nanoscale characterization capabilities of AFM to detect compositional variations in soft specimens, like proteins and cells [34]. Due to its high resolution, AFM has been widely used for the characterization of biomolecules such as fibrous and globular proteins. The main role of fibrous proteins is to provide mechanical stability [70]. Typical examples of fibrous proteins are the collagen and the amyloid fibrils, which are discussed in the next sections of this review.

AFM has been also extensively used for the mechanical characterization of globular proteins (i.e., proteins with a spherical shape and surface irregularities). Globular proteins present structural complexity [70], and its mechanical testing is a challenging procedure. Specifically, the classic models of applied mechanics, such as the Hertz model, provide several limitations in the analysis; thus, they can only be used approximately. Typical examples of globular proteins studied using AFM are the lysozyme, the bovine carbonic anhydrase II, and the lactate oxidase. In particular, Radmacher et al. investigated the viscoelastic properties of single lysozyme molecules (adsorbed on mica). For the theoretical analysis of the results, they used the Hertz model and Young's modulus of lysozyme was determined to be equal to 0.5 GPa [71]. In addition, for the investigation of the mechanical properties of bovine carbonic anhydrase II (BCA II), the modification of the Hertz model (which was proposed by Tataru [72]) was used. In the absence of Guanidine-HCl, Young's modulus of the native protein was determined to be equal to 75 MPa [73]. The mechanical properties of lactate oxidase (which has applications in bioanalytical devices for lactate determination) were determined by analyzing the fitted data obtained from the force curves (provided by AFM) to the Hertz model for conical and spherical indenter geometries. Young's modulus values in the case of lactate oxidase were calculated in the range 0.5–0.8 GPa [74].

4.2. Collagen. Collagens are the most abundant proteins in mammals and comprise almost the 30% of total cell protein in mammalian cells [75]. The collagen superfamily of vertebrate consists of more than 50 collagen and collagen-like proteins [76, 77]. The different members of the collagen superfamily have different shapes and sizes but the hallmark of a collagen is its monomer tropocollagen, which is composed of 3 polypeptide chains that form a right-handed triple-helical structure [76]. Each of these polypeptide chains contains a region with the repeating amino acid motif (Gly-X-Y), where X and Y can be any amino acid—12% of tripeptides have sequence Gly-Pro-Hyp; charged residues like arginine, lysine, and aspartic/glutamic acid make up approximately 15–20% of all residues in the monomer [78, 79].

The human body contains about 28 different collagens, among which fibrillar collagens and especially collagen type I are of most interest [76, 80]. Collagen type I is the major protein in the extracellular matrix [75], and it is characterized by unique properties such as self-assembly, biocompatibility,

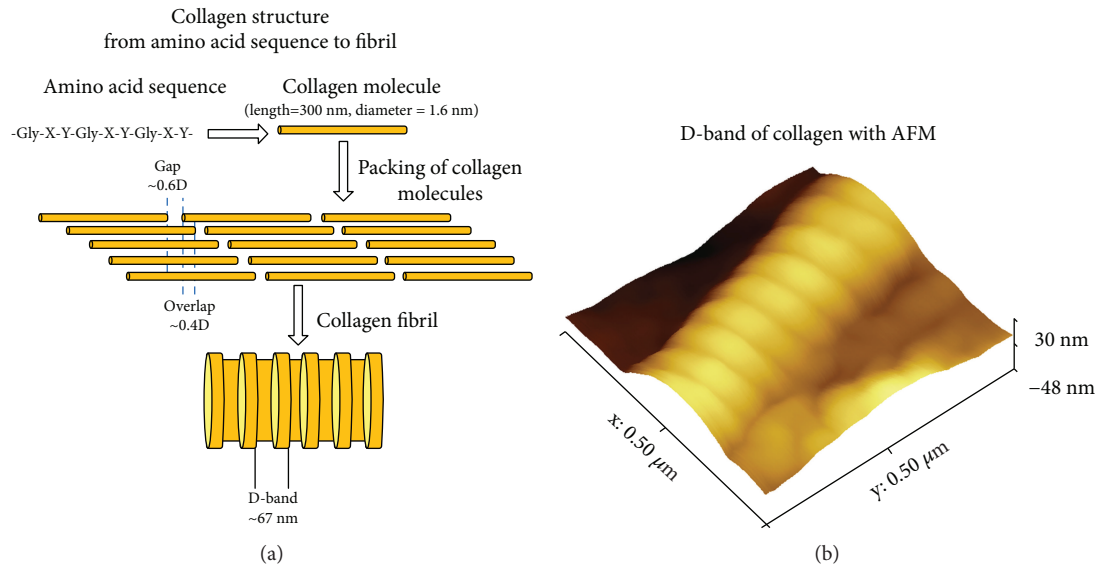


FIGURE 6: Collagen structure: (a) the collagen structure from the amino acid sequence to fibril. In this panel, the amino acid sequence, the collagen molecule, the packing of collagen molecules, and the structure of a collagen fibril are presented. (b) A collagen fiber D-band periodicity from a collagen thin film imaged using atomic force microscope (CPII Veeco-Bruker Microscope) in the tapping mode (adapted from [90]).

biodegradability, and nontoxicity [81]. Collagen type I molecules form rod-shaped triple helices assembled to form fibrils [77, 82], which are then properly aligned in order to form bundles and fibers [77, 82] (Figure 6(a)). Interestingly, the molecules are packed in a quarter-staggered fashion so as to form the D-band (also known as D-periodicity), which is a repeating banding pattern of about 67 nm (Figure 6(b)), depending on the tissue [75, 76, 83–86]. The fibrils of collagen type I are the elementary building blocks in many collagen-rich tissues [87, 88], while it presents different morphological functions (including tissue mechanical strength and scaffolding to cell migration) in different tissues [75, 77, 89]. Furthermore, collagen has been identified as a unique biomaterial for the formation of novel bioengineering interventions [75, 90–92]. AFM characterization (imaging and mechanical property measurements) has been extensively performed in pure collagen or collagen rich-tissues as AFM does not destroy the fibrillary structure of collagen and can offer information from collagen molecules to separated fibrils/fibers [81, 93]. AFM has been used for investigating a number of different issues concerning collagen, from collagen structure to collagen-related pathological conditions and collagen optical radiation or cell interactions.

The structural and the mechanical properties of collagen at the nanoscale under various conditions have been extensively studied using AFM [5, 22, 90, 94]. The major advantage of AFM in collagen investigation comparing to other techniques is its ability to provide information regarding nanotopographical features such as the D-band periodicity (the collagen fibril consists of an alternating gap and overlapping regions with a highly reproducible D-band periodicity of approximately 67 nm) [17]. Simultaneously, AFM can provide data regarding the mechanical response of selected regions at the nanoscale. Hence, AFM is a suitable tool for

the detection of local structural and mechanical variations of a single collagen fibril, under several external factors [11, 95]. The unique ability to combine information regarding nanotopographical and nanomechanical features using AFM in real time has led to groundbreaking solutions for the investigation of collagen [84, 96].

Thus, AFM has been used in several investigation areas related to tissues which contain collagen and has been proven a valuable tool in the field of histology and cytology [97]. Furthermore, AFM has been used for the investigation of collagen fibril structural variations at the nanoscale which are related to various pathological issues such as diabetes [98]. In addition, AFM has been increasingly used in the investigation regarding the influence of radiations arising either from nature or from medical activities (e.g., UV irradiation, radio-frequencies) on tissues which contain collagen [99, 100]. For example, the influence of UV irradiation on collagen at the nanoscale is a crucial issue regarding the general populations' health, due the chronic exposure of human skin in sunlight. As a result, the information provided at the nanoscale using AFM techniques has opened new insights into collagen research and the correlation of collagen nanofeature alterations with pathological situations.

4.2.1. Collagen-Ultraviolet (UV) Radiation Interactions. The clarification of the interactions of skin with sunlight is of crucial importance since it is an intrinsic constituent of human life [101]. Solar radiation is made up of infrared, visible, and ultraviolet (UV-C, UV-B, and UV-A) radiation and exposure of the human body (i.e., skin, eyes) to sun and especially to UV can be harmful and lead to sunburn, photoaging, corneal damage, and carcinogenesis [102, 103]. Additionally, UV irradiation is applied for material science purposes, including for sterilizing and cross-linking biomaterials [104–106]. As UV can induce a number of alterations

in collagen properties, including structure, chemical stability, and mechanical properties [107–111], AFM techniques have been extensively used for investigating UV-collagen interactions.

It has been shown that the irradiation of pure collagen with UV-C decreases the surface roughness [112–114], which is a crucial parameter in cell-surface crosstalk [115, 116] as modification in roughness alters the surface that is available for cell adhesion and growth [117]. The decrease of surface roughness due to UV irradiation has been demonstrated not only in pure collagen samples but also in collagen-based blends, including collagen-poly-vinyl alcohol, collagen-poly-vinyl pyrrolidone, and collagen-poly(ϵ -caprolactone) [112, 118, 119]. Although surface roughness was modified through UV-C irradiation, it has been shown that for the same dose, collagen fibrils retained their characteristic D-band structure [114]. The D-band periodicity is important for the fibril mechanical properties and the cell-collagen crosstalk, while it has been correlated with specific pathological conditions [84, 86, 120, 121]. Furthermore, AFM nanoindentation was used in order to investigate the effects of UV irradiation on the gap and overlapping zones of collagen D-band [17]. It was found that UV irradiation has a significant effect on the height level differences between the overlapping and gap zones, while the fibril stiffness (in terms of Young's modulus) in the D-band zone was reduced, which was associated with the UV-induced polypeptide chain scission. Moreover, it has been demonstrated that cells' behavior is affected when cells are cultured on UV-irradiated collagen-based substrates [114, 122, 123]. It has been shown that cells can normally spread on collagen-based substrates that were UV-irradiated with doses relevant to those that are used for sterilizing scope cells, but when the irradiation time was increased, the cells were characterized by abnormal growth (in terms of cell shape) [114]. In addition, it has been demonstrated that in some cases, UV irradiation of collagen supported cell growth and enhanced cell viability [111, 122, 123]. As AFM studies did not reveal significant modifications in topography when collagen is irradiated with low UV doses, the alterations in cell behavior have been suggested to be a consequence of either mechanical property alterations and/or chain scission [100, 124].

4.2.2. Low-Level Laser (LLL) Therapy Collagen Interactions.

Low-level laser therapy (LLLT), or photobiomodulation [125], applies low-level (also referred to as low-power) lasers for the treatment of several pathological conditions or abnormalities, including fibromyalgia, osteoarthritis, tuberculosis, temporomandibular joint disorders, and wound healing that presents increased interest. In the case of wound healing, it has been suggested that the underlying mechanism, which remains partially unknown, includes the increase of mitochondrial function, ATP, RNA, and protein synthesis [126]. Subsequently, these lead to increased oxygen consumption and enhanced synthesis of the reduced form of nicotinamide adenine dinucleotide (NADH) and ATP. As a result, a promotion of the cellular metabolism was observed along with enhanced wound healing mainly through the increase proliferation of fibroblasts and their ability to

produce collagen. Although the collagen role in the progress has been identified, the LLL-collagen interactions remain partially understood. Stylianou and Yova in 2015 used AFM techniques in order to investigate the effects that LLL (irradiation in the red region, 661 nm) has on collagen and the influence on cell culturing [127]. After LLLT irradiation, no statistical significant alterations were found in the nanoscale topographical characteristics of the collagen substrates (collagen thin films), but a negative effect (abnormal cell shape) was found on the fibroblasts that were cultured on the irradiated collagen substrates. As the modulation of fibroblast shape and behavior was recorded in the absence of measurable surface alterations, it was suggested that these effects are not influenced by the surface properties of the substrate through the surface contact guidance mechanism [128, 129]. These results offer new insights toward the clarification of the LLLT mechanism and the role of collagen in this procedure.

4.2.3. Nanomechanical Properties of Collagen. Extended studies focused on collagen using AFM techniques have been performed during the last decades due to the fact that many parts of the mammalian body contain collagen in the form of fibers (e.g., the skin, bones, cartilage, and tendons contain collagen fibers). Typical measurements of collagen fibers have been performed by Minary-Jolandan and Yu [11]. In their research, the mechanical differences on collagen fibrils due to the D-band periodicity were revealed (Young's modulus values were calculated to be ~ 1.2 GPa for the gap and ~ 2.2 GPa for the overlapping regions). The mechanical heterogeneity due to the D-periodicity was also confirmed by Kontomaris et al. [17]. Mechanical differences in the periodic banding of collagen from a rat tail tendon was also reported by Grant et al. [84]. However, Grant et al. took both a static and dynamic indentation approach to show that the topography had variances not only in elastic moduli but also in the time-dependent behavior at physiologically relevant frequencies (0.1–2 Hz). In addition, Strasser et al. determined Young's modulus of collagen fibril type I in the range 1.2 ± 1 GPa [130] and Yadavalli et al. in the range 1.03 ± 0.31 GPa [131]. In the same order of magnitude were the results presented in the research conducted by Heim et al. (i.e., Young's modulus values varied in the range 1–2 GPa) [132]. On the contrary, the results provided by Wenger et al. differ greatly comparing to the previous values (5–11.5 GPa) [133]. As mentioned, the key advantage of AFM is to carry out imaging and characterization under aqueous conditions, so it was shown that the nanomechanical properties of bovine Achilles tendon collagen fibrils changed by three orders of magnitude (1.9 ± 0.5 GPa to 1.2 ± 0.1 MPa) when going from ambient to buffer conditions [134]. Further, it was shown that reconstituted bovine Achilles tendon collagen can be mechanically tuned by altering the imaging buffer [78]. It was also shown that in imaging the same fibrils in air and under buffer, the diameter doubled in size. Then, the mechanical properties of collagen approximately doubled with addition of 1 M monovalent chloride salts, further increased by reducing the pH, and increased by a factor of 100 by testing under 100% ethanol [78]. Most

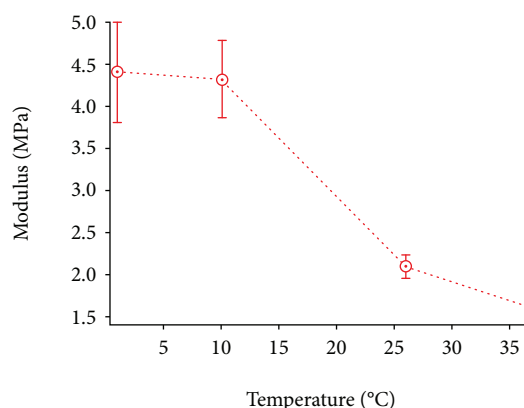


FIGURE 7: Moduli of a single individual collagen fibril at varying temperatures in PBS buffer (Colin Grant; unpublished data).

AFM studies test the compressive mechanical properties by nanoindentation; however, it is possible to carry out tensile testing on collagen fibrils [135]. Here, it was also shown that human collagen fibrils have reduced sensitivity to saline and pH compared to reconstituted collagen fibrils. As well as varying the aqueous conditions, the effect of temperature has also been carried out—nanomechanical properties of the same individual collagen fibril varied from 4.5 MPa at 1°C to 1.6 MPa at 37°C (Figure 7). This demonstrates the importance of carrying out nanomechanical property characterization of a biological matter under the most relevant physiological condition.

However, the determination of mechanical properties at the nanoscale is a challenging procedure. It is obvious from the results presented above that the extended range of values on Young's modulus values, even on the same sample, has been recorded (e.g., see the wide range of Young's modulus values regarding collagen in Table 1). The basic reasons for the wide range of Young's modulus values (even when the same sample is tested) are as follows:

- (a) The restrictions which are provided by the classic models of applied mechanics, commonly used for the analysis of the data obtained using AFM
- (b) The uncertainties in the experimental determination of critical magnitudes such as the spring's constant determination and the exact shape and dimensions of the AFM tip
- (c) Different used protocols for the sample preparation (e.g., testing in air or in liquid environment)

An analytical discussion of the approximations regarding the AFM indentation technique on biological samples is presented in "Approximations of the AFM Nanoindentation regarding Biological Samples and Biomaterials at the Nanoscale" in Supplementary Materials (available here).

4.2.4. Collagen in Tissue Samples. As previously discussed, collagen is the most abundant protein in the human body and is found in most tissues that requires some form of bio-mechanical structure/strength. AFM analysis can be carried

out to both image not only the collagenous structure of the tissue but also the nanomechanical properties. The sclera (white of the eye) has been investigated to show that the mechanical properties vary considerably on removing the episcleral layer to reveal the collagenous stromal layer [136]. The skin has the remarkable regenerative capacity to be able to heal itself in a complex cascade of biochemical and cellular remodeling processes. It was recently shown that the nanomechanical and viscoelastic properties of the upper dermis from the human skin change following wound healing [96]. Imaging revealed a variance in the orientation of collagen fibrils in scar tissue compared with healthy skin tissue, but also the scar tissue is stiffer than healthy tissue and also healthy tissue retains a higher dissipative characterization [96]. Similar dynamic/static nanoindentation was also carried out on porcine blood vessels [137]. The outer layer of the blood vessels (tunica adventitia) is a collagen layer that helps prevent overexpansion. Here, the adventitial layer of the porcine aorta vs. pulmonary arteries was compared, under aqueous conditions at 37°C. It was demonstrated that the aorta exhibited larger viscoelastic and dissipative characteristics, which makes sense as the aorta is under higher pressure compared with the pulmonary artery [137].

5. AFM and Specific Pathological Conditions

5.1. Articular Cartilage and Osteoarthritis

5.1.1. Cartilage. Articular cartilage is a connective tissue, which provides wear-resistant joint motion and low friction. It covers the ends of long bones and its thickness is in the range 1–3 mm. The main function of articular cartilage is to absorb and distribute the applied loads due to the joint movements. In addition, it provides protection to subchondral bone from damage. The functionality of articular cartilage is engendered by its collagen fiber meshwork and extracellular proteoglycan-rich matrix which is highly hydrated [138]. Loss of collagens or proteoglycans or structural changes may lead to a water content change and is a result to several damages to the tissue. As it has been previously reported, a loss of proteoglycans from the hydrated gel which is followed by an irreversible collagenolytic degradation of the fibrils results in damages regarding the collagen meshwork and as a result to the development of osteoarthritic cartilage [139].

Various methods are able to provide direct *in vitro* observation of cartilage under physiological conditions. Typical examples are the optical microscopy [140, 141], visual inspection, and histology [142, 143]. However, these methods are limited to a spatial resolution of approximately 200 nm. In addition, in the case of electron microscopy, ultra-structural details of articular cartilage at a molecular level can be provided, but the procedure requires dehydration and chemical fixation of the cartilage combined with metal staining or sputtering. Thus, the cartilage specimen cannot be examined at near physiological conditions. Moreover, optical and electron microscopy cannot provide measurements of the mechanical properties of articular cartilage.

The most direct method for stiffness measurements is the classic compression testing. However, the compression test

TABLE 1: Typical examples of Young's modulus values of collagen in the literature.

References	Collagen source	Young's modulus on collagen	
		Contact model used	Young's modulus values (GPa)
[17]	Type I collagen from bovine Achilles tendon	Oliver & Pharr model	0.74 - 1.43
[131]	Type I atelocollagen from calf skin	Hertz model	1.03 ± 0.31
[11]	Type I collagen from bovine Achilles tendon	Hertzian model, modified for cylindrical sample	1.2 - 2.2
[133]	Type I collagen fibrils from rat tail tendons	Oliver & Pharr model	3.75 - 11.5
[130]	Type I collagen fibrils from calf skin	Hertz model	1.2 ± 1

requires sample manipulation (e.g., the sample's surfaces have to be highly parallel and the cartilage has to be cut off the bone). On the other hand, macroindentation procedure does not require sample manipulation; hence, typical indentation testing devices can be used to evaluate the quality of the health or the disease state of articular cartilage [144–146]. These devices usually employ indenters with diameters in the range 1-2 mm in order to evaluate the correspondence of the sample to a specific applied load. However, stiffness measurements at the millimeter scale are not sensitive to detect pathological conditions (e.g., early-stage osteoarthritis) or changes due to aging [144, 146, 147].

5.1.2. Osteoarthritis. As it was already mentioned, various methods have been used for the determination of cartilage's pathological conditions; however, they are limited to specific conditions (e.g., measurements at the microscale or measurements at nonphysiological conditions) or they provide only specific information (e.g., imaging or mechanical properties). On the contrary, AFM provides the possibility of simultaneous imaging and mechanical property measurements (i.e., Young's modulus maps) on a micro- or nanometer scale in specimens that are near physiological conditions. Articular cartilage presents an interesting behavior depending on the level that is being tested. This interesting behavior has been revealed using AFM. In particular, at the micrometer scale, it behaves as a uniform and non-structured material. Hence, at the microscale, it presents an overall stiffness value which can be used as an initial approximation in order to evaluate its properties. In addition, it must be noted that cartilage can be modeled as a poroviscoelastic material; hence, the overall stiffness measurements provide an aggregate modulus, both viscous and elastic. As it has been previously reported, the aggregate modulus ranges between the values 1 MPa and 60 MPa depending on the loading conditions (~ 1 MPa for low-frequency conditions (< 0.1 Hz) and ~ 60 MPa for high-frequency loading (~ 40 Hz)).

Moreover, Young's modulus at specific regions of articular cartilage at the microscale or at the nanoscale can be calculated using AFM. As it has been previously reported, the elastic modulus of the articular cartilage intercellular matrix exhibits a depth-dependent increase. Specifically, Young's modulus value at the superficial zone is approximately 0.52 MPa and at the calcifying deep zone ~ 1.69 MPa [148, 149]. The major advantage of AFM comparing to traditional methods is that is able to provide information regarding the functionality of articular cartilage. Thus, using AFM, diseases such as osteoarthritis can be detected at the initial

stages. AFM has been used by many researchers as a tool for the diagnosis of cartilage's pathological conditions at early stages [14, 15, 150]. In particular, Stolz et al. [15] calculated Young's modulus of normal articular cartilage at the microscale (2.6 MPa) and nanoscale (0.021 MPa). The results of Loparic et al. are in the same order of magnitude. The microstiffness of articular cartilage was determined to be 1.3 ± 0.4 MPa and the nanostiffness 22.3 ± 1.5 kPa for cartilage's the proteoglycan gel (PG gel) and 184 ± 50 kPa for the collagen meshwork [150]. Stolz et al. investigated osteoarthritis at early stages and proved that microstiffness of articular cartilage does not present differences comparing to healthy cartilage. Hence, osteoarthritis at the early stages can be only detected at the nanoscale. In particular, at the nanoscale, nanostiffness was calculated to be 83 kPa in the case of normal cartilage and 5.6 kPa in the case of grade 3 osteoarthritis [14]. Hence, these findings proved the ability to detect early stages of osteoarthritis using AFM and have opened a new prospect for the use of AFM as a clinical tool. In particular, Stolz et al. tested AFM in real clinical activities; articular cartilage biopsies from seven patients who suffer from osteoarthritis (the age of the patients was in the range 62-96 years) were examined [14]. The result of this research has revealed an increasing softening of articular cartilage at the nanoscale with progressing osteoarthritis at a given age. It must be noted that all the detected changes at the initial stages of osteoarthritis could only be detected at the nanoscale.

In addition, Stolz et al. have shown that biomechanical and morphological changes occurring in articular cartilage during normal aging differ comparing to the ones occurring during osteoarthritis progression. The cartilage softening during osteoarthritis progression is due to the disintegration of collagen meshwork [14]. The stiffening of the collagen meshwork at the nanoscale can only be detected using AFM [14]. Hence, the ability to detect changes at early stages of osteoarthritis and distinguish these changes from the ones that occurred due to normal aging has opened an exciting prospect of using AFM as a tool in real clinical activities.

5.2. Cancer. Cancer progression has been associated with alterations in cancer cells and tumor microenvironment (TME) components [151, 152]. Alterations in cancer cells that make them differ from normal cells include changes in cell morphology, reproduction, communication, adhesion, cell-to-cell or cell-to-ECM interactions, cell invasion/metastasis, and even cell death. Recently, it has been demonstrated that cancer cells have different nanomechanical properties

than normal cells and alterations in the mechanical properties of cells play a crucial role during malignant transformation [152, 153]. TME consists of the tumor blood and lymphatic vessels, the stromal cells (FBs and CAFs), the ECM (including mainly collagen and hyaluronic acid), and a number of other soluble factors. Tumors have the tendency to modify their microenvironment in a way that promotes tumor growth and progression. For instance, in desmoplastic tumors, like pancreatic and breast cancers, the interactions between TME components lead to desmoplasia, which is characterized by the presence of CAFs and the overproduction of ECM components [154, 157]. This desmoplastic reaction leads to TME stiffening which increases the compressive mechanical forces in the tumor interior [113, 155, 156]. Furthermore, the crosstalk between TME and cancer cells influences a number of cancer cells' properties, including cell proliferation, migration, and cell invasion through surrounding tissues. Consequently, the understanding of cancer cells and TME alterations during cancer progressions is of utmost importance, in order to develop novel and more effective anticancer therapies or diagnostic techniques. There are several studies correlating the influence of the mechanical properties of the ECM and tumor progression [157, 158]. For instance, it has been demonstrated that caveolin-1 (Cav1, the major component of endocytic caveola plasma membrane, promotes among others the force-dependent contraction and TME stiffening [158]. AFM arises as a key tool in this research area, providing many novel research results [4, 159, 160]. AFM can be used as a unique technique in order to study cancer cell properties (such as growth, invasion, and metastasis), TME alterations, and cancer tissue progression. Generally, its ability to work on live cells with high resolution and to assess nanomechanical properties (e.g., Young's modulus properties) has made AFM a valuable technique in the field of cancer research. Apart from *in vitro* experiments of AFM on cancer cells, AFM has been used for studying the nanomechanical properties of TME components [4] and cancer tissue biopsies with great potentials [160–162]. In this section, we first present the use of AFM for characterizing the nanomechanical properties of cancer cells and its use for discrimination between healthy and cancer cells. Then, we discuss the use of AFM for investigating the nanomechanical properties from tissue biopsies and the possible application for early cancer diagnosis.

5.2.1. Cancer Cells

(1) *High-Resolution Imaging*. Although it has been demonstrated that cancer cells have different characteristics and properties than normal cells, they remain poorly identified or understood [163]. AFM techniques have already been used for studying cancer and normal cells in terms of morphology, cells' surface, pericellular activity, proteolytic activity, exosomes, cell-cell or cell-ECM interactions, and nanomechanical properties.

One of the key characteristics of AFM and one of its major advantages are its ability of high-resolution imaging. Although other techniques, like optical and fluorescence

microscopy, can offer significant information concerning cancer cell morphology at the single-cell level, AFM can provide information at the nanoscale concerning cell morphology and surface. For instance, AFM has been used for studying invadopodia which are cellular processes extended by the cells and play a significant role in cancer cell invasion and metastasis. Chasiotis et al. and Fillmore et al. used AFM to image the surface of human glioblastoma brain tumor cells (T98) on collagen substrates during invasion process [164, 165]. They demonstrated that invadopodia present an unusual nanomorphology and their results offered new insights concerning cell-substrate interactions. Additionally, AFM high-resolution imaging has been used for the characterization of single exosomes [166], which play a significant role in tumor proliferation and tumor microenvironment modulation [167–169]. Sharma et al. applied AFM techniques in order to investigate the exosomes from normal and cancer cells and showed that cancer cell-derived exosomes possess surface nanofilaments that may help in cell-cell communication [170]. Also, AFM can be applied to investigate specific cell activities that seem to be crucial for cell metastasis, as pericellular proteolytic activity which is important for TME remodeling and cancer cell invasion [171]. AFM can be used for assessing differences in average height, volume, and molecular weight distribution of pericellular matrix proteins in TME [171–173].

In the research area of cell-substrate interactions, AFM can provide unique information concerning the interactions of normal and cancer cells with culture substrates and obtain new data about cell-ECM interactions. It has been demonstrated that nonmetastatic breast cells adhered less to mineralized ECM secreted by osteoblasts than metastatic cells [174]. Furthermore, AFM has been used for investigating the mechanical response of cancer cells on different substrates. Park et al. studied prostate and breast cancer cells that were cultured on nanoscaffolds and showed that different cancer cell lines have distinct response to substrate characteristics such as size and nanomechanical properties [175]. Additionally, AFM can be used for studying cell-cell interaction. For instance, Puech et al. studied melanoma cell line during the binding process on human umbilical vein endothelial cells [176], while Laurent et al. investigated the adhesion strength between endothelial cells and cancer cells and demonstrated that the more invasive cells formed the strongest bonds with endothelial cells [177]. Hoffmann et al. used AFM in order to study the interaction forces among tumor cells and natural killer cells and demonstrated that in order to separate natural killer cells from cancer cells, the required forces are higher when the killer cell receptor 2B4 is activated [178].

(2) *Mechanical Properties of Cancer Cells*. Another area that presents a significant research interest is the use of AFM for assessing cancer cell nanomechanical properties. It can provide extremely high precision on the force applied to the cell, live and fixed ones, under natural conditions (e.g., in liquid conditions with temperature control), and it can provide quantitative mechanical measurements simultaneously to high-resolution imaging. As alteration in cytoarchitecture is

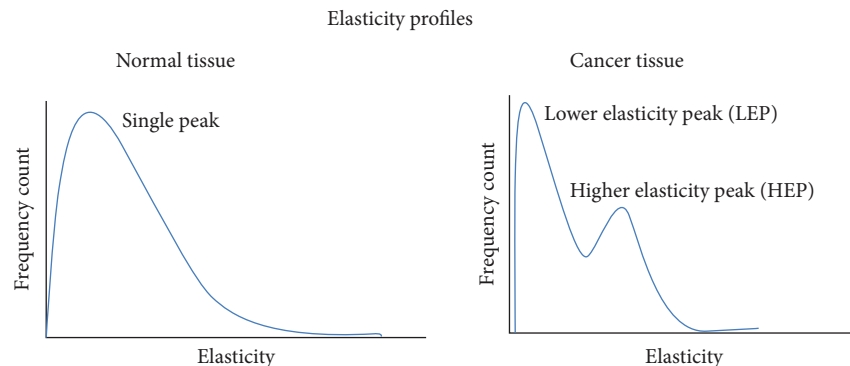


FIGURE 8: Schematic representations of predicted AFM elasticity measurements in normal and cancer tissues.

associated with cancer progression [164, 179, 180] and the cells' mechanical properties play a crucial role in cell motility, metastasis, and growth [181, 182], the investigation of the nanomechanical properties of cancer cells, in comparison with normal ones, is of particular scientific interest.

One of the first demonstrations of the AFM mechanical measurements on cancer cells was performed in 1993 by Weisenhorn et al. on lung cancer cells, but with a quite big variation in their Young modulus values. Afterwards, force-volume mode was used in order to provide enough statistics on embryonic cancer cells by Goldmann et al. [183, 184]. Although the study of single cancer cells can offer significant information concerning their mechanical properties, in 1999, the pioneer work of Lekka et al. demonstrated that the comparative investigation of cancer and normal cells can provide unique data [185, 186]. Bladder cells with different levels of malignancy were used, and the results demonstrated that cancer cells were softer than normal cells. This was the first study that demonstrated that AFM can be used for distinguishing cancer cells from normal cells in terms of cell deformability. In order to further correlate the cell malignancy with their deformability, a number of studies have been performed on different cell lines, including breast [161, 187], prostate [161, 188], and oral [189] tumor cells, showing that cancer cells are softer than normal cells in terms of Young's modulus values. Furthermore, Cross et al. investigated cells that were obtained from pleural effusion of patients and showed that metastatic cells are softer than benign cells in clinical samples [190], while in a number of studies, it has been demonstrated that cells derived from normal or nonmalignant tissues present a similar pattern [153]. All these studies suggest that the stiffness of tumor cells (in terms of Young's modulus) can be considered as a diagnostic method for distinguishing them from normal cells [161]. Additionally, recently, it was demonstrated that CAFs were also softer than normal FBs and present increased invasive properties [53]. Furthermore, it has been demonstrated that malign and benign cell lines present different viscoelastic properties [43]. More specifically, cancer cells are characterized a substantially larger loss tangent than benign cells [43]. On the other hand, it has been suggested that cell softening is a cell-type-specific response [191] and that this cell characteristic alone fails to serve as a universal indicator for

metastatic progression [192]. Consequently, more research is demanded toward this direction so as AFM to be used as a diagnostic tool for detecting cancer cells and distinguish them from normal ones in real clinical practice.

5.2.2. Cancer Tissue. Although in the previous section we present that cancer cells are softer than normal cells, it is a common belief that tumors are stiffer than their host tissue [162]. Tumor stiffening is caused by the increase in ECM composition, mainly collagen type I and collagen crosslinking during cancer progression [193–195], and it is the major biomechanical property of solid tumors that clinicians and patients can feel during palpation. Concerning the mechanical properties of tumor, AFM seems to be a valuable tool for assessing its nanomechanical properties with high spatial resolution. Although it has been presented that AFM has the potentials to be a unique cancer diagnostic tool [162, 180, 196], the work toward this direction is limited [160, 197–199].

One of the first studies on this area was performed on snap-frozen mammary tissues, and the results demonstrated that the malignant epithelium was stiffer than in isolated breast cancer cells and that the ECM adjacent to the epithelium progressively stiffens [198]. In 2012, Lekka et al. investigated tissue samples from patients with endometrioid carcinoma of the uterine, breast, and vulvar cancers and their results demonstrated that these tissues were softer than the nonneoplastic regions [161]. In a pioneer work, in the same year, Plodinec et al. demonstrated that AFM can be used for assessing unique nanomechanical fingerprints from human breast biopsies that can be used for cancer breast diagnosis [162]. Their results revealed that normal and benign tissues present a uniform stiffness (in terms of Young's modulus) distribution, while malignant tissue was characterized by two distinguishable maxima. The same maxima were reported by Tian et al. in 2015 in human liver tissue and were referred as lower elasticity peak (LEP) and higher elasticity peak (HEP) (Figure 8) [199]. Also, in this study, the different stiffness distributions and maxima of other tissues (including esophageal cancer, clear cell renal cell carcinoma, colon cancer, and papillary renal cell carcinoma) were reported.

In 2016, Ciasca et al. demonstrated that AFM can assess nanomechanical fingerprints of human glioblastoma and

meningothelial meningioma and AFM techniques can be applied for tumor brain grading [200]. In the same year, Ansardamavandi et al. developed clustering algorithms in order to divide and categorize the derived stiffness (in terms of Young's modulus values) measurements [197]. With their technique, they achieve to divide the measurements into three categories (the cellular, the noncellular, and the fibrous part of the tissue) and demonstrated that AFM can be combined with computational methods for identifying more than two different components of the tissue. In 2017, Cui et al. used AFM for investigating the nanomechanical fingerprints of cervical cancer and cervical intraepithelial neoplasia [201]. The research results demonstrated that both healthy and cancer samples present bimodal distribution of Young's modulus values with similar values of LEP, but cancer HEP values demonstrated that cancer tissues were significantly stiffer than the healthy controls. Consequently, HEP values could be used as a nanomechanical biomarker for cancer diagnosis. Also, in 2017, Minelli et al. applied an operator-independent neural network in order to identify the nanomechanical fingerprints of brain cancer [202]. Their technique achieves to identify and distinguish cancer from healthy tissue in a fully automated fashion.

The results so far have demonstrated that AFM is arising a novel technique for assessing the nanomechanical properties of cancer tissue and has the potential to provide a novel tool for early cancer diagnosis.

5.3. Alzheimer's Disease

5.3.1. Amyloid Fibrils. The study of protein fibrils is an important subject in various research fields and disciplines. A very interesting fibrous protein complex is amyloid fibrils which are highly ordered fibrillar structures assembled from either peptides or unfolded proteins [203]. The deposition of amyloid, in the form of amyloid plaques, has been associated with a number of degenerative diseases, while the amyloid structure has also been found in many functional proteins that are not related with a specific disease. As the involved mechanisms remain unknown, the clarification of the mechanisms of fibrillation, the structural features of the amyloid fibrils, and their physical and nanomechanical properties will help to reveal their biological role [203]. AFM and its capabilities for nanomechanical characterization of biological samples arise as a very significant tool for the study of the amyloid fibrils. For instance, Roeters et al. used AFM in combination with other techniques (such as X-ray powder diffraction and IR spectroscopy) for studying the aggregation of the intrinsically disordered protein alpha-synuclein (α S) into amyloid fibrils [204]. These amyloid fibrils have been correlated with the pathology of Parkinson's disease. Their results demonstrated that the structure of α S fibrils varies as a function of ionic strength, and they argued that this sensitivity to the ionic strength might form the basis of differences in α S-related pathologies. Also, in the last years, many researchers have focused on the self-assembly of amyloid peptides and proteins at interfaces since it will provide significant information for understanding the mechanism of some neurodegenerative diseases

[205]. The AFM has been employed in this area and so far, the results demonstrate that interfaces play an important role in peptide assembly [205]. Furthermore, very recently, Watanabe-Nakayama and Ono used high-speed AFM (HS-AFM), which allows the video imaging of the conformational changes of individual molecules, in order to investigate the structural dynamics of individual amyloidogenic protein assemblies [206].

5.3.2. Alzheimer's Disease. As it was already mentioned, the formation of fibrous particles is associated with a number of specific diseases. One of these, which have a great social impact, is Alzheimer's disease (AD). Patients with this disease presents neuritic plaques and vascular deposits consisting from fibrous aggregates of the protein amyloid- β ($A\beta$). More specifically, the hydrophilic molecules of $A\beta$ accumulated outside of the neural cells and result in the formation of these highly toxicity amyloid plaques [207]. These amyloid plaques are composed of amyloid fibrils and small oligomers, which are insoluble protein aggregates [208]. Although the aggregation of the $A\beta$ protein has been correlated with neurotoxicity, the involved mechanisms remain unclear [7]. Soon after the development of the AFM, it was demonstrated that the AFM is a powerful tool for studying the $A\beta$ amyloids and the AFM can provide unique information for understanding the structural origins of this complex neurodegenerative disease [7]. For instance, in 1996, AFM was used to investigate the self-assembly and the surface structure of the resultant fibrils [209, 210]. AFM has been applied in many studies since then for studying $A\beta$ amyloids with several research purposes. Some of the more recent research results use advanced, sophisticated, and coupled AFM techniques. Furthermore, AFM has been used for studying β -amyloid structure in liquid conditions [211] and β -amyloid aggregation as a function of concentration [212]. Also, Connelly et al. investigated the ion channel mechanism and pore structures of the amyloids of AD pathology by using AFM [213], while several studies study the relationship between the formation of β -amyloid fibrils and toxicity in AD [214]. Furthermore, Song et al. used AFM in combination with fluorescence spectroscopy so as to study the interactions between vanillin and $A\beta$ polypeptide [215]. Their results demonstrated the depolymerization of $A\beta$ 1-42 aggregates by vanillin in a dose-dependent manner, and the authors suggested that vanillin may be a potential pharmacological agent for the treatment of AD. In another study, Han et al. developed a sophisticated AFM-based technique to evaluate the amyloid precursor protein (APP) cleavage mechanism at the nanomolecular level, as the clarification of the APP cleavage mechanism is crucial for the development of new AD therapeutic agents [216]. Also, Banerjee et al. studied isolated cross-linked $A\beta$ 42 trimers ($A\beta$ oligomers) with HS-AFM which enabled the visualization of the structural dynamics of the oligomers at nanometer resolution on a millisecond time scale. According to the researchers, the nanoscale characterization of the $A\beta$ oligomer structure and dynamics can lead to the development of novel oligomer-specific therapeutic agents. In other recent works, Li et al. used real-time AFM combined with molecular dynamics

simulations as a novel approach to investigate the amyloid nanostructures formed by a potential pentapeptide inhibitor [217], while Han et al. applied AFM in order to probe the interactions between A β and two kinds of antibodies [207].

5.4. Viruses and HIV

5.4.1. Viruses. AFM has opened a new prospect regarding the investigation of the physical properties of viruses [218, 219]. The research regarding the structural properties of viruses and virus mechanics facilitates the engineering of their physical properties in order to improve their applications in bionanotechnology and molecular biology [220]. In particular, AFM provides the ability to acquire topographic images of biological objects at the nanometer scale (such as the viruses). The first imaging attempt regarding viruses, using scanning probe microscopy (STM), was provided by Baró et al. [221]. The virus particle that was visualized was the bacteriophage Φ 29. But as in STM imaging the sample has to be electrical conductive, the particle was covered with a metallic layer that is far from its physiological conditions. This limitation has been overcome using AFM, which does not require electrical conductivity. AFM has been widely used for the topographic property determination of viruses, partially disassembled viruses, viral capsids, nucleic acids, etc. [222–225]. In addition, AFM can be used in order to investigate the viral infection in live cell process [226–229] and for the determination of the interaction forces between viruses and other molecules [220].

Viruses are solid-state objects; thus, the determination of their mechanical properties is possible. For almost all “empty” capsids, Young’s modulus has been determined under the assumption that the capsid is homogeneous and hollow with idealized geometry [220]. In addition, the shell thickness and the empty capsid’s size are considered to be similar to the real capsid’s size [218, 220]. For Young’s modulus determination, the thin elasticity theory and finite element analysis on the model particle are usually used. However, the validity of this approach for Young’s modulus determination is under discussion [230]. A different approach for the determination of the mechanical properties of viruses is based on the consideration of the virus particle and the AFM cantilever as two ideal springs in series. In this case, the “spring constant” of the particle k_p can be determined using the following equation: $k_{ef}^{-1} = k_p^{-1} + k_c^{-1}$ where, k_{ef} is the value of the effective spring’s constant (which is calculated from the slope of the force vs. distance curves) and k_c is the cantilever’s spring constant. However, despite the fact that stiffness, as it is calculated using the spring constant, is an object’s property, it does not depend only on the material but also depends on the object’s dimensions and geometry.

Moreover, an alternative method for the mechanical property determination of viruses is the structural strength determination. In the most of the cases, the linearity of the force vs. distance curves is lost when a specific force is applied. The loss of the linearity is due to the mechanical failure or buckling in the particle. In addition, it must be noted that for the mechanical property determination of particles, a number of load-indentation curves are used. The force

experiments usually do not cause permanent damages to the particles. However, a big number of indentation experiments may result in a nonlinear mechanical response or in mechanical failure. This behavior is caused by the material fatigue of the particle.

5.4.2. HIV. A typical example of a virus in medicine, with great significance and social impact that can be tested using the AFM methods, is the human immunodeficiency virus (HIV). HIV is an enveloped retrovirus with a genetic material that in the first phases of development is in a single-stranded RNA form [231]. In the mature phase of development, the viral genomic RNA is encapsidated within a cone-shaped capsid [231]. HIV capsid is a conical shell with a length \sim 100–120 nm which is formed during viral maturation by the assembly of about 1500 capsid protein molecules (these molecules are organized into 250 hexamers and 12 pentamers approximately). The presence of these pentamers induces the curvature necessary to form the cone shape of the capsid [232–234].

The calculation of the stiffness of the capsid is mandatory for the assessment of any mechanical model regarding the capsid’s uncoating. Several experiments for the determination of the mechanical properties of HIV 1 particles using AFM have been performed during the last decade [220, 231, 235, 236]. In particular, Ramalho et al. applied the nanoindentation technique to measure the stiffness of empty capsids independently from the viral envelope. In particular, in vitro assemblies of wild-type and mutant recombinant HIV-1 capsid protein and isolated and mutant HIV-1 cores (i.e., filled capsids) were tested. This research resulted that the mutant assemblies were significantly stiffer than the wild-type assemblies. Pang et al. investigated the mechanism under which the physical properties of viral particles change during maturation and the effects of these changes in the viral lifestyle [235]. Their results indicated that HIV presents a severe reduction in particle stiffness during maturation that is mediated by the viral envelope protein. Kol et al. compared the mechanical properties of mature and immature HIV viruses using AFM nanoindentation [236]. The spring constant of the mature HIV-1 virus was calculated equal to 0.22 N/m while the spring constant of immature HIV-1 virus was calculated equal to 3.15 N/m. In addition, Young’s moduli were found to be 0.44 GPa and 0.93 GPa for the mature and the immature HIV-1, respectively, which means that the immature HIV-1 virus is stiffer than the mature one. The research regarding HIV is of great importance due to the fact that the mechanical softening as a result of maturation of HIV-1 (which is due to the loss of Env-Gag interactions) is probably a necessary condition before the infection occurrence [220].

6. Conclusions

AFM is a unique tool for nanocharacterization, including high-resolution imaging and nanomechanical measurements, of biological samples under different environmental conditions. New advances of AFM enable the simultaneous imaging with other modalities offering new perspectives in

the field. A plethora of studies so far have demonstrated the abilities of AFM for assessing unique nanocharacteristics of biological samples that can be correlated with different pathological conditions. Consequently, AFM stands out as the ideal research instrument for exploring the detection of pathological conditions even at very early stages, making it very attractive in the area of bio- and nanomedicine.

Abbreviations

3D:	Three dimensional
AD:	Alzheimer's disease
AFM:	Atomic force microscopy
APP:	Amyloid precursor protein
ATP:	Adenosine triphosphate
CAFs:	Cancer-associated fibroblasts
CLSM:	Laser scanning confocal microscope
ECM:	Extracellular matrix
ENCCs:	Enteric neural crest cells
FBs:	Fibroblasts
HIV:	Human immunodeficiency virus
HS-AFM:	High-speed AFM
ILK:	Integrin-linked kinase
KFM:	Kelvin force microscopy
LLLT:	Low-level laser therapy
MRCS:	Mechanoresponsive cell system
NADH:	Reduced form of nicotinamide adenine dinucleotide
PrP:	Prion protein
SEM:	Scanning electron microscopy
SHG:	Second harmonic generation
SPM:	Scanning probe microscopy
STM:	Scanning tunnelling microscopy
TEM:	Transmission electron microscopy
TME:	Tumor microenvironment
UV:	Ultraviolet
VASP:	Vasodilator-stimulated phosphoprotein.

Conflicts of Interest

The authors declare that there is no conflict of interest regarding the publication of this paper.

Supplementary Materials

Approximations of the AFM nanoindentation regarding biological samples and biomaterials at the nanoscale. (*Supplementary Materials*)

References

- [1] A. Stylianou, D. Yova, and K. Politopoulos, "Atomic force microscopy quantitative and qualitative nanoscale characterization of collagen thin films," in *Proceedings of the 5th Conference on Emerging Technologies in NDT*, CRC Press 2012, Chapter 65, pp. 415–420, 2012.
- [2] D. P. Allison, N. P. Mortensen, C. J. Sullivan, and M. J. Doktycz, "Atomic force microscopy of biological samples," *Wiley Interdisciplinary Reviews: Nanomedicine and Nanobiotechnology*, vol. 2, no. 6, pp. 618–634, 2010.
- [3] N. Gadegaard, "Atomic force microscopy in biology: technology and techniques," *Biotechnic & Histochemistry*, vol. 81, no. 2-3, pp. 87–97, 2006.
- [4] A. Stylianou and T. Stylianopoulos, "Atomic force microscopy probing of cancer cells and tumor microenvironment components," *BioNanoScience*, vol. 6, no. 1, pp. 33–46, 2016.
- [5] A. Stylianou, D. Yova, and E. Alexandratou, "Nanotopography of collagen thin films in correlation with fibroblast response," *Journal of Nanophotonics*, vol. 7, no. 1, article 073590, 2013.
- [6] G. Binnig, C. F. Quate, and C. Gerber, "Atomic force microscope," *Physical Review Letters*, vol. 56, no. 9, pp. 930–933, 1986.
- [7] V. J. Morris, A. R. Kirby, and A. P. Gunning, *Atomic Force Microscopy for Biologists*, Imperial College Press, London, 2008.
- [8] A. Stylianou, D. Yova, E. Alexandratou, and A. Petri, "Atomic force imaging microscopy investigation of the interaction of ultraviolet radiation with collagen thin films," in *Nanoscale Imaging, Sensing, and Actuation for Biomedical Applications X*, San Francisco, CA, USA, February 2013.
- [9] A. Bergmann, D. Feigl, D. Kuhn et al., "A low-cost AFM setup with an interferometer for undergraduates and secondary-school students," *European Journal of Physics*, vol. 34, no. 4, pp. 901–914, 2013.
- [10] Y. Seo and W. Jhe, "Atomic force microscopy and spectroscopy," *Reports on Progress in Physics*, vol. 71, no. 1, article 016101, 2007.
- [11] M. Minary-Jolandan and M. F. Yu, "Nanomechanical heterogeneity in the gap and overlap regions of type I collagen fibrils with implications for bone heterogeneity," *Biomacromolecules*, vol. 10, no. 9, pp. 2565–2570, 2009.
- [12] F. M. Ohnesorge, "Towards atomic resolution non-contact dynamic force microscopy in a liquid," *Surface and Interface Analysis*, vol. 27, no. 5-6, pp. 379–385, 1999.
- [13] W. C. Oliver and G. M. Pharr, "Measurement of hardness and elastic modulus by instrumented indentation: advances in understanding and refinements to methodology," *Journal of Materials Research*, vol. 19, no. 1, pp. 3–20, 2004.
- [14] M. Stolz, R. Gottardi, R. Raiteri et al., "Early detection of aging cartilage and osteoarthritis in mice and patient samples using atomic force microscopy," *Nature Nanotechnology*, vol. 4, no. 3, pp. 186–192, 2009.
- [15] M. Stolz, R. Raiteri, A. U. Daniels, M. R. Van Landingham, W. Baschong, and U. Aebi, "Dynamic elastic modulus of porcine articular cartilage determined at two different levels of tissue organization by indentation-type atomic force microscopy," *Biophysical Journal*, vol. 86, no. 5, pp. 3269–3283, 2004.
- [16] C. Braunsmann, J. Seifert, J. Rheinlaender, and T. E. Schäffer, "High-speed force mapping on living cells with a small cantilever atomic force microscope," *Review of Scientific Instruments*, vol. 85, no. 7, article 073703, 2014.
- [17] S. V. Kontomaris, A. Stylianou, D. Yova, and G. Balogiannis, "The effects of UV irradiation on collagen D-band revealed by atomic force microscopy," *Scanning*, vol. 37, no. 2, 111 pages, 2015.
- [18] S. V. Kontomaris, A. Stylianou, D. Yova, and K. Politopoulos, "Mechanical properties of collagen fibrils on thin films by atomic force microscopy nanoindentation," in *2012 IEEE*

- 12th International Conference on Bioinformatics & Bioengineering (BIBE)*, pp. 608–613, Larnaca, Cyprus, November 2012.
- [19] S. V. Kontomaris, D. Yova, A. Stylianou, and K. Politopoulos, “The significance of the percentage differences of Young’s modulus in the AFM nanoindentation procedure,” *Micro and Nanosystems*, vol. 7, no. 2, pp. 86–97, 2015.
- [20] A. Stylianou, S. V. Kontomaris, and D. Yova, “Assessing collagen nanoscale thin films heterogeneity by AFM multi-mode imaging and nanoindentation for nanobiomedical applications,” *Micro and Nanosystems*, vol. 6, no. 2, pp. 95–102, 2014.
- [21] D. Kirmizis and S. Logothetidis, “Atomic force microscopy probing in the measurement of cell mechanics,” *International Journal of Nanomedicine*, vol. 5, no. 1, pp. 137–145, 2010.
- [22] A. Stylianou and D. Yova, “Surface nanoscale imaging of collagen thin films by atomic force microscopy,” *Materials Science and Engineering C*, vol. 33, no. 5, pp. 2947–2957, 2013.
- [23] D. P. John and H. Georg, “Calibration of the torsional and lateral spring constants of cantilever sensors,” *Nanotechnology*, vol. 25, no. 22, article 225701, 2014.
- [24] S. Habelitz, M. Balooch, S. J. Marshall, G. Balooch, and G. W. Marshall Jr, “In situ atomic force microscopy of partially demineralized human dentin collagen fibrils,” *Journal of Structural Biology*, vol. 138, no. 3, pp. 227–236, 2002.
- [25] W. Melitz, J. Shen, A. C. Kummel, and S. Lee, “Kelvin probe force microscopy and its application,” *Surface Science Reports*, vol. 66, no. 1, pp. 1–27, 2011.
- [26] T. Yamaoka, H. Tsujikawa, S. Hasumura et al., “Vacuum magnetic force microscopy at high temperatures: observation of permanent magnets,” *Microscopy Today*, vol. 22, no. 6, pp. 12–17, 2014.
- [27] E. I. Altman, M. Z. Baykara, and U. D. Schwarz, “Noncontact atomic force microscopy: an emerging tool for fundamental catalysis research,” *Accounts of Chemical Research*, vol. 48, no. 9, pp. 2640–2648, 2015.
- [28] P. D. Garcia and R. Garcia, “Determination of the elastic moduli of a single cell cultured on a rigid support by force microscopy,” *Biophysical Journal*, vol. 114, no. 12, pp. 2923–2932, 2018.
- [29] S. E. Campbell, V. L. Ferguson, and D. C. Hurley, “Nanomechanical mapping of the osteochondral interface with contact resonance force microscopy and nanoindentation,” *Acta Biomaterialia*, vol. 8, no. 12, pp. 4389–4396, 2012.
- [30] M. O. Krisenko, A. Cartagena, A. Raman, and R. L. Geahlen, “Nanomechanical property maps of breast cancer cells as determined by multiharmonic atomic force microscopy reveal SYK-dependent changes in microtubule stability mediated by map1b,” *Biochemistry*, vol. 54, no. 1, pp. 60–68, 2015.
- [31] D. M. Harcombe, M. G. Ruppert, M. R. P. Ragazzon, and A. J. Fleming, “Higher-harmonic AFM imaging with a high-bandwidth multifrequency Lyapunov filter,” *2017 IEEE International Conference on Advanced Intelligent Mechatronics (AIM)*, 2017, pp. 725–730, Munich, Germany, July 2017.
- [32] N. Shamsudhin, H. Rothuizen, B. J. Nelson, and A. Sebastian, “Multi-frequency atomic force microscopy: a system-theoretic approach,” *IFAC Proceedings Volumes*, vol. 47, no. 3, pp. 7499–7504, 2014.
- [33] A. Raman, S. Trigueros, A. Cartagena et al., “Mapping nanomechanical properties of live cells using multi-harmonic atomic force microscopy,” *Nature Nanotechnology*, vol. 6, no. 12, pp. 809–814, 2011.
- [34] S. Benaglia, V. G. Gisbert, A. P. Perrino, C. A. Amo, and R. Garcia, “Fast and high-resolution mapping of elastic properties of biomolecules and polymers with bimodal AFM,” *Nature Protocols*, vol. 13, no. 12, pp. 2890–2907, 2018.
- [35] Y. F. Dufréne, D. Martínez-Martín, I. Medalsy, D. Alsteens, and D. J. Müller, “Multiparametric imaging of biological systems by force-distance curve-based AFM,” *Nature Methods*, vol. 10, no. 9, pp. 847–854, 2013.
- [36] R. García and R. Pérez, “Dynamic atomic force microscopy methods,” *Surface Science Reports*, vol. 47, no. 6-8, pp. 197–301, 2002.
- [37] R. Garcia and R. Proksch, “Nanomechanical mapping of soft matter by bimodal force microscopy,” *European Polymer Journal*, vol. 49, no. 8, pp. 1897–1906, 2013.
- [38] G. Chawla and S. D. Solares, “Mapping of conservative and dissipative interactions in bimodal atomic force microscopy using open-loop and phase-locked-loop control of the higher eigenmode,” *Applied Physics Letters*, vol. 99, no. 7, article 074103, 2011.
- [39] Z. Al-Rekabi and S. Contera, “Multifrequency AFM reveals lipid membrane mechanical properties and the effect of cholesterol in modulating viscoelasticity,” *Proceedings of the National Academy of Sciences of the United States of America*, vol. 115, no. 11, pp. 2658–2663, 2018.
- [40] I. González-Domínguez, S. Gutiérrez-Granados, L. Cervera, F. Gòdia, and N. Domingo, “Identification of HIV-1-based virus-like particles by multifrequency atomic force microscopy,” *Biophysical Journal*, vol. 111, no. 6, pp. 1173–1179, 2016.
- [41] G. Lamour, C. K. Yip, H. Li, and J. Gsponer, “High intrinsic mechanical flexibility of mouse prion nanofibrils revealed by measurements of axial and radial Young’s moduli,” *ACS Nano*, vol. 8, no. 4, pp. 3851–3861, 2014.
- [42] Z. Y. Zheng, R. Xu, S. L. Ye et al., “High harmonic exploring on different materials in dynamic atomic force microscopy,” *Science China Technological Sciences*, vol. 61, no. 3, pp. 446–452, 2018.
- [43] J. Rother, H. Nöding, I. Mey, and A. Janshoff, “Atomic force microscopy-based microrheology reveals significant differences in the viscoelastic response between malignant and benign cell lines,” *Open Biology*, vol. 4, no. 5, 2014.
- [44] U. Maver, T. Velnar, M. Gaberšček, O. Planinšek, and M. Finšgar, “Recent progressive use of atomic force microscopy in biomedical applications,” *TrAC Trends in Analytical Chemistry*, vol. 80, pp. 96–111, 2016.
- [45] M. Cascione, V. de Matteis, R. Rinaldi, and S. Leporatti, “Atomic force microscopy combined with optical microscopy for cells investigation,” *Microscopy Research and Technique*, vol. 80, no. 1, pp. 109–123, 2017.
- [46] S. Handschuh-Wang, T. Wang, and X. Zhou, “Recent advances in hybrid measurement methods based on atomic force microscopy and surface sensitive measurement techniques,” *RSC Advances*, vol. 7, no. 75, pp. 47464–47499, 2017.
- [47] L. Zhou, M. Cai, T. Tong, and H. Wang, “Progress in the correlative atomic force microscopy and optical microscopy,” *Sensors*, vol. 17, no. 4, p. 938, 2017.
- [48] J. W. Lichtman and J.-A. Conchello, “Fluorescence microscopy,” *Nature Methods*, vol. 2, no. 12, pp. 910–919, 2005.

- [49] J.-A. Conchello and J. W. Lichtman, "Optical sectioning microscopy," *Nature Methods*, vol. 2, no. 12, pp. 920–931, 2005.
- [50] J. Jonkman and C. M. Brown, "Any way you slice it—a comparison of confocal microscopy techniques," *Journal of Biomolecular Techniques*, vol. 26, no. 2, pp. 54–65, 2015.
- [51] E. Alexandratou, D. Yova, and S. Loukas, "A confocal microscopy study of the very early cellular response to oxidative stress induced by zinc phthalocyanine sensitization," *Free Radical Biology and Medicine*, vol. 39, no. 9, pp. 1119–1127, 2005.
- [52] J. R. Staunton, B. L. Doss, S. Lindsay, and R. Ros, "Correlating confocal microscopy and atomic force indentation reveals metastatic cancer cells stiffen during invasion into collagen I matrices," *Scientific Reports*, vol. 6, no. 1, article 19686, 2016.
- [53] A. Stylianou, V. Gkretsi, and T. Stylianopoulos, "Transforming growth factor- β modulates pancreatic cancer associated fibroblasts cell shape, stiffness and invasion," *Biochimica et Biophysica Acta (BBA) - General Subjects*, vol. 1862, no. 7, pp. 1537–1546, 2018.
- [54] S. Cazaux, A. Sadoun, M. Biarnes-Pelicot et al., "Synchronizing atomic force microscopy force mode and fluorescence microscopy in real time for immune cell stimulation and activation studies," *Ultramicroscopy*, vol. 160, pp. 168–181, 2016.
- [55] C. Canale, R. Oropesa-Nuñez, A. Diaspro, and S. Dante, "Amyloid and membrane complexity: the toxic interplay revealed by AFM," *Seminars in Cell & Developmental Biology*, vol. 73, pp. 82–94, 2018.
- [56] S. Wegmann, M. Miesbauer, K. F. Winklhofer, J. Tatzelt, and D. J. Muller, "Observing fibrillar assemblies on scrapie-infected cells," *Pflügers Archiv - European Journal of Physiology*, vol. 456, no. 1, pp. 83–93, 2008.
- [57] M. S. Kuyukina, I. B. Ivshina, I. O. Korshunova, and E. V. Rubtsova, "Assessment of bacterial resistance to organic solvents using a combined confocal laser scanning and atomic force microscopy (CLSM/AFM)," *Journal of Microbiological Methods*, vol. 107, pp. 23–29, 2014.
- [58] A. M. Streets, A. Li, T. Chen, and Y. Huang, "Imaging without fluorescence: nonlinear optical microscopy for quantitative cellular imaging," *Analytical Chemistry*, vol. 86, no. 17, pp. 8506–8513, 2014.
- [59] A. Stylianou, K. Politopoulos, M. Kyriazi, and D. Yova, "Combined information from AFM imaging and SHG signal analysis of collagen thin films," *Biomedical Signal Processing and Control*, vol. 6, no. 3, pp. 307–313, 2011.
- [60] R. Navab, D. Strumpf, To C et al., "Integrin $\alpha 11\beta 1$ regulates cancer stromal stiffness and promotes tumorigenicity and metastasis in non-small cell lung cancer," *Oncogene*, vol. 35, no. 15, pp. 1899–1908, 2015.
- [61] B. K. Robinson, E. Cortes, A. J. Rice, M. Sarper, and A. del Río Hernández, "Quantitative analysis of 3D extracellular matrix remodelling by pancreatic stellate cells," *Biology Open*, vol. 5, no. 6, pp. 875–882, 2016.
- [62] N. R. Chevalier, E. Gazquez, L. Bidault et al., "Corrigendum: how tissue mechanical properties affect enteric neural crest cell migration," *Scientific Reports*, vol. 6, no. 1, article 34118, 2016.
- [63] L. Liu, S. X. Zhang, W. Liao et al., "Mechanoresponsive stem cells to target cancer metastases through biophysical cues," *Science Translational Medicine*, vol. 9, no. 400, 2017.
- [64] F. Braet, D. J. Taatjes, and E. Wisse, "Probing the unseen structure and function of liver cells through atomic force microscopy," *Seminars in Cell & Developmental Biology*, vol. 73, pp. 13–30, 2018.
- [65] M. Mahmoud, K. T. Daniela, M. Sascha, B. Mark, and H. Sonja, "3-D morphological characterization of the liver parenchyma by atomic force microscopy and by scanning electron microscopy," *Microscopy Research and Technique*, vol. 64, no. 1, pp. 1–9, 2004.
- [66] T. V. Pavlova, I. A. Pavlo, N. B. Pilkevich, and M. A. Chaplygina, "Methods of scanning blood microscopy in oncology diagnosis of kidney pathology," *Journal of Pharmacy Research*, vol. 11, no. 12, pp. 1589–1593, 2017.
- [67] R. Kaul-Ghanekar, S. Singh, H. Mamgain, A. Jalota-Badhwar, K. M. Paknikar, and S. Chattopadhyay, "Tumor suppressor protein SMAR1 modulates the roughness of cell surface: combined AFM and SEM study," *BMC Cancer*, vol. 9, no. 1, p. 350, 2009.
- [68] S. Iyer, R. M. Gaikwad, V. Subba-Rao, C. D. Woodworth, and I. Sokolov, "Atomic force microscopy detects differences in the surface brush of normal and cancerous cells," *Nature Nanotechnology*, vol. 4, no. 6, pp. 389–393, 2009.
- [69] L. I. Volakis, R. Li, A. WEt et al., "Loss of myoferlin redirects breast cancer cell motility towards collective migration," *PLoS One*, vol. 9, no. 2, article e86110, 2014.
- [70] B. Alberts, A. Johnson, J. Lewis, P. Walter, M. Raff, and K. Roberts, *Molecular Biology of the Cell*, International Student Edition: Routledge, 4th edition, 2002.
- [71] M. Radmacher, M. Fritz, J. P. Cleveland, D. A. Walters, and P. K. Hansma, "Imaging adhesion forces and elasticity of lysozyme adsorbed on mica with the atomic force microscope," *Langmuir*, vol. 10, no. 10, pp. 3809–3814, 1994.
- [72] Y. Tatara, "Extensive theory of force- approach relations of elastic spheres in compression and in impact," *Journal of Engineering Materials and Technology*, vol. 111, no. 2, pp. 163–168, 1989.
- [73] R. Afrin, M. T. Alam, and A. Ikai, "Pretransition and progressive softening of bovine carbonic anhydrase II as probed by single molecule atomic force microscopy," *Protein Science*, vol. 14, no. 6, pp. 1447–1457, 2005.
- [74] A. Parra, E. Casero, E. Lorenzo, F. Pariente, and L. Vázquez, "Nanomechanical properties of globular proteins: lactate oxidase," *Langmuir*, vol. 23, no. 5, pp. 2747–2754, 2007.
- [75] P. Fratzl, *Collagen Structure and Mechanics*, Springer, New York, NY, USA, 2008.
- [76] D. J. S. Hulmes, "Collagen diversity, synthesis and assembly," in *Collagen*, pp. 15–47, Springer, Boston, MA, USA, 2008.
- [77] S. Ricard-Blum, "The collagen family," *Cold Spring Harbor Perspectives in Biology*, vol. 3, no. 1, pp. 1–19, 2011.
- [78] C. A. Grant, D. J. Brockwell, S. E. Radford, and N. H. Thomson, "Tuning the elastic modulus of hydrated collagen fibrils," *Biophysical Journal*, vol. 97, no. 11, pp. 2985–2992, 2009.
- [79] M. G. Venugopal, J. A. M. Ramshaw, E. Braswell, D. Zhu, and B. Brodsky, "Electrostatic interactions in collagen-like triple-helical peptides," *Biochemistry*, vol. 33, no. 25, pp. 7948–7956, 1994.
- [80] K. E. Kadler, C. Baldock, J. Bella, and R. P. Boot-Handford, "Collagens at a glance," *Journal of Cell Science*, vol. 120, no. 12, pp. 1955–1958, 2007.
- [81] V. Hasirci, E. Vrana, P. Zorlutuna et al., "Nanobiomaterials: a review of the existing science and technology, and

- new approaches," *Journal of Biomaterials Science, Polymer Edition*, vol. 17, no. 11, pp. 1241–1268, 2006.
- [82] S. Ricard-Blum, F. Ruggiero, and M. Van Der Rest, "The collagen superfamily," in *Collagen*, J. Brinckmann, H. Notbohm, and P. K. Müller, Eds., vol. 247 of Topics in Current Chemistry, pp. 35–84, Springer, Berlin, Heidelberg, 2005.
- [83] L. Bozec, G. van der Heijden, and M. Horton, "Collagen fibrils: nanoscale ropes," *Biophysical Journal*, vol. 92, no. 1, pp. 70–75, 2007.
- [84] C. A. Grant, M. A. Phillips, and N. H. Thomson, "Dynamic mechanical analysis of collagen fibrils at the nanoscale," *Journal of the Mechanical Behavior of Biomedical Materials*, vol. 5, no. 1, pp. 165–170, 2012.
- [85] J. A. Petruska and A. J. Hodge, "A subunit model for the tropocollagen macromolecule," *Proceedings of the National Academy of Sciences of the United States of America*, vol. 51, no. 5, pp. 871–876, 1964.
- [86] J. M. Wallace, B. G. Orr, J. C. Marini, and M. M. B. Holl, "Nanoscale morphology of type I collagen is altered in the Brl mouse model of osteogenesis imperfecta," *Journal of Structural Biology*, vol. 173, no. 1, pp. 146–152, 2011.
- [87] V. P. Ivanova and A. I. Krivchenko, "A current viewpoint on structure and evolution of collagens. I. Fibrillar collagens," *Journal of Evolutionary Biochemistry and Physiology*, vol. 48, no. 2, pp. 127–139, 2012.
- [88] M. D. Shoulders and R. T. Raines, "Collagen structure and stability," *Annual Review of Biochemistry*, vol. 78, no. 1, pp. 929–958, 2009.
- [89] M. K. Gordon and R. A. Hahn, "Collagens," *Cell and Tissue Research*, vol. 339, no. 1, pp. 247–257, 2010.
- [90] A. Stylianou, "Atomic force microscopy for collagen-based nanobiomaterials," *Journal of Nanomaterials*, vol. 2017, Article ID 9234627, 14 pages, 2017.
- [91] G. T. Tihan, I. Rău, R. G. Zgârian, and M. V. Ghica, "Collagen-based biomaterials for ibuprofen delivery," *Comptes Rendus Chimie*, vol. 19, no. 3, pp. 390–394, 2016.
- [92] B. D. Walters and J. P. Stegemann, "Strategies for directing the structure and function of three-dimensional collagen biomaterials across length scales," *Acta Biomaterialia*, vol. 10, no. 4, pp. 1488–1501, 2014.
- [93] D. A. Cisneros, J. Friedrichs, A. Taubenberger, C. M. Franz, and D. J. Muller, "Creating ultrathin nanoscopic collagen matrices for biological and biotechnological applications," *Small*, vol. 3, no. 6, pp. 956–963, 2007.
- [94] A. Stylianou, V. Gkretsi, and T. Stylianopoulos, "Atomic force microscopy nano-characterization of 3D collagen gels with tunable stiffness," *MethodsX*, vol. 5, pp. 503–513, 2018.
- [95] N. E. Kurland, Z. Drira, and V. K. Yadavalli, "Measurement of nanomechanical properties of biomolecules using atomic force microscopy," *Micron*, vol. 43, no. 2-3, pp. 116–128, 2012.
- [96] C. A. Grant, P. C. Twigg, and D. J. Tobin, "Static and dynamic nanomechanical properties of human skin tissue using atomic force microscopy: effect of scarring in the upper dermis," *Acta Biomaterialia*, vol. 8, no. 11, pp. 4123–4129, 2012.
- [97] T. Ushiki, J. Hitomi, S. Ogura, T. Umemoto, and M. Shigeno, "Atomic force microscopy in histology and cytology," *Archives of Histology and Cytology*, vol. 59, no. 5, pp. 421–431, 1996.
- [98] B. E. Layton, A. M. Sastry, H. Wang et al., "Differences between collagen morphologies, properties and distribution in diabetic and normal biobreeding and Sprague-Dawley rat sciatic nerves," *Journal of Biomechanics*, vol. 37, no. 6, pp. 879–888, 2004.
- [99] S. Choi, Y. Cheong, J. H. Shin et al., "Short-term nanostructural effects of high radiofrequency treatment on the skin tissues of rabbits," *Lasers in Medical Science*, vol. 27, no. 5, pp. 923–933, 2012.
- [100] A. Sionkowska and T. Wess, "Mechanical properties of UV irradiated rat tail tendon (RTT) collagen," *International Journal of Biological Macromolecules*, vol. 34, no. 1-2, pp. 9–12, 2004.
- [101] V. T. Natarajan, P. Ganju, A. Ramkumar, R. Grover, and R. S. Gokhale, "Multifaceted pathways protect human skin from UV radiation," *Nature Chemical Biology*, vol. 10, no. 7, pp. 542–551, 2014.
- [102] E. D. Baron and A. K. Suggs, "Introduction to photobiology," *Dermatologic Clinics*, vol. 32, no. 3, pp. 255–266, 2014.
- [103] D. Markovitsi, E. Sage, L. D. Frederick, and J. Davies, "Interaction of UV radiation with DNA," *Photochemical & Photobiological Sciences*, vol. 12, no. 8, pp. 1256–1258, 2013.
- [104] G. Fessel, J. Wernli, Y. Li, C. Gerber, and J. G. Snedeker, "Exogenous collagen cross-linking recovers tendon functional integrity in an experimental model of partial tear," *Journal of Orthopaedic Research*, vol. 30, no. 6, pp. 973–981, 2012.
- [105] A. Gaspar, L. Moldovan, D. Constantin, A. M. Stanciu, P. M. Sarbu Boeti, and I. C. Efrimescu, "Collagen-based scaffolds for skin tissue engineering," *Journal of Medicine and Life*, vol. 4, no. 2, pp. 172–177, 2011.
- [106] H. Suh and J. C. Park, "Evaluation of calcification in porcine valves treated by ultraviolet ray and glutaraldehyde," *Materials Science and Engineering C*, vol. 13, no. 1-2, pp. 65–73, 2000.
- [107] N. N. Fathima, R. Suresh, J. R. Rao, and B. U. Nair, "Effect of UV irradiation on the physicochemical properties of collagen stabilized using aldehydes," *Journal of Applied Polymer Science*, vol. 104, no. 6, pp. 3642–3648, 2007.
- [108] N. N. Fathima, R. Suresh, J. R. Rao, B. U. Nair, and T. Ramasami, "Effect of UV irradiation on stabilized collagen: role of chromium (III)," *Colloids and Surfaces B: Biointerfaces*, vol. 62, no. 1, pp. 11–16, 2008.
- [109] K. Jariashvili, B. Madhan, B. Brodsky, A. Kuchava, L. Namicheishvili, and N. Metreveli, "UV damage of collagen: insights from model collagen peptides," *Biopolymers*, vol. 97, no. 3, pp. 189–198, 2012.
- [110] N. O. Metreveli, K. K. Jariashvili, L. O. Namicheishvili et al., "UV-vis and FT-IR spectra of ultraviolet irradiated collagen in the presence of antioxidant ascorbic acid," *Ecotoxicology and Environmental Safety*, vol. 73, no. 3, pp. 448–455, 2010.
- [111] J. Skopinska-Wisniewska, A. Sionkowska, A. Kaminska, A. Kaznica, R. Jachimaki, and T. Drewa, "Surface characterization of collagen/elastin based biomaterials for tissue regeneration," *Applied Surface Science*, vol. 255, no. 19, pp. 8286–8292, 2009.
- [112] A. Sionkowska, A. Planecka, J. Kozłowska, and J. Skopińska-Wisniewska, "Surface properties of UV-irradiated poly (vinyl alcohol) films containing small amount of collagen," *Applied Surface Science*, vol. 255, no. 7, pp. 4135–4139, 2009.
- [113] T. Stylianopoulos, J. D. Martin, V. P. Chauhan et al., "Causes, consequences, and remedies for growth-induced solid stress

- in murine and human tumors,” *Proceedings of the National Academy of Sciences of the United States of America*, vol. 109, no. 38, pp. 15101–15108, 2012.
- [114] A. Stylianou, D. Yova, and E. Alexandratou, “Investigation of the influence of UV irradiation on collagen thin films by AFM imaging,” *Materials Science and Engineering: C*, vol. 45, pp. 455–468, 2014.
- [115] K. Anselme, A. Ponche, and M. Bigerelle, “Relative influence of surface topography and surface chemistry on cell response to bone implant materials. Part 2: biological aspects,” *Proceedings of the Institution of Mechanical Engineers, Part H: Journal of Engineering in Medicine*, vol. 224, no. 12, pp. 1487–1507, 2010.
- [116] C. Zink, H. Hall, D. M. Brunette, and N. D. Spencer, “Orthogonal nanometer-micrometer roughness gradients probe morphological influences on cell behavior,” *Biomaterials*, vol. 33, no. 32, pp. 8055–8061, 2012.
- [117] U. Covani, L. Giacomelli, A. Krajewski et al., “Biomaterials for orthopedics: a roughness analysis by atomic force microscopy,” *Journal of Biomedical Materials Research-Part A*, vol. 82A, no. 3, pp. 723–730, 2007.
- [118] Z. Cheng and S. H. Teoh, “Surface modification of ultra thin poly (ϵ -caprolactone) films using acrylic acid and collagen,” *Biomaterials*, vol. 25, no. 11, pp. 1991–2001, 2004.
- [119] A. Sionkowska, J. Kozłowska, A. Planecka, and J. Skopińska-Wiśniewska, “Collagen fibrils in UV irradiated poly(vinyl pyrrolidone) films,” *Applied Surface Science*, vol. 255, no. 5, pp. 2030–2039, 2008.
- [120] K. Poole, K. Khairy, J. Friedrichs et al., “Molecular-scale topographic cues induce the orientation and directional movement of fibroblasts on two-dimensional collagen surfaces,” *Journal of Molecular Biology*, vol. 349, no. 2, pp. 380–386, 2005.
- [121] D. R. Stamov, A. Müller, Y. Wegrowski, S. Brezillon, and C. M. Franz, “Quantitative analysis of type I collagen fibril regulation by lumican and decorin using AFM,” *Journal of Structural Biology*, vol. 183, no. 3, pp. 394–403, 2013.
- [122] M. Achilli, J. Lagueux, and D. Mantovani, “On the effects of UV-C and pH on the mechanical behavior, molecular conformation and cell viability of collagen-based scaffold for vascular tissue engineering,” *Macromolecular Bioscience*, vol. 10, no. 3, pp. 307–316, 2010.
- [123] A. B. Caruso and M. G. Dunn, “Changes in mechanical properties and cellularity during long-term culture of collagen fiber ACL reconstruction scaffolds,” *Journal of Biomedical Materials Research-Part A*, vol. 73A, no. 4, pp. 388–397, 2005.
- [124] S. Anastase-Ravion, M. P. Carreno, C. Blondin et al., “Synergistic effects of glucose and ultraviolet irradiation on the physical properties of collagen,” *Journal of Biomedical Materials Research*, vol. 60, no. 3, pp. 384–391, 2002.
- [125] D. P. Kuffler, “Photobiomodulation in promoting wound healing: a review,” *Regenerative Medicine*, vol. 11, no. 1, pp. 107–122, 2016.
- [126] K. Chawla, A. K. Lamba, S. Tandon, F. Faraz, and V. Gaba, “Effect of low-level laser therapy on wound healing after depigmentation procedure: a clinical study,” *Journal of Indian Society of Periodontology*, vol. 20, no. 2, pp. 184–188, 2016.
- [127] A. Stylianou and D. Yova, “Atomic force microscopy investigation of the interaction of low-level laser irradiation of collagen thin films in correlation with fibroblast response,” *Lasers in Medical Science*, vol. 30, no. 9, pp. 2369–2379, 2015.
- [128] M. K. Driscoll, X. Sun, C. Guven, J. T. Fourkas, and W. Losert, “Cellular contact guidance through dynamic sensing of nanotopography,” *ACS Nano*, vol. 8, no. 4, pp. 3546–3555, 2014.
- [129] F. Zhou, L. Yuan, H. Huang, and H. Chen, “Phenomenon of “contact guidance” on the surface with nano-micro-groove-like pattern and cell physiological effects,” *Chinese Science Bulletin*, vol. 54, no. 18, pp. 3200–3205, 2009.
- [130] S. Strasser, A. Zink, M. Janko, W. M. Heckl, and S. Thalhammer, “Structural investigations on native collagen type I fibrils using AFM,” *Biochemical and Biophysical Research Communications*, vol. 354, no. 1, pp. 27–32, 2007.
- [131] V. K. Yadavalli, D. V. Svintradze, and R. M. Pidaparti, “Nano-scale measurements of the assembly of collagen to fibrils,” *International Journal of Biological Macromolecules*, vol. 46, no. 4, pp. 458–464, 2010.
- [132] A. J. Heim, W. G. Matthews, and T. J. Koob, “Determination of the elastic modulus of native collagen fibrils via radial indentation,” *Applied Physics Letters*, vol. 89, no. 18, article 181902, 2006.
- [133] M. P. E. Wenger, L. Bozec, M. A. Horton, and P. Mesquidaz, “Mechanical properties of collagen fibrils,” *Biophysical Journal*, vol. 93, no. 4, pp. 1255–1263, 2007.
- [134] C. A. Grant, D. J. Brockwell, S. E. Radford, and N. H. Thomson, “Effects of hydration on the mechanical response of individual collagen fibrils,” *Applied Physics Letters*, vol. 92, no. 23, article 233902, 2008.
- [135] R. B. Svensson, T. Hassenkam, C. A. Grant, and S. P. Magnusson, “Tensile properties of human collagen fibrils and fascicles are insensitive to environmental salts,” *Biophysical Journal*, vol. 99, no. 12, pp. 4020–4027, 2010.
- [136] C. A. Grant, N. H. Thomson, M. D. Savage, H. W. Woon, and D. Greig, “Surface characterisation and biomechanical analysis of the sclera by atomic force microscopy,” *Journal of the Mechanical Behavior of Biomedical Materials*, vol. 4, no. 4, pp. 535–540, 2011.
- [137] C. A. Grant and P. C. Twigg, “Pseudostatic and dynamic nanomechanics of the tunica adventitia in elastic arteries using atomic force microscopy,” *ACS Nano*, vol. 7, no. 1, pp. 456–464, 2013.
- [138] P. G. Alexander, R. Gottardi, H. Lin, T. P. Lozito, and R. S. Tuan, “Three-dimensional osteogenic and chondrogenic systems to model osteochondral physiology and degenerative joint diseases,” *Experimental Biology and Medicine (Maywood, N.J.)*, vol. 239, no. 9, pp. 1080–1095, 2014.
- [139] R. Gottardi, U. Hansen, R. Raiteri et al., “Supramolecular organization of collagen fibrils in healthy and osteoarthritic human knee and hip joint cartilage,” *PLoS One*, vol. 11, no. 10, article e0163552, 2016.
- [140] M. D. Buschmann, E. B. Hunziker, Y. J. Kim, and A. J. Grodzinsky, “Altered aggrecan synthesis correlates with cell and nucleus structure in statically compressed cartilage,” *Journal of Cell Science*, vol. 109, pp. 499–508, 1996.
- [141] F. Guilak, A. Ratcliffe, and V. C. Mow, “Chondrocyte deformation and local tissue strain in articular cartilage: a confocal microscopy study,” *Journal of Orthopaedic Research*, vol. 13, no. 3, pp. 410–421, 1995.
- [142] D. L. Garner and D. C. McGillivray, “Living articular cartilage is not smooth. The structure of mammalian and avian joint surfaces demonstrated in vivo by immersion incident light

- microscopy," *Annals of the Rheumatic Diseases*, vol. 30, no. 1, pp. 3–9, 1971.
- [143] D. P. Speer and L. Dahners, "The collagenous architecture of articular cartilage. Correlation of scanning electron microscopy and polarized light microscopy observations," *Clinical Orthopaedics and Related Research*, no. 139, pp. 267–275, 1979.
- [144] R. C. Appleyard, M. V. Swain, S. Khanna, and G. A. Murrell, "The accuracy and reliability of a novel handheld dynamic indentation probe for analysing articular cartilage," *Physics in Medicine & Biology*, vol. 46, no. 2, pp. 541–550, 2001.
- [145] R. M. Aspden, T. Larsson, R. Svensson, and D. Heinegård, "Computer-controlled mechanical testing machine for small samples of biological viscoelastic materials," *Journal of Biomedical Engineering*, vol. 13, no. 6, pp. 521–525, 1991.
- [146] G. N. Duda, R. U. Kleemann, U. Bluecher, and A. Weiler, "A new device to detect early cartilage degeneration," *The American Journal of Sports Medicine*, vol. 32, no. 3, pp. 693–698, 2004.
- [147] K. A. Athanasiou, C. F. Zhu, X. Wang, and C. M. Agrawal, "Effects of aging and dietary restriction on the structural integrity of rat articular cartilage," *Annals of Biomedical Engineering*, vol. 28, no. 2, pp. 143–149, 2000.
- [148] R. V. Patel and J. J. Mao, "Microstructural and elastic properties of the extracellular matrices of the superficial zone of neonatal articular cartilage by atomic force microscopy," *Frontiers in Bioscience*, vol. 8, no. 1, pp. a18–a25, 2003.
- [149] S. Tomkoria, R. V. Patel, and J. J. Mao, "Heterogeneous nanomechanical properties of superficial and zonal regions of articular cartilage of the rabbit proximal radius condyle by atomic force microscopy," *Medical Engineering & Physics*, vol. 26, no. 10, pp. 815–822, 2004.
- [150] M. Loparic, D. Wirz, A. U. Daniels et al., "Micro- and nanomechanical analysis of articular cartilage by indentation-type atomic force microscopy: validation with a gel-microfiber composite," *Biophysical Journal*, vol. 98, no. 11, pp. 2731–2740, 2010.
- [151] F. Chen, X. Zhuang, L. Lin et al., "New horizons in tumor microenvironment biology: challenges and opportunities," *BMC Medicine*, vol. 13, no. 1, 2015.
- [152] S. Kumar and V. M. Weaver, "Mechanics, malignancy, and metastasis: the force journey of a tumor cell," *Cancer and Metastasis Reviews*, vol. 28, no. 1–2, pp. 113–127, 2009.
- [153] M. Lekka, "Discrimination between normal and cancerous cells using AFM," *BioNano Science*, vol. 6, no. 1, pp. 65–80, 2016.
- [154] D. Hanahan and R. A. Weinberg, "Hallmarks of cancer: the next generation," *Cell*, vol. 144, no. 5, pp. 646–674, 2011.
- [155] T. R. Cox, D. Bird, A. M. Baker et al., "LOX-mediated collagen crosslinking is responsible for fibrosis-enhanced metastasis," *Cancer Research*, vol. 73, no. 6, pp. 1721–1732, 2013.
- [156] T. Stylianopoulos and R. K. Jain, "Combining two strategies to improve perfusion and drug delivery in solid tumors," *Proceedings of the National Academy of Sciences of the United States of America*, vol. 110, no. 46, pp. 18632–18637, 2013.
- [157] V. Gkretsi, A. Stylianou, P. Papageorgis, C. Polydorou, and T. Stylianopoulos, "Remodeling components of the tumor microenvironment to enhance cancer therapy," *Frontiers in Oncology*, vol. 5, p. 214, 2015.
- [158] J. G. Goetz, S. Minguet, I. Navarro-Lérida et al., "Biomechanical remodeling of the microenvironment by stromal caveolin-1 favors tumor invasion and metastasis," *Cell*, vol. 146, no. 1, pp. 148–163, 2011.
- [159] A. Stylianou, V. Gkretsi, C. Patrickios, and T. Stylianopoulos, "Exploring the nano-surface of collagenous and other fibrotic tissues with AFM," in *Fibrosis*, L. Rittié, Ed., vol. 1627 of *Methods in Molecular Biology*, pp. 453–489, Humana Press, New York, NY, USA, 2017.
- [160] A. Stylianou, M. Lekka, and T. Stylianopoulos, "AFM assessing of nanomechanical fingerprints for cancer early diagnosis and classification: from single cell to tissue level," *Nanoscale*, vol. 10, no. 45, pp. 20930–20945, 2018.
- [161] M. Lekka, D. Gil, K. Pogoda et al., "Cancer cell detection in tissue sections using AFM," *Archives of Biochemistry and Biophysics*, vol. 518, no. 2, pp. 151–156, 2012.
- [162] M. Plodinec, M. Loparic, C. A. Monnier et al., "The nanomechanical signature of breast cancer," *Nature Nanotechnology*, vol. 7, no. 11, pp. 757–765, 2012.
- [163] S. Suresh, "Biomechanics and biophysics of cancer cells," *Acta Biomaterialia*, vol. 3, no. 4, pp. 413–438, 2007.
- [164] I. Chasiotis, H. L. Fillmore, and G. T. Gillies, "Atomic force microscopy measurement of cytostructural elements involved in the nanodynamics of tumour cell invasion," *Nanotechnology*, vol. 14, no. 5, pp. 557–561, 2003.
- [165] H. L. Fillmore, I. Chasiotis, S. W. Cho, and G. T. Gillies, "Atomic force microscopy observations of tumour cell invadopodia: novel cellular nanomorphologies on collagen substrates," *Nanotechnology*, vol. 14, no. 1, pp. 73–76, 2003.
- [166] D. J. Müller and Y. F. Dufrene, "Atomic force microscopy: a nanoscopic window on the cell surface," *Trends in Cell Biology*, vol. 21, no. 8, pp. 461–469, 2011.
- [167] T. Jung, D. Castellana, P. Klingbeil et al., "CD44v6 dependence of premetastatic niche preparation by exosomes," *Neoplasia*, vol. 11, no. 10, pp. 1093–IN17, 2009.
- [168] H. Peinado, M. Alečković, S. Lavotshkin et al., "Melanoma exosomes educate bone marrow progenitor cells toward a pro-metastatic phenotype through MET," *Nature Medicine*, vol. 18, no. 6, pp. 883–891, 2012.
- [169] D. D. Taylor and C. Gercel-Taylor, "MicroRNA signatures of tumor-derived exosomes as diagnostic biomarkers of ovarian cancer," *Gynecologic Oncology*, vol. 110, no. 1, pp. 13–21, 2008.
- [170] S. Sharma, K. Das, J. Woo, and J. K. Gimzewski, "Nanofilaments on glioblastoma exosomes revealed by peak force microscopy," *Journal of the Royal Society Interface*, vol. 11, no. 92, 2014.
- [171] T. Ludwig, R. Kirmse, and K. Poole, "Challenges and approaches-probing tumor cell invasion by atomic force microscopy," in *Modern Research and Educational Topics in Microscopy*, Formatex, A. Méndez-Vilas and J. Díaz, Eds., pp. 11–22, 2007.
- [172] S. Kusick, H. Bertram, H. Oberleithner, and T. Ludwig, "Nanoscale imaging and quantification of local proteolytic activity," *Journal of Cellular Physiology*, vol. 204, no. 3, pp. 767–774, 2005.
- [173] T. Ludwig, "Local proteolytic activity in tumor cell invasion and metastasis," *BioEssays*, vol. 27, no. 11, pp. 1181–1191, 2005.
- [174] A. V. Taubenberger, V. M. Quent, L. Thibaudeau, J. A. Clements, and D. W. Huttmacher, "Delineating breast

- cancer cell interactions with engineered bone microenvironments,” *Journal of Bone and Mineral Research*, vol. 28, no. 6, pp. 1399–1411, 2013.
- [175] S. Park, L. Bastatas, J. Matthews, and Y. J. Lee, “Mechanical responses of cancer cells on nanoscaffolds for adhesion size control,” *Macromolecular Bioscience*, vol. 15, no. 6, pp. 851–860, 2015.
- [176] P. H. Puech, K. Poole, D. Knebel, and D. J. Muller, “A new technical approach to quantify cell–cell adhesion forces by AFM,” *Ultramicroscopy*, vol. 106, no. 8-9, pp. 637–644, 2006.
- [177] V. M. Laurent, A. Duperray, V. Sundar Rajan, and C. Verdier, “Atomic force microscopy reveals a role for endothelial cell ICAM-1 expression in bladder cancer cell adherence,” *PLoS One*, vol. 9, no. 5, article e98034, 2014.
- [178] S. C. Hoffmann, A. Cohnen, T. Ludwig, and C. Watzl, “2B4 engagement mediates rapid LFA-1 and actin-dependent NK cell adhesion to tumor cells as measured by single cell force spectroscopy,” *Journal of Immunology*, vol. 186, no. 5, pp. 2757–2764, 2011.
- [179] M. F. Coughlin, D. R. Bielenberg, G. Lenormand et al., “Cytoskeletal stiffness, friction, and fluidity of cancer cell lines with different metastatic potential,” *Clinical and Experimental Metastasis*, vol. 30, no. 3, pp. 237–250, 2013.
- [180] M. Plodinec and R. Y. H. Lim, “Nanomechanical characterization of living mammary tissues by atomic force microscopy,” in *Mammary Stem Cells*, M. Vivanco, Ed., vol. 1293 of *Methods in Molecular Biology*, pp. 231–246, Humana Press, New York, NY, USA, 2015.
- [181] A. Fuhrmann, J. R. Staunton, V. Nandakumar, N. Banyai, P. C. W. Davies, and R. Ros, “AFM stiffness nanotomography of normal, metaplastic and dysplastic human esophageal cells,” *Physical Biology*, vol. 8, no. 1, article 015007, 2011.
- [182] K. Hayashi and M. Iwata, “Stiffness of cancer cells measured with an AFM indentation method,” *Journal of the Mechanical Behavior of Biomedical Materials*, vol. 49, pp. 105–111, 2015.
- [183] W. H. Goldmann and R. M. Ezzell, “Viscoelasticity in wild-type and vinculin-deficient (5.51) mouse F9 embryonic carcinoma cells examined by atomic force microscopy and rheology,” *Experimental Cell Research*, vol. 226, no. 1, pp. 234–237, 1996.
- [184] W. H. Goldmann, R. Galneder, M. Ludwig et al., “Differences in elasticity of vinculin-deficient F9 cells measured by magnetometry and atomic force microscopy,” *Experimental Cell Research*, vol. 239, no. 2, pp. 235–242, 1998.
- [185] M. Lekka, P. Laidler, D. Gil, J. Lekki, Z. Stachura, and A. Z. Hryniewicz, “Elasticity of normal and cancerous human bladder cells studied by scanning force microscopy,” *European Biophysics Journal*, vol. 28, no. 4, pp. 312–316, 1999.
- [186] M. Lekka, J. Lekki, M. Marszałek et al., “Local elastic properties of cells studied by SFM,” *Applied Surface Science*, vol. 141, no. 3-4, pp. 345–349, 1999.
- [187] Q. S. Li, G. Y. H. Lee, C. N. Ong, and C. T. Lim, “AFM indentation study of breast cancer cells,” *Biochemical and Biophysical Research Communications*, vol. 374, no. 4, pp. 609–613, 2008.
- [188] E. C. Faria, N. Ma, E. Gazi et al., “Measurement of elastic properties of prostate cancer cells using AFM,” *Analyst*, vol. 133, no. 11, pp. 1498–1500, 2008.
- [189] Z. L. Zhou, A. H. W. Ngan, B. Tang, and A. X. Wang, “Reliable measurement of elastic modulus of cells by nano-indentation in an atomic force microscope,” *Journal of the Mechanical Behavior of Biomedical Materials*, vol. 8, pp. 134–142, 2012.
- [190] S. E. Cross, Y.-S. Jin, J. Rao, and J. K. Gimzewski, “Nanomechanical analysis of cells from cancer patients,” *Nature Nanotechnology*, vol. 2, no. 12, pp. 780–783, 2007.
- [191] K. Pogoda, J. Jaczewska, J. Wiltowska-Zuber et al., “Depth-sensing analysis of cytoskeleton organization based on AFM data,” *European Biophysics Journal*, vol. 41, no. 1, pp. 79–87, 2012.
- [192] S. Park and Y. J. Lee, “AFM-based dual nano-mechanical phenotypes for cancer metastasis,” *Journal of Biological Physics*, vol. 40, no. 4, pp. 413–419, 2014.
- [193] K. Levental, H. Yu, L. Kass et al., “Matrix crosslinking forces tumor progression by enhancing integrin signaling,” *Cell*, vol. 139, no. 5, pp. 891–906, 2009.
- [194] M. J. Paszek, N. Zahir, K. R. Johnson et al., “Tensional homeostasis and the malignant phenotype,” *Cancer Cell*, vol. 8, no. 3, pp. 241–254, 2005.
- [195] T. Stylianopoulos, L. L. Munn, and R. K. Jain, “Reengineering the physical microenvironment of tumors to improve drug delivery and efficacy: from mathematical modeling to bench to bedside,” *Trends in Cancer*, vol. 4, no. 4, pp. 292–319, 2018.
- [196] M. Lekka, “Atomic force microscopy: a tip for diagnosing cancer,” *Nature Nanotechnology*, vol. 7, no. 11, pp. 691–692, 2012.
- [197] A. Ansardamavandi, M. Tafazzoli-Shadpour, R. Omidvar, and I. Jahanzad, “Quantification of effects of cancer on elastic properties of breast tissue by atomic force microscopy,” *Journal of the Mechanical Behavior of Biomedical Materials*, vol. 60, pp. 234–242, 2016.
- [198] J. I. Lopez, I. Kang, W. K. You, D. M. McDonald, and V. M. Weaver, “In situ force mapping of mammary gland transformation,” *Integrative Biology*, vol. 3, no. 9, pp. 910–921, 2011.
- [199] M. Tian, Y. Li, W. Liu et al., “The nanomechanical signature of liver cancer tissues and its molecular origin,” *Nanoscale*, vol. 7, no. 30, pp. 12998–13010, 2015.
- [200] G. Ciasca, T. E. Sassun, E. Minelli et al., “Nano-mechanical signature of brain tumours,” *Nanoscale*, vol. 8, no. 47, pp. 19629–19643, 2016.
- [201] Y. Cui, X. Zhang, K. You et al., “Nanomechanical characteristics of cervical cancer and cervical intraepithelial neoplasia revealed by atomic force microscopy,” *Medical Science Monitor: International Medical Journal of Experimental and Clinical Research*, vol. 23, pp. 4205–4213, 2017.
- [202] E. Minelli, G. Ciasca, T. E. Sassun et al., “A fully-automated neural network analysis of AFM force-distance curves for cancer tissue diagnosis,” *Applied Physics Letters*, vol. 111, no. 14, article 143701, 2017.
- [203] J. Adamcik and R. Mezzenga, “Study of amyloid fibrils via atomic force microscopy,” *Current Opinion in Colloid & Interface Science*, vol. 17, no. 6, pp. 369–376, 2012.
- [204] S. J. Roeters, A. Iyer, G. Pletikapiä, V. Kogan, V. Subramaniam, and S. Woutersen, “Evidence for intramolecular antiparallel beta-sheet structure in alpha-synuclein fibrils from a combination of two-dimensional infrared spectroscopy and atomic force microscopy,” *Scientific Reports*, vol. 7, no. 1, 2017.

- [205] H. Lei, X. Zhang, J. Hu, and Y. Zhang, "Self-assembly of amyloid-like peptides at interfaces investigated by atomic force microscopy," *Science of Advanced Materials*, vol. 9, no. 1, pp. 65–76, 2017.
- [206] T. Watanabe-Nakayama and K. Ono, "High-speed atomic force microscopy of individual amyloidogenic protein assemblies," in *Nanoscale Imaging*, Y. Lyubchenko, Ed., vol. 1814 of *Methods in Molecular Biology*, pp. 201–212, Humana Press, New York, NY, USA, 2018.
- [207] S. W. Han, T. H. Lee, M. S. Kang, H. J. Kim, and H. K. Shin, "Probing amyloid β and the antibody interaction using atomic force microscopy," *Journal of Nanoscience and Nanotechnology*, vol. 18, no. 2, pp. 1410–1413, 2018.
- [208] E. Drolle, F. Hane, B. Lee, and Z. Leonenko, "Atomic force microscopy to study molecular mechanisms of amyloid fibril formation and toxicity in Alzheimer's disease," *Drug Metabolism Reviews*, vol. 46, no. 2, pp. 207–223, 2014.
- [209] A. P. Shivji, M. C. Davies, C. J. Roberts, S. J. B. Tendler, and M. J. Wilkinson, "Molecular surface morphology studies of β -amyloid self-assembly: effect of pH on fibril formation," *Protein and Peptide Letters*, vol. 3, no. 6, pp. 407–414, 1996.
- [210] W. B. Stine Jr, S. W. Snyder, U. S. Lador et al., "The nanometer-scale structure of amyloid- β visualized by atomic force microscopy," *Protein Journal*, vol. 15, no. 2, pp. 193–203, 1996.
- [211] G. S. Shekhawat, M. P. Lambert, S. Sharma et al., "Soluble state high resolution atomic force microscopy study of Alzheimer's β -amyloid oligomers," *Applied Physics Letters*, vol. 95, no. 18, article 183701, 2009.
- [212] G. M. Mustata, G. S. Shekhawat, M. P. Lambert et al., "Insights into the mechanism of Alzheimer's β -amyloid aggregation as a function of concentration by using atomic force microscopy," *Applied Physics Letters*, vol. 100, no. 13, article 133704, 2012.
- [213] L. Connelly, H. Jang, F. Teran Arce et al., "Atomic force microscopy and MD simulations reveal pore-like structures of all-d-enantiomer of Alzheimer's β -amyloid peptide: relevance to the ion channel mechanism of AD pathology," *Journal of Physical Chemistry B*, vol. 116, no. 5, pp. 1728–1735, 2012.
- [214] E. Drolle, K. Hammond, F. T. Hane, B. Lee, and Z. Leonenko, "Atomic Force Microscopy and Kelvin Probe Force Microscopy to Study Molecular Mechanism of Alzheimer's Disease," in *International Conference on Scanning Probe Microscopy on Soft and Polymeric Materials*, Ontario, Canada, September 2014.
- [215] S. Song, X. Ma, Y. Zhou, M. Xu, S. Shuang, and C. Dong, "Studies on the interaction between vanillin and β -amyloid protein via fluorescence spectroscopy and atomic force microscopy," *Chemical Research in Chinese Universities*, vol. 32, no. 2, pp. 172–177, 2016.
- [216] S. W. Han, H. K. Shin, and T. Adachi, "Nanolithography of amyloid precursor protein cleavage with β -secretase by atomic force microscopy," *Journal of Biomedical Nanotechnology*, vol. 12, no. 3, pp. 546–553, 2016.
- [217] N. Li, H. Jang, M. Yuan et al., "Graphite-templated amyloid nanostructures formed by a potential pentapeptide inhibitor for Alzheimer's disease: a combined study of real-time atomic force microscopy and molecular dynamics simulations," *Langmuir*, vol. 33, no. 27, pp. 6647–6656, 2017.
- [218] P. J. de Pablo, "Atomic force microscopy of virus shells," *Seminars in Cell & Developmental Biology*, vol. 73, pp. 199–208, 2018.
- [219] F. Moreno-Madrid, N. Martín-González, A. Llauro et al., "Atomic force microscopy of virus shells," *Biochemical Society Transactions*, vol. 45, no. 2, pp. 499–511, 2017.
- [220] M. G. Mateu, "Mechanical properties of viruses analyzed by atomic force microscopy: a virological perspective," *Virus Research*, vol. 168, no. 1-2, pp. 1–22, 2012.
- [221] A. M. Baró, R. Miranda, J. Alamán et al., "Determination of surface topography of biological specimens at high resolution by scanning tunnelling microscopy," *Nature*, vol. 315, no. 6016, pp. 253–254, 1985.
- [222] Y. G. Kuznetsov, A. J. Malin, R. W. Lucas, M. Plomp, and A. McPherson, "Imaging of viruses by atomic force microscopy," *Journal of General Virology*, vol. 82, no. 9, pp. 2025–2034, 2001.
- [223] Y. G. Kuznetsov and A. McPherson, "Atomic force microscopy in imaging of viruses and virus-infected cells," *Microbiology and Molecular Biology Reviews*, vol. 75, no. 2, pp. 268–285, 2011.
- [224] A. J. Malkin, M. Plomp, and A. McPherson, "Unraveling the architecture of viruses by high-resolution atomic force microscopy," in *DNA Viruses*, P. M. Lieberman, Ed., vol. 292 of *Methods in Molecular Biology*, pp. 85–108, Humana Press, 2005.
- [225] A. McPherson and Y. G. Kuznetsov, "Atomic force microscopy investigation of viruses," in *Atomic Force Microscopy in Biomedical Research*, P. Braga and D. Ricci, Eds., vol. 736 of *Methods in Molecular Biology (Methods and Protocols)*, pp. 171–195, Humana Press, 2011.
- [226] M. Gladnikoff and I. Rouso, "Directly monitoring individual retrovirus budding events using atomic force microscopy," *Biophysical Journal*, vol. 94, no. 1, pp. 320–326, 2008.
- [227] M. Gladnikoff, E. Shimoni, N. S. Gov, and I. Rouso, "Retroviral assembly and budding occur through an actin-driven mechanism," *Biophysical Journal*, vol. 97, no. 9, pp. 2419–2428, 2009.
- [228] W. Häberle, J. K. H. Hörber, F. Ohnesorge, D. P. E. Smith, and G. Binnig, "In situ investigations of single living cells infected by viruses," *Ultramicroscopy*, vol. 42-44, pp. 1161–1167, 1992.
- [229] M. Moloney, L. McDonnell, and H. O'Shea, "Atomic force microscopy analysis of enveloped and non-enveloped viral entry into, and egress from, cultured cells," *Ultramicroscopy*, vol. 100, no. 3-4, pp. 163–169, 2004.
- [230] R. D. Hartschuh, S. P. Wargacki, H. Xiong et al., "How rigid are viruses," *Physical Review E*, vol. 78, no. 2, article 021907, 2008.
- [231] R. Ramalho, S. Rankovic, J. Zhou, C. Aiken, and I. Rouso, "Analysis of the mechanical properties of wild type and hyperstable mutants of the HIV-1 capsid," *Retrovirology*, vol. 13, no. 1, 2016.
- [232] B. K. Ganser, S. Li, V. Y. Klishko, J. T. Finch, and W. I. Sundquist, "Assembly and analysis of conical models for the HIV-1 core," *Science*, vol. 283, no. 5398, pp. 80–83, 1999.
- [233] W. I. Sundquist and H. G. Kräusslich, "HIV-1 assembly, budding, and maturation," *Cold Spring Harbor Perspectives in Medicine*, vol. 2, no. 7, 2012.
- [234] G. Zhao, J. R. Perilla, E. L. Yufenyuy et al., "Mature HIV-1 capsid structure by cryo-electron microscopy and all-atom

- molecular dynamics,” *Nature*, vol. 497, no. 7451, pp. 643–646, 2013.
- [235] H. B. Pang, L. Hevroni, N. Kol et al., “Virion stiffness regulates immature HIV-1 entry,” *Retrovirology*, vol. 10, no. 1, p. 4, 2013.
- [236] N. Kol, Y. Shi, M. Tsvitov et al., “A stiffness switch in human immunodeficiency virus,” *Biophysical Journal*, vol. 92, no. 5, pp. 1777–1783, 2007.
- [237] V. Gkretsi, A. Stylianou, and T. Stylianopoulos, “Vasodilator-stimulated phosphoprotein (VASP) depletion from breast cancer MDA-MB-231 cells inhibits tumor spheroid invasion through downregulation of Migfilin, β -catenin and urokinase-plasminogen activator (uPA),” *Experimental Cell Research*, vol. 352, no. 2, pp. 281–292, 2017.

Research Article

Conformational Distortions of the Red Blood Cell Spectrin Matrix Nanostructure in Response to Temperature Changes *In Vitro*

Elena Kozlova ^{1,2}, Aleksandr Chernysh,^{1,2} Viktoria Sergunova,¹ Ekaterina Manchenko,^{1,2} Viktor Moroz,¹ and Aleksandr Kozlov²

¹V.A. Negovsky Research Institute of General Reanimatology, Federal Research and Clinical Center of Intensive Care Medicine and Rehabilitology, 107031, 25 Petrovka St., Build. 2, Moscow, Russia

²Sechenov First Moscow State Medical University (Sechenov University), 119991, 2-4 Bolshaya Pirogovskaya St, Moscow, Russia

Correspondence should be addressed to Elena Kozlova; waterlake@mail.ru

Received 2 December 2018; Revised 18 February 2019; Accepted 27 February 2019; Published 6 May 2019

Guest Editor: Andreas Stylianou

Copyright © 2019 Elena Kozlova et al. This is an open access article distributed under the Creative Commons Attribution License, which permits unrestricted use, distribution, and reproduction in any medium, provided the original work is properly cited.

The spectrin matrix is a structural element of red blood cells (RBCs). As such, it affects RBC morphology, membrane deformability, nanostructure, stiffness, and, ultimately, the rheological properties of blood. However, little is known about how temperature affects the spectrin matrix. In this study, the nanostructure of the spectrin network was recorded by atomic force microscopy. We describe how the nanostructure of the RBC spectrin matrix changes from a regular network to a chaotic pattern following an increase in temperature from 20 to 50°C. At 20–37°C, the spectrin network formed a regular structure with dimensions of typically 150 ± 60 nm. At 42–43°C, 83% of the spectrin network assumed an irregular structure. Finally, at 49–50°C the chaotic pattern was observed, and no quantitative estimates of the spectrin structure's parameters could be made. These results can be useful for biophysical studies on the destruction of the spectrin network under pathological conditions, as well as for investigating cell morphology and blood rheology in different diseases.

1. Introduction

Red blood cell (RBC) morphology, membrane deformability, and nanostructure are largely related to the structure of the cytoskeleton underlying the lipid bilayer [1–3]. The spectrin matrix is thought to be a critical structural component of RBCs [4].

Temperature represents an important factor affecting the functioning of biological objects. An increase in temperature causes conformational distortions of the RBC spectrin matrix [5] and changes the rheological properties of blood [6].

Various methods have been applied to study the RBC spectrin matrix [7–9]. Recently, atomic force microscopy (AFM) has been used to visualise blood cells and study the properties of their membranes. AFM is particularly effective for studying the nanostructure of biological objects up to several nanometres in size [10–22].

External factors, such as ionizing radiation [23], drugs [24, 25], or long-term storage of packed RBCs [26], as well

as genetic mutations [27] can damage both protein and lipid components of the membrane. This is then followed by damage to the spectrin matrix. Understanding how the RBC spectrin network behaves under different physical and chemical insults remains an important scientific and clinical challenge.

The purpose of the present study was to apply AFM to investigate the influence of temperature on conformational distortions of the RBC spectrin matrix nanostructure *in vitro*.

2. Materials and Methods

2.1. Experimental Setup. Experimental work was carried out according to the following scheme:

- (1) Development of the ghost preparation method for spectrin matrix identification
- (2) Acquisition of spectrin network AFM images

- (3) Investigation of the influence of the physical factor (temperature) on cells
- (4) Quantitative assessment of spectrin matrix characteristics based on the effect of the above factor

2.2. Preparation of Blood Samples. Blood withdrawal (150 μL) into ethylenediaminetetraacetic acid- (EDTA-) containing microvettes (Sarstedt AG & Co., Germany) was carried out during a prophylactic examination on eight volunteers (25–35 years old, four women and four men). Informed consent was obtained from each donor. All experiments were carried out in accordance with guidelines and regulations of the Federal Research and Clinical Centre of Intensive Care Medicine and Rehabilitology, V.A. Negovsky Scientific Research Institute of General Reanimatology, Moscow, Russian Federation. All experimental protocols were approved by this Institute.

2.3. Temperature Adjustment. Microvettes containing blood samples were put into a hot-air thermostat TC-1/80 (SKTB SPU, Russian Federation) and incubated for 30 min at a given temperature. The temperature ranges were as follows: 20°C, 36–37°C, 39–40°C, 42–43°C, and 49–50°C.

2.4. Formation of the Spectrin Matrix on the Surface of RBC Ghosts. For the sake of clarity, we defined the term RBC ghost as the membrane and cytoskeletal elements of the RBC devoid of cytoplasmic contents. In our experiments, lipid fractions were removed from the RBC ghosts and the spectrin matrix appeared on the surface.

Figure 1 illustrates the formation of RBC ghosts and exposure of spectrin matrix. Cells were first subjected to haemolysis (Figure 1(a)), whereby 150 μL of fresh blood was added to 500 μL hypotonic solution consisting of one part 0.9% NaCl (Kelun, Kazpharm, Kazakhstan) and nine parts of distilled water. This initiated RBC haemolysis (Figure 1(b)). The resulting suspension was centrifuged in an Eppendorf tube (Ningbo Greetmed Medical Instruments Co., China) at 3,000 rpm for 5 min. The supernatant was removed, and a pellet of 75 μL was left in the tube. Then, 300 μL of distilled water was added to the suspension to continue haemolysis and the suspension was mixed. The resulting lysate was centrifuged at 500 rpm for 5 min. After a soft centrifugation, the Eppendorf tube with the suspension was left in the refrigerator at 4°C for 30 min and then at 20°C for 10 min to continue with haemolysis. The Eppendorf tube containing the ghost suspension was finally centrifuged at 3,000 rpm for 5 min. Once the supernatant was removed, a pellet of 75 μL was left at the bottom of the tube and 10 μL of it was placed on a glass slide. Smears of RBC ghosts' monolayers were prepared using a device-assisted V-Sampler (Vision Hema, Austria). Given the progressive removal of lipids during haemolysis (Figures 1(b) and 1(c)), the spectrin matrix was now exposed in RBC ghost smears (Figure 1(d)).

The use of RBC ghosts to expose the spectrin matrix on the membrane surface has been reported previously [18]. Here, only physical means were applied to achieve spectrin matrix exposure: osmosis (0.9% NaCl and distilled H_2O), centrifugal force (3,000 rpm), and temperature (20°C and 4°C). We did not use any chemical agents for preparation

of RBC ghosts—neither glutaraldehyde nor triton, etc., in order to avoid additional chemical influence on the protein-lipid structures of the membrane.

The extracellular (outer surface) and cytoplasmic (inner surface) structures of the plasma membrane can be studied by various methods [18, 28]. The spectrin matrix on the extracellular surface of the membrane is shown schematically in Figures 1(b) and 1(d) (arrow A) and Figure 2(a) (arrow A). The spectrin matrix on the cytoplasmic surface of the membrane is shown schematically in Figures 1(b) and 1(d) (arrow B) and Figure 2(b) (arrow B). The structure of the spectrin matrix on the inner side of the membrane can be observed following a shift in the ZZ plane (Figures 1(b), 2(a), and 2(b)).

If the RBC ghost maintained two complete surfaces after all the preparation steps, then the spectrin matrix on the extracellular membrane surface could be visualised (A, Figures 2(c) and 2(d)). Conversely, if the upper layer was partially removed or shifted during preparation (arrow D, Figure 2(b)), then the inner surface appeared (arrow B, Figure 2(b); B, Figure 2(e)).

Figure 2(c) shows an example of an AFM image of a spectrin matrix obtained on a control blood sample not subjected to any external factor. The typical size of the spectrin network was $S = 150 \pm 60$ nm. Such a basic network was observed in $65 \pm 20\%$ of the extracellular surfaces of RBC ghosts. In $30 \pm 12\%$ of RBC ghosts' surfaces, the network could not be detected. The remaining $5 \pm 2\%$ of RBC ghosts' surfaces had a spectrin network whose dimensions were typically >250 nm (Figure 2(i)). Only 2% of the ghosts' surfaces presented shifted layers (Figure 2(l)).

Observation of the spectrin matrix and its structural characteristics depends on preparation conditions. Accordingly, an increase in the volume of distilled water during the preparation of the spectrin matrix by a factor of 1.5 (up to 500 μL) increased by ten times the number of large spectrin networks (Figures 2(d), 2(g) and 2(j)). An increase in the rotational rate of RBC ghosts to 12,000 rpm led to the rupture of spectrin filaments (Figures 2(e), 2(h), 2(k), and 2(m)) in comparison with the original procedure (Figures 2(c), 2(f), 2(i), and 2(l)) and to 85% of the ghosts having shifted layers (Figure 2(m)). A representative AFM image of the spectrin matrix on the cytoplasmic membrane surface prepared using high-speed centrifugation is shown in Figures 2(e) and 2(h).

2.5. Atomic Force Microscopy. AFM was used to visualise the spectrin matrix and to quantify its characteristics [18, 20]. We used the NTEGRA Prima AFM instrument (NT-MDT Co., Russian Federation) under the semi-contact mode. Cantilevers PPP-NCSTR-10 (Nanosensors, Switzerland) with a force constant of 5 N/m, tip radius of 10–15 nm, and resonance frequency of 76–263 kHz were used. We employed also cantilevers NSG01 (TipsNano, Russian Federation) with a force constant of 5 N/m, tip curvature radius of 10 nm, and resonance frequency of 87–230 kHz. There were 512 or 1024 scanning points within each line of image.

We scanned monolayers of RBCs and RBC ghosts. The scanning fields were $100 \times 100 \mu\text{m}^2$, $40 \times 40 \mu\text{m}^2$, or $10 \times 10 \mu\text{m}^2$. To study the spectrin matrix nanostructure, a

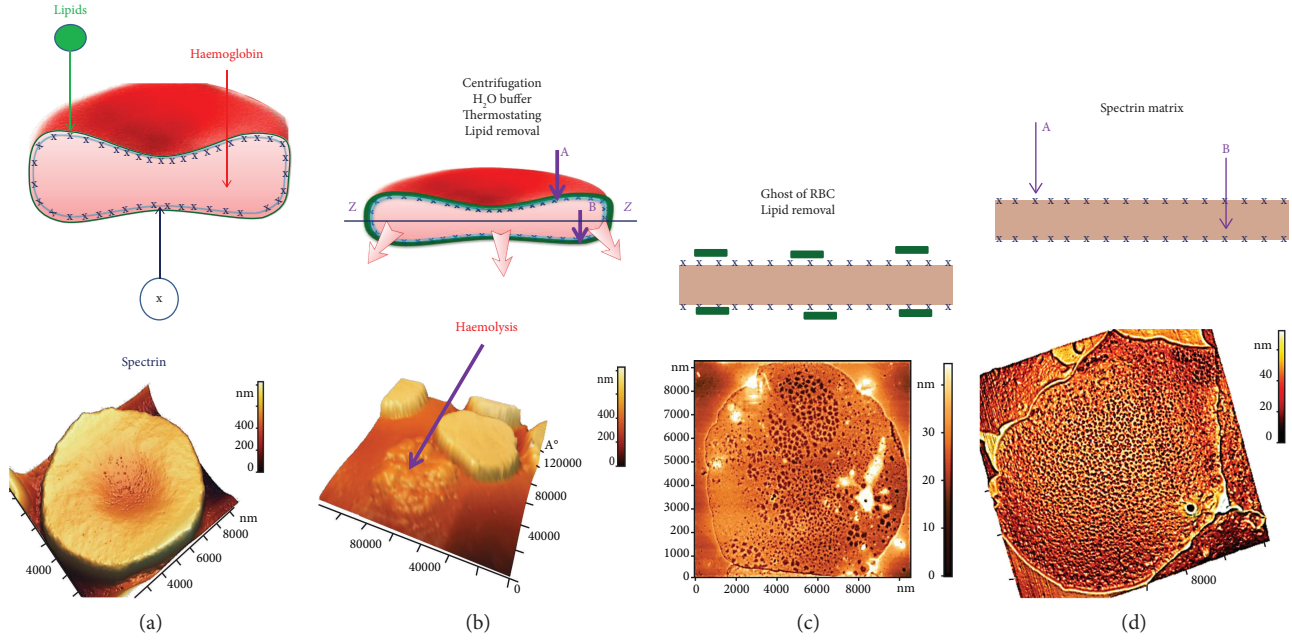


FIGURE 1: Experimental setup for detecting the spectrin matrix: schematic representation and AFM images. (a) RBC prior to treatment, (b) haemolysis and partial removal of lipids, (c) formation of RBC ghosts and lipid removal, and (d) exposure of the spectrin matrix on the ghosts' surface.

membrane surface area of $3 \times 3 \mu\text{m}^2$ was scanned. We analysed 2D and 3D images, as well as the corresponding profiles. For image processing and quantitative assessment of their parameters, we employed the instrument's own NT-MDT SPM software.

2.6. Statistical Analysis. The following groups of RBCs from donors were analysed: control 20°C (eight donors), $36\text{--}37^\circ\text{C}$ (four donors), $39\text{--}40^\circ\text{C}$ (four donors), $42\text{--}43^\circ\text{C}$ (four donors), and $49\text{--}50^\circ\text{C}$ (four donors). The experiments were repeated three times. In each experiment, the corresponding sample (smear) of RBC ghosts was made, amounting to 24 RBC ghost samples for the control and 48 for the different temperature ranges. In total, we obtained 81 samples. AFM images of $100 \times 100 \mu\text{m}^2$ and $40 \times 40 \mu\text{m}^2$ were acquired for each sample and ten RBC ghosts were selected from each of them for quantitative estimation. This yielded a total of 810 RBC ghosts. To estimate nanostructure characteristics, 50 values of sizes (L , S) and height (h) per RBC ghost were measured and taken into account. For each condition, 1800 characteristics were estimated. Statistical analysis of experimental data was performed using OriginPro (OriginLab Corporation, Northampton, Massachusetts, USA). Data represent mean \pm standard deviation (SD). Error bars in Figures 2(i)–2(m), and 3(c) represent the SD.

3. Results

3.1. Local Nanodefects Are Observed in the Spectrin Network. Figure 4 shows some examples of typical defects in spectrin network nanostructure observed during our experiments on the influence of temperature on blood. Normally, each actin complex (blue marker, Figure 4) of the spectrin matrix

comprised six spectrin filaments (yellow lines). However, as shown in Figure 4(a), one connection could occasionally be broken.

Based on AFM images, the characteristic length S of spectrin filaments was estimated as the end-to-end distance between actin nodes, whereas the height h of the nanostructures was determined by the elevation difference between the edge of the hole and its deepest point (Figure 4(b)). The size L of holes in the spectrin matrix was estimated by the surface profile (Figures 4(c), 5(c), 5(d), 6(c), 6(d), 6(g), 6(h), 7(c), and 7(d)).

In a number of cases, we observed the simultaneous disruption of several (3–4) spectrin filaments at contact points with ankyrin complexes (red markers, Figure 4(b)).

In other cases, we observed a broken connection between spectrin filaments and the actin complex. The 3D image of a spectrin matrix element in Figure 4(c) shows six distorted connections to actin filaments forming a cone. The diameter of such local craters was estimated as $L = 300 \pm 100 \text{ nm}$. Disruption of the spectrin filaments led, in turn, to a shortening of the distance between membrane proteins, resulting in their clustering (blue markers fused to each other in Figure 4(d)).

Such nanodefects could appear separately or simultaneously; however, the probability of their occurrence was changed with an increase in temperature. The structures shown in Figure 4(a) may be observed under $36\text{--}37^\circ\text{C}$. The topological structures indicated in Figures 4(b)–4(d) were arisen under $39\text{--}40^\circ\text{C}$.

3.2. The Nanostructure of the RBC Spectrin Matrix Is Influenced by Temperature. As with other biopolymers, the structural properties of spectrin depend on blood temperature. Here, we investigated the spectrin matrix after

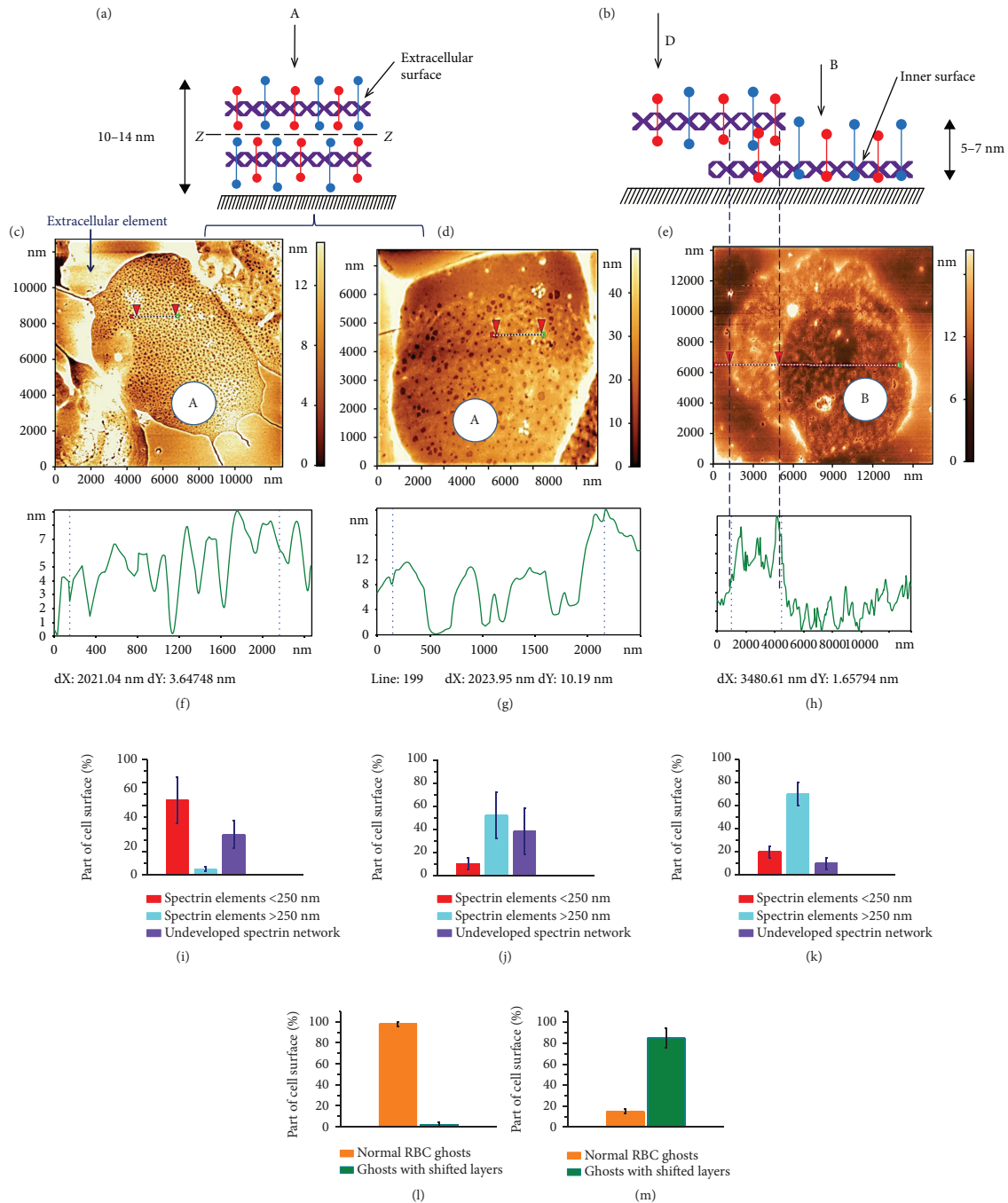


FIGURE 2: Spectrin matrix. (a) Schematic representation of the extracellular membrane surface (arrow A), a dashed line (ZZ) indicates the centre of the membrane. (b) Schematic representation of the inner membrane surface (arrow B) and shifted layer (arrow D). (c) AFM 2D image of the RBC spectrin matrix, $12 \times 12 \mu\text{m}^2$, obtained with optimised preparation parameters: $300 \mu\text{L}$ distilled H_2O and centrifugation at 3,000 rpm. (d) AFM 2D image of the RBC spectrin matrix, $8 \times 12 \mu\text{m}^2$, obtained with $500 \mu\text{L}$ distilled H_2O and centrifugation at 3,000 rpm. (e) AFM 2D image of the RBC spectrin matrix on the cytoplasmic membrane surface, $15 \times 15 \mu\text{m}^2$, obtained with $300 \mu\text{L}$ distilled H_2O and centrifugation at 12,000 rpm. (f–h) Height profiles of the corresponding sections in (c–e). (i–k) Percentage of spectrin network surfaces containing elements <250 nm and >250 nm, as well as with an undeveloped spectrin network as determined in (c–e). (l–m) Percentage of spectrin network on the extracellular membrane surface and with removed or shifted layer: (l) corresponds to (e), and (m) corresponds to (c, d). The dashed line from (b) to (e) delineates the extracellular and inner membrane surfaces. Experimental data are shown as mean \pm SD.

incubating blood at a physiological range of temperatures ($36\text{--}42^\circ\text{C}$), at much higher temperatures ($49\text{--}50^\circ\text{C}$), and at room temperature (20°C).

3.2.1. 20°C . After fresh blood was left in a microvette at 20°C for 30 min, $95 \pm 3\%$ of RBCs appeared as discocytes and a regular spectrin network structure was observed. The typical

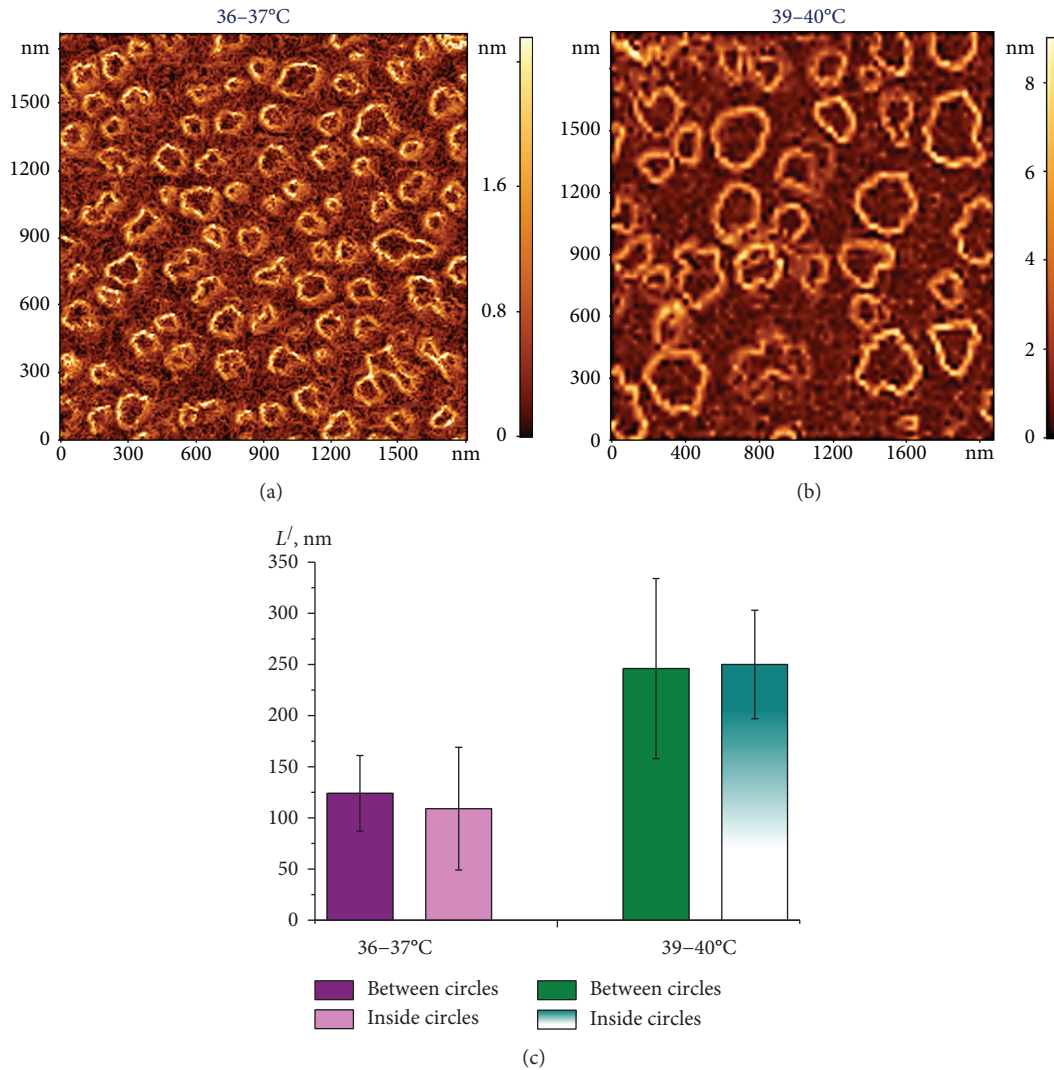


FIGURE 3: AFM 2D image of the $grad h(x,y)$ distribution in the spectrin matrix, $2000 \times 2000 \text{ nm}^2$. (a) At $36\text{--}37^\circ\text{C}$; (b) at $39\text{--}40^\circ\text{C}$; (c) histogram of distance L' (nm) between circles and inside (diameter), as determined in (a) and (b). Experimental data are shown as mean \pm SD.

length of spectrin filaments was $S_{20^\circ\text{C}} = 150 \pm 60 \text{ nm}$, which coincides with that under control conditions. The elevation difference was $h_{20^\circ\text{C}} = 4 \pm 2 \text{ nm}$. Such pattern corresponds to the basic variant of the spectrin matrix.

3.2.2. $36\text{--}37^\circ\text{C}$. Incubation of blood in a thermostat at a physiological temperature of $36\text{--}37^\circ\text{C}$ for 30 min did not change the cells' morphology or the structure of the spectrin matrix as compared to the basic variant (Figures 5(a) and 5(b)).

The spectrin network, with its protein complexes and filaments, was clearly visible (Figures 5(b) and 5(c)) and corresponded to the blue, red, and yellow markers in Figure 4(a). The dark zones corresponded to areas of lipid bilayer destruction (holes). In Figure 5(c), red arrows show the structures between which the parameters were measured. On the profile in Figure 5(d), the corresponding zones are marked by dots. The typical size of a hole was $L_{36\text{--}37^\circ\text{C}} = 150 \pm 60 \text{ nm}$ and the height difference $h_{36\text{--}37^\circ\text{C}} = 4.2 \pm 1.8 \text{ nm}$.

3.2.3. $39\text{--}40^\circ\text{C}$. When blood was incubated at $39\text{--}40^\circ\text{C}$ for 30 min (Figure 6(a)), the morphology of the cells changed. Discocytes amounted to $86 \pm 8\%$ of cells, echinocytes to $6 \pm 1\%$, and target cells (codocytes) to $8 \pm 3\%$ (green arrows, Figure 6). Two spectrin network ensembles were detected: the first (Figures 6(b)–6(d)) corresponded to $37 \pm 6\%$ of cases, the second (Figures 6(f)–6(h)) to $35 \pm 6\%$ of cases, as indicated by a representative 2D image of the spectrin matrix and a fragment of its nanostructure. In ensemble 1, the spectrin matrix displayed a regular structure (Figures 6(b)–6(d)), but the size of network elements was greater than that observed at 20°C and $36\text{--}37^\circ\text{C}$ (Figure 5); specifically, it was calculated as $L_{39\text{--}40^\circ\text{C}(1)} = 240 \pm 60 \text{ nm}$. 2D images (Figures 5(b) and 5(c)) and the corresponding surface profiles (Figure 6(d)) indicated that the entire actin complex was defective. The local topological nanodefects were in the form of a frustum with height $h_{39\text{--}40^\circ\text{C}(1)} = 5.5 \pm 1.5 \text{ nm}$.

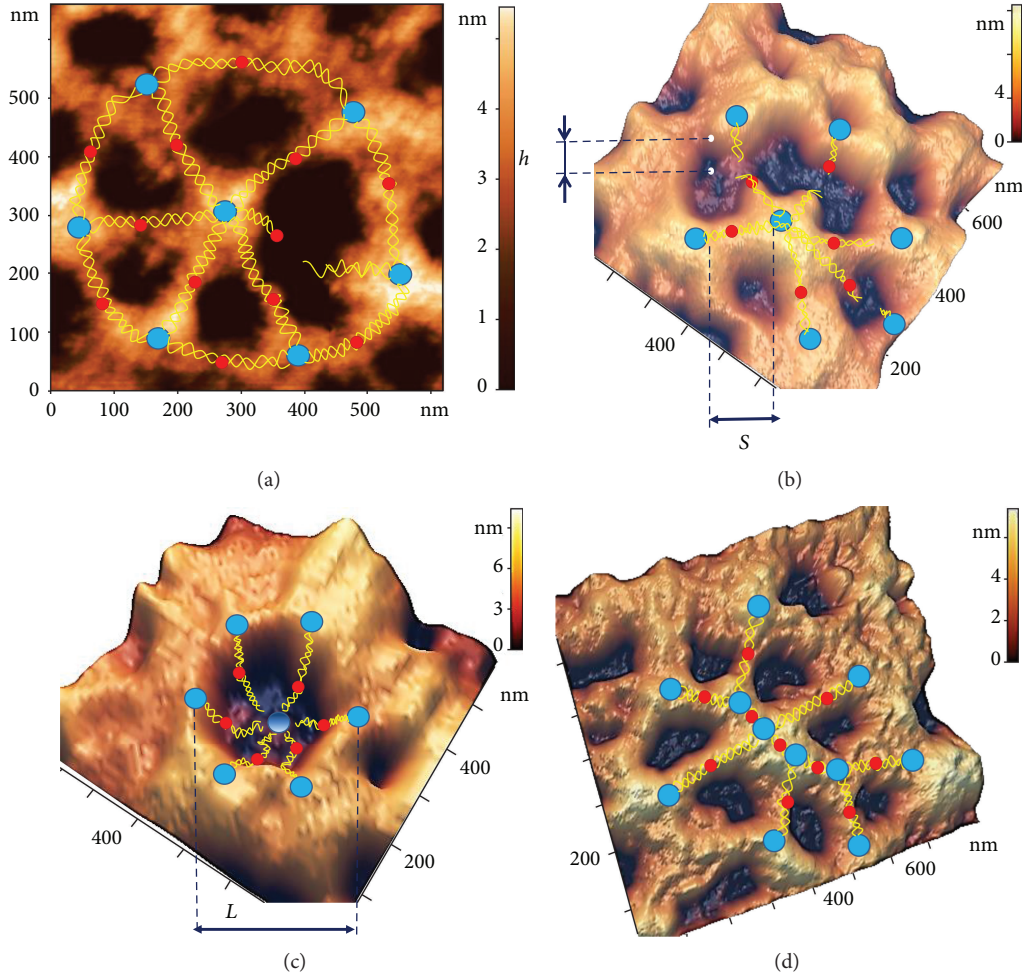


FIGURE 4: Examples of typical local nanodefects in the spectrin network. (a) AFM 2D image, $660 \times 660 \text{ nm}^2$, of a basic spectrin matrix element, with a broken ankyrin (red) connection. (b) AFM 3D image, $700 \times 700 \text{ nm}^2$, of a spectrin network element with three distorted ankyrin connections. (c) AFM 3D image, $600 \times 600 \text{ nm}^2$, of a spectrin matrix element, in which the connection between six spectrin filaments (yellow lines) and an actin complex (blue) is broken, resulting in the formation of a local topological crater-like dip. (d) AFM 3D image, $800 \times 800 \text{ nm}^2$, of a spectrin network element showing clustering of protein complexes.

In some zones of the spectrin network, another type of connection distortion could be detected, namely, discontinuities in the ankyrin complex that resulted in a partial ring structure (Figures 4(b) and 6(c)). The discontinuity of several neighbouring connections at this temperature range was higher than at $36\text{--}37^\circ\text{C}$.

Ensemble 2 displayed an irregular, disordered structure of the spectrin matrix (Figures 6(f)–6(h)), which differed from the ordered network observed previously (Figures 5(b) and 5(c)). In ensemble 2, typical distances showed a wide dispersion, with $L_{39-40^\circ\text{C}(2)} = 220 \pm 160 \text{ nm}$ and $h_{39-40^\circ\text{C}(2)} = 2.6 \pm 1.2 \text{ nm}$.

3.2.4. $42\text{--}43^\circ\text{C}$. A temperature increase to $42\text{--}43^\circ\text{C}$ resulted in target cells in the monolayer increasing to $25 \pm 8\%$ (Figure 6(e)). The proportion of ensemble 2-type spectrin matrix (Figures 6(f) and 6(g)) also increased to $83 \pm 8\%$. The typical parameters of the spectrin nanostructure were $L_{42-43^\circ\text{C}(2)} = 220 \pm 120 \text{ nm}$ and $h_{39-40^\circ\text{C}(2)} = 5 \pm 3 \text{ nm}$. Moreover, the

spectrin matrix was not uniformly irregular across the entire surface of the network. Specifically, it appeared less irregular towards the centre of the cell, in line with the target structure.

3.2.5. $49\text{--}50^\circ\text{C}$. This is the temperature of spectrin denaturation [29]. Total damage to spectrin filaments can lead to alterations in the spectrin matrix as a whole, in turn leading to changes in RBC morphology. As shown in Figure 7(a), the shape of RBCs differed from that at $36\text{--}37^\circ\text{C}$ (Figure 5(a)), with discocytes accounting for only $1.0 \pm 0.5\%$ of cells.

AFM images of the spectrin network (Figure 7(b)) revealed marked differences compared to the control (Figure 2(c) and 5(b)), with $79 \pm 6\%$ of the extracellular surface being strongly damaged. A regularly shaped spectrin matrix was not observed, which also means it was impossible to carry out adequate quantitative estimations of its parameters. A chaotic pattern was observed on the surface (Figure 7(c)), whose typical parameters were $L_{49-50^\circ\text{C}} = 250 \pm 150 \text{ nm}$ and $h_{49-50^\circ\text{C}} = 15 \pm 7 \text{ nm}$ (Figure 7(d)). Moreover, protruding structures were

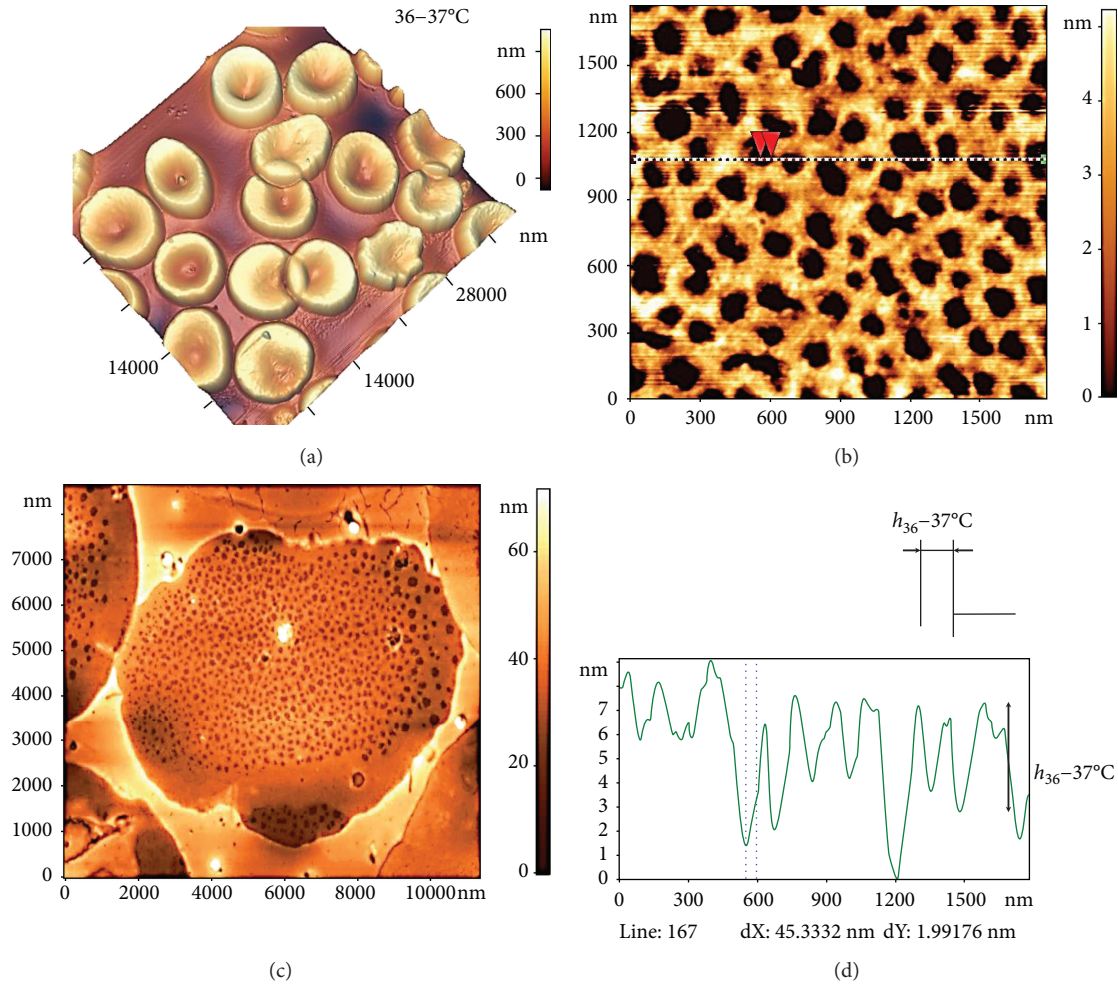


FIGURE 5: Influence of temperature at 36–37°C on spectrin matrix nanostructure. (a) AFM 3D image showing RBC morphology, $38 \times 38 \mu\text{m}^2$. (b) AFM 2D image of the RBC spectrin matrix, $8 \times 8 \mu\text{m}^2$. (c) AFM 2D image of a fragment of the spectrin matrix nanostructure, $1500 \times 1500 \text{ nm}^2$. (d) Height profile along the line indicated in (c), and red arrows correspond to dashed lines on the profile.

observed on the surface, possibly formed by spectrin, proteins, or vesicles.

The shape and geometric parameters of spectrin matrix nanostructures were also estimated based on AFM 2D images reconstructing the gradient distribution of the nanostructure's height over its surface, $\text{grad } h(x, y)$ (Figure 3). Bright outlines represented fields where the $\text{grad } h(x, y)$ value was larger. This occurred in regions where the height changed abruptly, such as where discontinuities and dips in the spectrin network were detected. Conversely, dark areas corresponded to regions where $\text{grad } h(x, y) \approx 0$; that is, the height did not change.

Thus, an increase in the temperature from 36 to 50°C resulted in a substantial transformation of the spectrin matrix nanostructure, from a regular spectrin network to an irregular and disordered pattern. The dynamics of representative spectrin matrix nanostructure transformations as a function of increasing temperature are shown in Figure 8. As blood temperature increased, the percentage of different spectrin matrix configurations on the surface of ghost RBCs changed and is summarised by the histogram in Figure 8(e).

The colours on the histogram correspond to the markers on the AFM 2D images shown in Figures 8(a)–8(d).

Going from 20 to 50°C, the percentage of spectrin networks whose elements were $< 250 \text{ nm}$ dropped from $75 \pm 10\%$ (20–36°C) to $18 \pm 8\%$ (39–40°C) and finally to $1.0 \pm 0.3\%$ (49–50°C).

The change in spectrin matrix nanostructure was associated with a disruption of the connections between spectrin filaments and membrane proteins, topological dips and clustering of membrane proteins, and spectrin denaturation. The probability of these processes varied with temperature, which led to a certain dynamics in network configurations.

4. Discussion

In the present study, we performed *in vitro* biophysical experiments to show specific topological nanodefects in the spectrin matrix under varying blood temperature conditions. Temperature is the main factor in the study of any material as it affects intermolecular interactions and, thus, *phase transition* of matter. Temperature is particularly

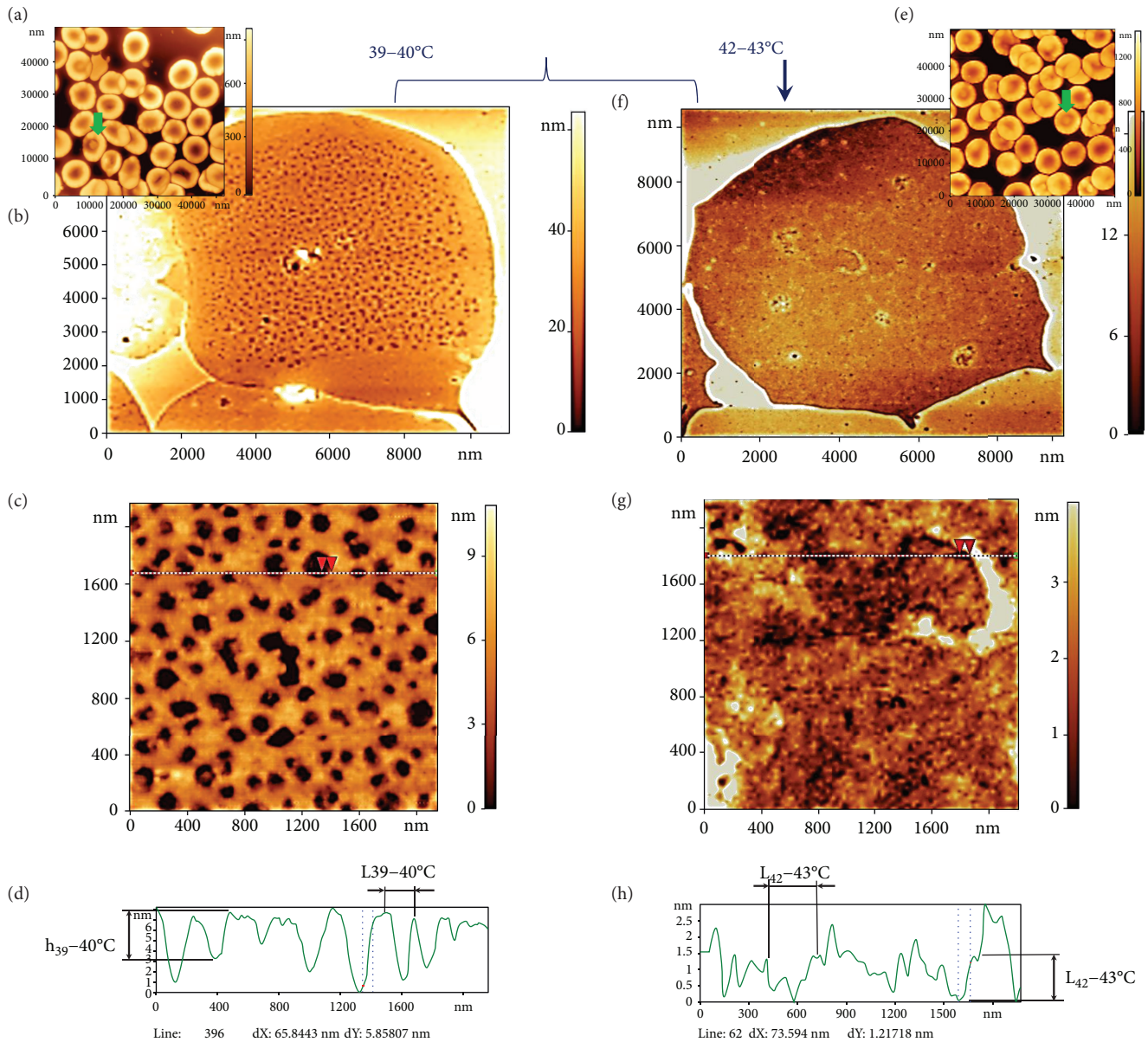


FIGURE 6: Influence of temperature at 39–40°C and 42–43°C on spectrin matrix nanostructure. (a, e) AFM 3D images of RBC morphology, $38 \times 38 \mu\text{m}^2$ and $60 \times 60 \mu\text{m}^2$. (b, f) AFM 2D images of the spectrin matrix, $12 \times 12 \mu\text{m}^2$. (c, g) AFM 2D images of a fragment of the spectrin matrix nanostructure, $2000 \times 2000 \text{ nm}^2$. (d) Height profile along the lines indicated in (c, h, g). Red arrows correspond to dashed lines on the profile. The curly bracket unites possible variants of RBC ghosts and spectrin matrix at 39–40°C. The vertical arrow shows a ghost RBC variant and the spectrin matrix at 42–43°C. Ensemble 1 of RBC ghosts corresponds to (b–d). Ensemble 2 of RBC ghosts corresponds to (f–h).

important for biological molecules, such as polymers and biopolymers, of which spectrin is an example [30]. A key point addressed by the present work was the influence of temperature in the physiological range (36–42°C) on the spectrin matrix structure.

Spectrin is the main protein of the spectrin matrix; it is made of a fibrillar molecule with a length of 180–200 nm and a thickness of 2–3 nm [31]. The spectrin molecule consists of two large alpha and beta polypeptide chains, associated in the antiparallel direction, and with a length of 100 nm. Dimers are self-associated into tetramers, and these interact with ankyrin. The binding of ankyrin to the cytoplasmic domain enables the attachment of the cytoskeleton to the

plasma membrane (Figure 4). At its end, the tetramer binds the protein band 4.1 and the short actin filament, forming a network [32, 33].

Under normal physiological conditions (36–37°C), most of the spectrin matrix nanostructure (>70%) forms a regular network with spacing comparable to the length of spectrin filaments (Figures 5, 8(a), and 8(e)). Higher physiological temperatures (39–40°C) result in a transitional state (Figure 6, 8(b), 8(c), and 8(e)), whereby only 20% of the spectrin matrix forms a regular network and 40% forms an ordered structure but with spacing greater than in the control, and the remaining spectrin matrix is found in an irregular structure that does not resemble a network.

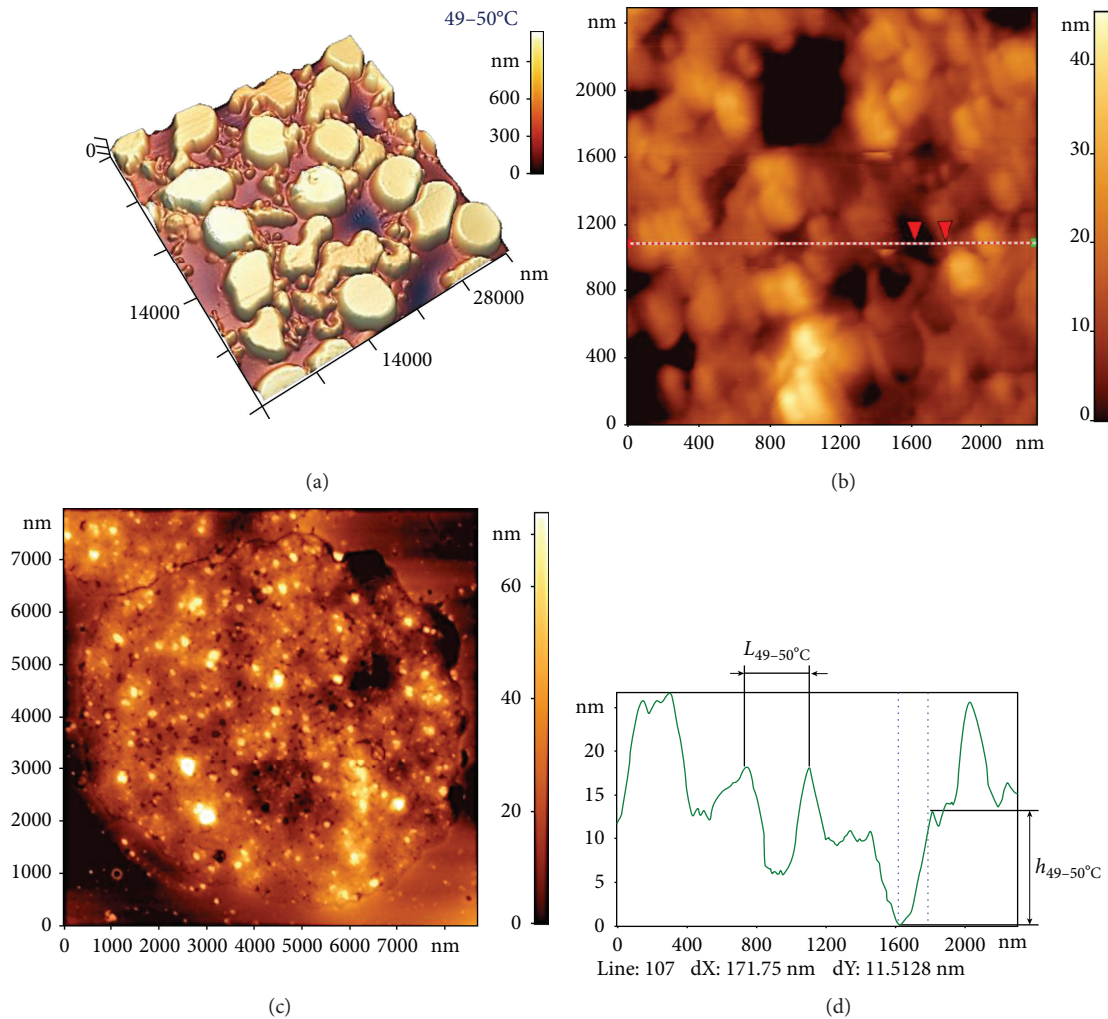


FIGURE 7: Influence of temperature at 49–50°C on the spectrin matrix nanostructure. (a) AFM 3D image showing RBC morphology, $38 \times 38 \mu\text{m}^2$. (b) AFM 2D image of the distorted spectrin network, $8 \times 8 \mu\text{m}^2$. (c) AFM 2D images of a fragment of the distorted spectrin matrix nanostructure (chaotic pattern), $2300 \times 2300 \text{ nm}^2$. (d) Height profile along the line indicated in (c). Red arrows correspond to dashed lines on the profile.

The consequence of this distribution may be a change in the cells' morphology and altered blood rheology. Finally, at 42–43°C, almost 95% of the spectrin matrix forms an irregular structure.

Special attention was given to temperature in the range of 49–50°C, at which spectrin denaturation occurs [29]. This leads to the RBC membrane *in vitro* to lose its stability [29]. In this case, the spectrin matrix is in a chaotic state in almost all RBC ghosts (Figure 7, 8(d), and 8(e)), making it impossible to adequately quantify the parameters of the spectrin structure.

All these processes and measurements are of a statistical nature, explaining why at 39–40°C regular networks and irregular structures are observed simultaneously, whereas at 36–37°C most of the spectrin matrix has a regular and periodically spaced structure, and at 49–50°C it acquires a clearly irregular structure.

An increase in temperature can cause rupture of the bonds in the spectrin matrix, akin to that observed following the action of toxic and oxidative factors. Changes to the

nanostructure of the spectrin matrix will lead to different outcomes, depending on whether the factor acts on actin [34] or ankyrin junctions [35, 36].

Local alterations to the spectrin matrix arising from changes in blood temperature are potential active centres for local topological defects in RBC membranes. Similar local topological defects were observed following the action of pharmacological agents, ionizing radiation, and long-term storage of blood [15, 23, 25, 37], resulting in alterations to the biophysical processes in RBCs.

A change in the spectrin matrix can alter the rheological properties of blood. Previous studies have investigated the relationship between the mechanical properties of RBCs and the structural basis of the spectrin matrix. For example, they have explored the correlation between the size of the cytoskeleton network and stiffening of the cells [3]. The membrane skeleton is assumed to be responsible for maintaining the shape of the erythrocyte and permitting the large deformations that allow it to survive repeated passage through narrow capillaries [4]. The reversible

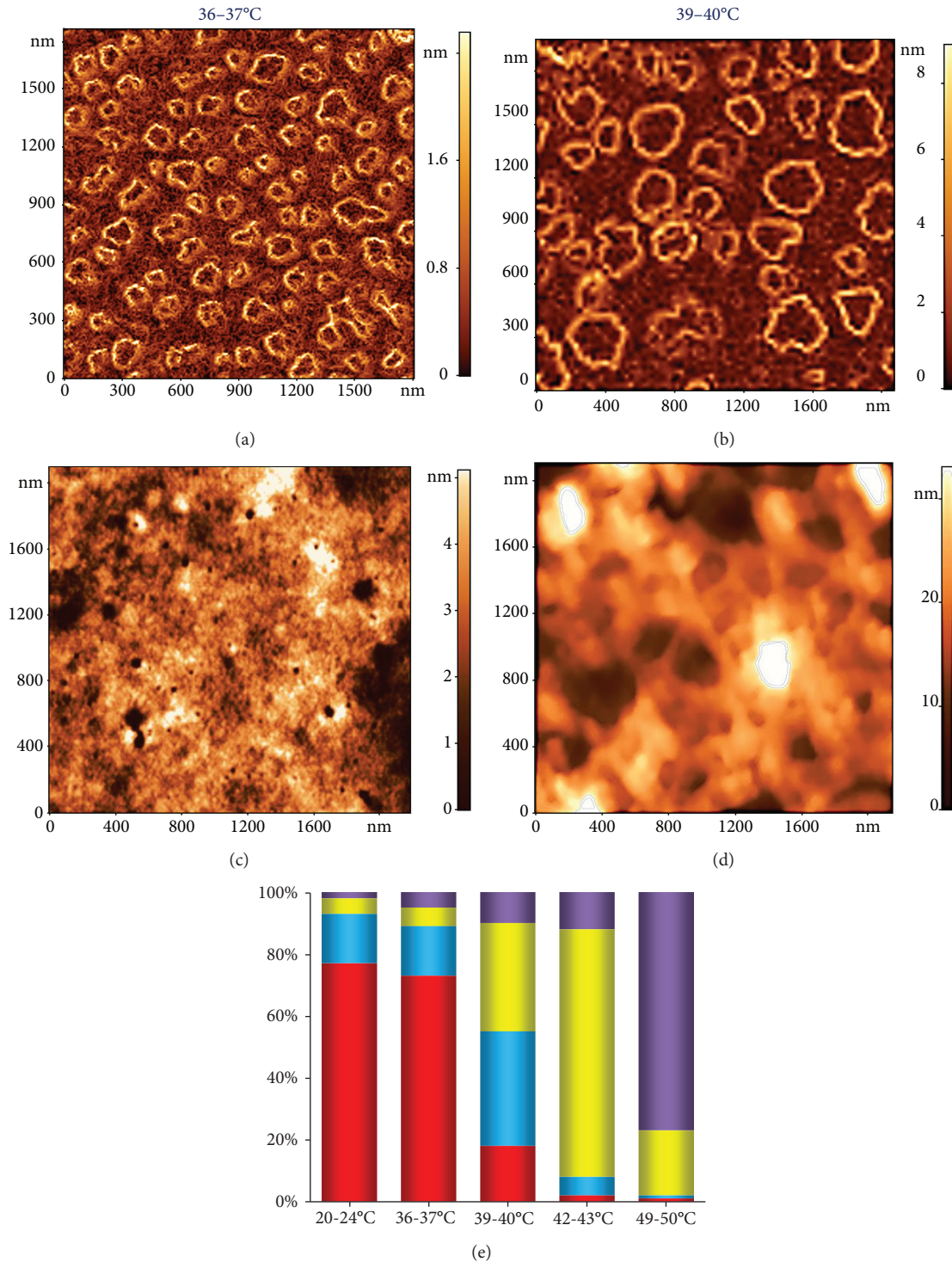


FIGURE 8: AFM 2D images showing the basic typical variants of the spectrin matrix nanostructure, $2000 \times 2000 \text{ nm}^2$. (a) Regular spectrin network with a typical element $< 250 \text{ nm}$ (red square). (b) Regular spectrin network with enlarged deep spectrin matrix elements $> 250 \text{ nm}$ (blue square). (c) Irregular structure (yellow square). (d) Chaotic pattern (purple square). (e) Histogram showing the percentage of each of the structures in (a–d) at various temperatures ($20\text{--}24^\circ\text{C}$, $36\text{--}37^\circ\text{C}$, $39\text{--}40^\circ\text{C}$, $42\text{--}43^\circ\text{C}$, and $49\text{--}50^\circ\text{C}$); colours correspond to those in (a–d). Experimental data are shown as mean values.

rearrangement of the spectrin network has been shown to allow rapid and large deformations, thus ensuring the mechanical stability of the membrane [28]. Given their role as structural nodes in the membrane skeleton, actin

filaments directly control the biomechanical properties of the RBC membrane [38]. Theoretical studies have also been conducted to establish the relationship between mechanical properties of deformable RBCs and the structure of the

spectrin matrix [30]. At the same time, much remains unclear. In particular, the structure of spectrin *in vivo* and the processes underlying its changes when the membrane is deformed are still awaiting clarification [39].

5. Conclusion

Using direct *in vitro* biophysical experiments under controlled conditions, we show how the nanostructure of the RBC spectrin matrix changes from a regular network to a chaotic pattern with increasing temperature. This study can be used as the basis for understanding how an increase in body temperature can affect RBC membrane nanostructure, morphology, and, ultimately, blood rheology.

Data Availability

The data used to support the findings of this study are included within the article.

Conflicts of Interest

The authors declare that there is no conflict of interest regarding the publication of this article.

Acknowledgments

This work has been supported by the Ministry of Science and Higher Education of the Russian Federation and by the “Russian Academic Excellence Project 5-100.” We would like to thank Editage (<http://www.editage.com>) for English language editing.

References

- [1] V. T. Marchesi and E. Steers, “Selective solubilization of a protein component of the red cell membrane,” *Science*, vol. 159, no. 3811, pp. 203–204, 1968.
- [2] A. Elgsaeter, B. Stokke, A. Mikkelsen, and D. Branton, “The molecular basis of erythrocyte shape,” *Science*, vol. 234, no. 4781, pp. 1217–1223, 1986.
- [3] L. Lai, X. Xu, C. T. Lim, and J. Cao, “Stiffening of red blood cells induced by cytoskeleton disorders: a joint theory-experiment study,” *Biophysical Journal*, vol. 109, no. 11, pp. 2287–2294, 2015.
- [4] A. H. Swihart, J. M. Mikrut, J. B. Ketterson, and R. C. Macdonald, “Atomic force microscopy of the erythrocyte membrane skeleton,” *Journal of Microscopy*, vol. 204, no. 3, pp. 212–225, 2001.
- [5] B. Paarvanova and I. Ivanov, “Effect of hypertonicity on the dynamic state of erythrocyte spectrin network as revealed by thermal dielectroscopy,” *Trakia Journal of Science*, vol. 14, no. 1, pp. 96–102, 2016.
- [6] M. Marinkovic, M. Diez-Silva, I. Pantic, J. J. Fredberg, S. Suresh, and J. P. Butler, “Febrile temperature leads to significant stiffening of *Plasmodium falciparum* parasitized erythrocytes,” *American Journal of Physiology. Cell Physiology*, vol. 296, no. 1, pp. C59–C64, 2009.
- [7] T. J. Byers and D. Branton, “Visualization of the protein associations in the erythrocyte membrane skeleton,” *Proceedings of the National Academy of Sciences of the United States of America*, vol. 82, no. 18, pp. 6153–6157, 1985.
- [8] S. C. Liu, L. H. Derick, and J. Palek, “Visualization of the hexagonal lattice in the erythrocyte membrane skeleton,” *Journal of Cell Biology*, vol. 104, no. 3, pp. 527–536, 1987.
- [9] J. A. Ursitti, D. W. Pumplin, J. B. Wade, and R. J. Bloch, “Ultrastructure of the human erythrocyte cytoskeleton and its attachment to the membrane,” *Cell Motility and the Cytoskeleton*, vol. 19, no. 4, pp. 227–243, 1991.
- [10] A. Stylianou, M. Lekka, and T. Stylianopoulos, “AFM assessing of nanomechanical fingerprints for cancer early diagnosis and classification: from single cell to tissue level,” *Nanoscale*, vol. 10, no. 45, pp. 20930–20945, 2018.
- [11] S. N. Pleskova, E. N. Gorshkova, and R. N. Kriukov, “Dynamics of formation and morphological features of neutrophil extracellular traps formed under the influence of opsonized *Staphylococcus aureus*,” *Journal of Molecular Recognition*, vol. 31, no. 7, article e2707, 2018.
- [12] F. Liu, J. Burgess, H. Mizukami, and A. Ostafin, “Sample preparation and imaging of erythrocyte cytoskeleton with the atomic force microscopy,” *Cell Biochemistry and Biophysics*, vol. 38, no. 3, pp. 251–270, 2003.
- [13] M. Encinar, S. Casado, A. Calzado-Martín et al., “Nanomechanical properties of composite protein networks of erythroid membranes at lipid surfaces,” *Colloids and Surfaces. B, Biointerfaces*, vol. 149, pp. 174–183, 2017.
- [14] H. Wang, X. Hao, Y. Shan, J. Jiang, M. Cai, and X. Shang, “Preparation of cell membranes for high resolution imaging by AFM,” *Ultramicroscopy*, vol. 110, no. 4, pp. 305–312, 2010.
- [15] E. Kozlova, A. Chernysh, V. Moroz, O. Gudkova, V. Sergunova, and A. Kuzovlev, “Transformation of membrane nanosurface of red blood cells under hemin action,” *Scientific Reports*, vol. 4, no. 1, article 6033, 2015.
- [16] M. G. Millholland, R. Chandramohanadas, A. Pizzarro et al., “The malaria parasite progressively dismantles the host erythrocyte cytoskeleton for efficient egress,” *Molecular & Cellular Proteomics*, vol. 10, no. 12, article M111.010678, 2011.
- [17] Y. Shan and H. Wang, “The structure and function of cell membranes examined by atomic force microscopy and single-molecule force spectroscopy,” *Chemical Society Reviews*, vol. 44, no. 11, pp. 3617–3638, 2015.
- [18] M. Takeuchi, H. Miyamoto, Y. Sako, H. Komizu, and A. Kusumi, “Structure of the erythrocyte membrane skeleton as observed by atomic force microscopy,” *Biophysical Journal*, vol. 74, no. 5, pp. 2171–2183, 1998.
- [19] K. Bukara, I. Drvenica, V. Ilić et al., “Comparative studies on osmosis based encapsulation of sodium diclofenac in porcine and outdated human erythrocyte ghosts,” *Journal of Biotechnology*, vol. 240, pp. 14–22, 2016.
- [20] E. Kozlova, A. Chernysh, V. Sergunova, O. Gudkova, E. Manchenko, and A. Kozlov, “Atomic force microscopy study of red blood cell membrane nanostructure during oxidation-reduction processes,” *Journal of Molecular Recognition*, vol. 31, no. 10, article e2724, 2018.
- [21] C. Carelli-Alinovi, S. Dinarelli, B. Sampaolese, F. Misiti, and M. Girasole, “Morphological changes induced in erythrocyte by amyloid beta peptide and glucose depletion: a combined atomic force microscopy and biochemical study,” *Biochimica et Biophysica Acta (BBA) - Biomembranes*, vol. 1861, no. 1, pp. 236–244, 2019.

- [22] E. Kozlova, A. Chernysh, V. Moroz et al., "Opposite effects of electroporation of red blood cell membranes under the influence of zinc ions," *Acta of Bioengineering and Biomechanics*, vol. 14, no. 1, pp. 3–13, 2012.
- [23] E. K. Kozlova, V. A. Sergunova, E. A. Krasavin et al., "Local defects in the nanostructure of the membrane of erythrocytes upon ionizing radiation of blood," *Physics of Particles and Nuclei Letters*, vol. 13, no. 1, pp. 140–148, 2016.
- [24] E. K. Kozlova, A. M. Chernysh, V. V. Moroz, and A. N. Kuzovlev, "Analysis of nanostructure of red blood cells membranes by space Fourier transform of AFM images," *Micron*, vol. 44, pp. 218–227, 2013.
- [25] A. M. Chernysh, E. K. Kozlova, V. V. Moroz et al., "Nonlinear local deformations of red blood cell membranes: effects of toxins and pharmaceuticals (part 2)," *General Reanimatology*, vol. 14, no. 1, pp. 29–39, 2018.
- [26] E. Kozlova, A. Chernysh, V. Moroz, V. Sergunova, O. Gudkova, and E. Manchenko, "Morphology, membrane nanostructure and stiffness for quality assessment of packed red blood cells," *Scientific Reports*, vol. 7, no. 1, article 7846, 2017.
- [27] J. Narla and N. Mohandas, "Red cell membrane disorders," *International Journal of Laboratory Hematology*, vol. 39, no. 1, pp. 47–52, 2017.
- [28] L. Picas, F. Rico, M. Deforet, and S. Scheuring, "Structural and mechanical heterogeneity of the erythrocyte membrane reveals hallmarks of membrane stability," *ACS Nano*, vol. 7, no. 2, pp. 1054–1063, 2013.
- [29] I. T. Ivanov, B. K. Paarvanova, V. Ivanov, K. Smuda, H. Bäumlner, and R. Georgieva, "Effects of heat and freeze on isolated erythrocyte submembrane skeletons," *General Physiology and Biophysics*, vol. 36, no. 02, pp. 155–165, 2017.
- [30] T. G. Fai, A. Leo-Macias, D. L. Stokes, and C. S. Peskin, "Image-based model of the spectrin cytoskeleton for red blood cell simulation," *PLoS Computational Biology*, vol. 13, no. 10, article e1005790, 2017.
- [31] J. W. Brown, E. Bullitt, S. Sriswasdi, S. Harper, D. W. Speicher, and C. J. McKnight, "The physiological molecular shape of spectrin: a compact supercoil resembling a Chinese finger trap," *PLoS Computational Biology*, vol. 11, no. 6, article e1004302, 2015.
- [32] V. Heinrich, K. Ritchie, N. Mohandas, and E. Evans, "Elastic thickness compressibility of the red cell membrane," *Biophysical Journal*, vol. 81, no. 3, pp. 1452–1463, 2001.
- [33] B. Machnicka, A. Czogalla, A. Hryniewicz-Jankowska et al., "Spectrins: a structural platform for stabilization and activation of membrane channels, receptors and transporters," *Biochimica et Biophysica Acta (BBA) - Biomembranes*, vol. 1838, no. 2, pp. 620–634, 2014.
- [34] I. Solar, J. Dulitzky, and N. Shalkai, "Hemin-promoted peroxidation of red cell cytoskeletal proteins," *Archives of Biochemistry and Biophysics*, vol. 283, no. 1, pp. 81–89, 1990.
- [35] W. T. Tse, M. C. Lecomte, F. F. Costa et al., "Point mutation in the beta-spectrin gene associated with alpha I/74 hereditary elliptocytosis. Implications for the mechanism of spectrin dimer self-association," *The Journal of Clinical Investigation*, vol. 86, no. 3, pp. 909–916, 1990.
- [36] V. Bennett and A. J. Baines, "Spectrin and ankyrin-based pathways: metazoan inventions for integrating cells into tissues," *Physiological Reviews*, vol. 81, no. 3, pp. 1353–1392, 2001.
- [37] A. P. Kozlov, E. A. Krasavin, A. V. Boreyko, A. P. Chernyaev, P. Y. Alekseeva, and U. A. Bliznyuk, "Investigation of erythrocyte membrane damage under the action of γ radiation in a wide dose range using electroporation," *Physics of Particles and Nuclei Letters*, vol. 5, no. 2, pp. 127–130, 2008.
- [38] D. S. Gokhin, R. B. Nowak, J. A. Khoory, A. d. I. Piedra, I. C. Ghiran, and V. M. Fowler, "Dynamic actin filaments control the mechanical behavior of the human red blood cell membrane," *Molecular Biology of the Cell*, vol. 26, no. 9, pp. 1699–1710, 2015.
- [39] S. E. Lux, "Anatomy of the red cell membrane skeleton: unanswered questions," *Blood*, vol. 127, no. 2, pp. 187–199, 2016.

Research Article

Effect of Fe₃O₄ Nanoparticles on Mixed POPC/DPPC Monolayers at Air-Water Interface

Zhuangwei Xu, Changchun Hao , Bin Xie, and Runguang Sun

School of Physics and Information Technology, Shaanxi Normal University, Xi'an 710062, China

Correspondence should be addressed to Changchun Hao; haochangchun@snnu.edu.cn

Received 1 November 2018; Revised 20 December 2018; Accepted 8 January 2019; Published 3 March 2019

Guest Editor: Andreas Stylianou

Copyright © 2019 Zhuangwei Xu et al. This is an open access article distributed under the Creative Commons Attribution License, which permits unrestricted use, distribution, and reproduction in any medium, provided the original work is properly cited.

Fe₃O₄ nanoparticles (NPs) as a commonly used carrier in targeted drug delivery are widely used to carry drugs for the treatment of diseases. However, the mechanism of action of between Fe₃O₄ NPs and biological membranes is still unclear. Therefore, this article reports the influence of hydrophilic and hydrophobic Fe₃O₄ NPs on mixed 1-palmitoyl-2-oleoyl-*sn*-glycero-3-phosphocholine (POPC) and 1,2-dipalmitoyl-*sn*-glycero-3-phosphocholine (DPPC) that were studied using the Langmuir-Blodgett (LB) film technique and an atomic force microscope (AFM). From surface pressure-area (π - A) isotherms, we have calculated the compression modulus. The results showed that hydrophobic Fe₃O₄ NPs enlarged the liquid-expanded (LE) and liquid-condensed (LC) phase of the mixed POPC/DPPC monolayers. The compressibility modulus of the mixed POPC/DPPC monolayer increases for hydrophilic Fe₃O₄ NPs, but the opposite happens for the hydrophobic Fe₃O₄ NPs. The adsorption of hydrophobic Fe₃O₄ NPs in mixed POPC/DPPC monolayers was much more than the hydrophilic Fe₃O₄ NPs. The interaction of hydrophilic Fe₃O₄ NPs with the head polar group of the mixed lipids increased the attraction force among the molecules, while the interaction of hydrophobic Fe₃O₄ NPs with the tail chain of the mixed lipids enhanced the repulsive force. The morphology of the monolayers was observed by AFM for validating the inferred results. This study is of great help for the application of Fe₃O₄ NPs in biological systems.

1. Introduction

Nowadays, nanoparticles (NPs) have been used in the research of new materials, biological imaging, biosensors, drug delivery, and other biotechnologies or biologically related systems [1–5]. Fe₃O₄ NPs, which have the characteristics of low toxicity and high biocompatibility, especially play a unique role in the study of drug delivery systems [6–9]. Based on the magnetic properties of Fe₃O₄ NPs, it can be used as a carrier to carry targeted drugs to be accurately transported to cancer cell areas. However, in order for nanoparticles to enter the cell, it is necessary to understand the interaction of the nanoparticles with the biofilm. Hence, it is urgent to study the effects of Fe₃O₄ NPs and biofilms.

A biological membrane mainly contains all kinds of lipids, cholesterol, and proteins [10, 11]. Owing to the complexity of its composition, researches have used the model of lipids to study its structural characteristics. In the past years, people mainly studied the effects of Fe₃O₄

on the single lipid layer [1]. There were few researches who committed to Fe₃O₄ NPs and multilipids, especially to compare the different properties of Fe₃O₄ NPs with those of biofilm models. Therefore, it is necessary to study the effects of hydrophilic and hydrophobic Fe₃O₄ NPs on mixed lipid monolayers.

The Langmuir-Blodgett (LB) method is one of the most favorable tools for the *in vitro* study of the interaction at the air-water interface [12–14]. The importance of electron microscopy to modern technology is self-evident, and the atomic force microscope (AFM) is a scanning probe microscope known for its unique measurement conditions (room temperature and no vacuum) and high-resolution surface topography. AFM is widely used in many fields, such as in materials science, nanotechnology, biology, and the semiconductor industry [15]. Due to the nanoscale of the AFM tip, it can better observe the surface topography and structure of the nanoparticles and biofilm simulation. In this study, we used 1-palmitoyl-2-oleoyl-*sn*-glycero-3-phosphocholine (POPC)

and 1,2-dipalmitoyl-*sn*-glycero-3-phosphocholine (DPPC) lipids as binary biological membrane models to explore the interaction of hydrophilic and hydrophobic Fe_3O_4 NPs with biological membrane models. We use LB and AFM techniques to study the stability, fluidity, and adsorption of monolayers.

2. Materials and Methods

2.1. Materials. 1,2-Dipalmitoyl-*sn*-glycero-3-phosphocholine (DPPC) and 1-palmitoyl-2-oleoyl-*sn*-glycero-3-phosphocholine (POPC) were purchased as powders from Avanti Polar Lipids (AL, USA). Hydrophilic Fe_3O_4 NP solution (10 nm avg. part. size, 5 mg/mL in H_2O) and hydrophobic Fe_3O_4 NP solution (10 nm avg. part. size, 5 mg/mL in toluene) were purchased from Sigma-Aldrich. In these experiments, the water was the Milli-Q water (18.2 M Ω -cm) obtained from a Millipore purification system.

2.2. Methods. Monolayer experiments were carried out with Langmuir-Blodgett (LB) films (KSV Minitrough, Finland). These are made up of two barriers and a Wilhelmy plate. In the experiments, a Langmuir trough and two barriers were cleaned at least three times with anhydrous ethanol and ultrapure water alternately. The temperature of the subphase was maintained at $22 \pm 0.5^\circ\text{C}$ by circulating water equipment. The exact volume of the lipid solution was added to the air-water interface by a Hamilton microsyringe [16].

The surface pressure-area (π - A) isotherm curve of the monolayer can be autoobtained by computer. In order to increase the reliability of the experimental data, the experimental data were repeatedly computed at least three times. The monolayer was deposited onto freshly cleaved mica at the surface pressures of 5 mN/m and 20 mN/m by a pulling device with a speed of 1 mm/min. The transfer ratio is close to a unit, indicating that mica is almost completely covered with single layer.

The microstructures of LB monolayers were observed using the SPM-9500-J3 atomic force microscope (AFM) (Shimadzu Corp., Japan) in tapping mode at room temperature. The AFM images of the maximum scanning area of $125 \times 125 \mu\text{m}$ and a Z range of about $8 \mu\text{m}$ was collected using a micro-V-shaped cantilever probe (Olympus Optical Co. Ltd., Japan). The probe was made of Si_3N_4 with a spring constant of 0.06 N/m and a tip radius of 10 nm. The images were collected simultaneously with 512×512 points and a scanning rate of 1.0 Hz per line.

3. Results and Discussion

3.1. π - A Isotherms and C_s^{-1} of Monolayers with Hydrophilic and Hydrophobic Fe_3O_4 NPs. The surface pressure-area (π - A) isotherms can be used to reflect the phase behavior and thermodynamic properties of the lipid monolayers. The π - A isotherms of POPC/DPPC monolayers with different molar ratios at the air-water interface are shown in Figure 1(a). For a pure DPPC monolayer, the coexistence region of the liquid-expanded and liquid-condensed (LE-LC) phase was observed at the surface pressure of 4.5 mN/m, which is consistent with literature [17]. When $X_{\text{POPC}} = 0.25$, the phase

transition point of the LE-LC phase was still observed. However, when X_{POPC} was increased to 0.5 and 0.75, the plateau-like LE-LC phase disappeared. The phase transition temperatures of DPPC and POPC are 41°C and -2°C , respectively [18]. At room temperature, the DPPC phase is in the gel phase and the POPC phase is in the liquid phase. The mixture of POPC/DPPC showed a different phase behavior from pure lipids.

Figures 1(b) and 1(c) show the π - A isotherms of mixed POPC/DPPC monolayers with the different subphase, respectively. In the subphase, the concentration of hydrophilic and hydrophobic Fe_3O_4 NPs was 0.016 mM, which was consistent in all experiments. We found that the isotherms moved to the direction of a larger area for the hydrophobic Fe_3O_4 NP case than for the hydrophilic Fe_3O_4 NP case.

In order to more easily understand the effect of hydrophilic/hydrophobic Fe_3O_4 NPs on the isotherms of the lipid monolayers, the relevant information is summarized in Figure 2. The lipid monolayers have three characteristic parameters: limiting area A_∞ (an empirical parameter approximating the area occupied by the molecules at zero pressure), collapse pressure π_c , and lift-off area A_L (the molecular occupation area where the isotherm rising just emerges related to the baseline) [19].

The limiting area of pure DPPC monolayers is only 38.8 \AA , while the limiting area of pure POPC is 65.76 \AA . After the hydrophilic/hydrophobic Fe_3O_4 NPs are added to the subphase, the limiting area of the monolayers increases and the hydrophobic Fe_3O_4 NPs are larger than the hydrophilic Fe_3O_4 NPs. The collapse pressure decreases with the increase of X_{POPC} . In the presence of POPC molecules, hydrophobic Fe_3O_4 NPs significantly affect the collapse pressure of the monolayers, resulting in a significant dropping of the collapse pressure. Compared with pure DPPC monolayers, the lift-off area of DPPC monolayers is higher in the presence of hydrophilic Fe_3O_4 NPs, but lower in comparison with hydrophobic Fe_3O_4 NPs.

The compression modulus C_s^{-1} can be calculated from the π - A isotherms [20, 21] to study the compression or elastic properties of the Langmuir monolayers. It is calculated as follows:

$$C_s^{-1} = -A \left(\frac{\partial \pi}{\partial A} \right)_T, \quad (1)$$

where A and π are the mean molecular area and surface pressure, respectively.

The maximum value of compression modulus $C_{s \text{ max}}^{-1}$ indicates the rigid state of Langmuir monolayers. Figure 3 represents the compression modulus versus area (C_s^{-1} vs. A) of certain molar ratios of mixed POPC/DPPC (pure POPC black, DPPC olive, $X = 0.75$ red, $X = 0.5$ blue, $X = 0.25$ magenta) at the air-water interface.

For convenience, the maximum value of compression modulus $C_{s \text{ max}}^{-1}$ is shown in Figure 4. In Figure 4, the $C_{s \text{ max}}^{-1}$ values of pure DPPC and POPC monolayers are 202.89 mN/m and 86.78 mN/m, respectively, indicating that

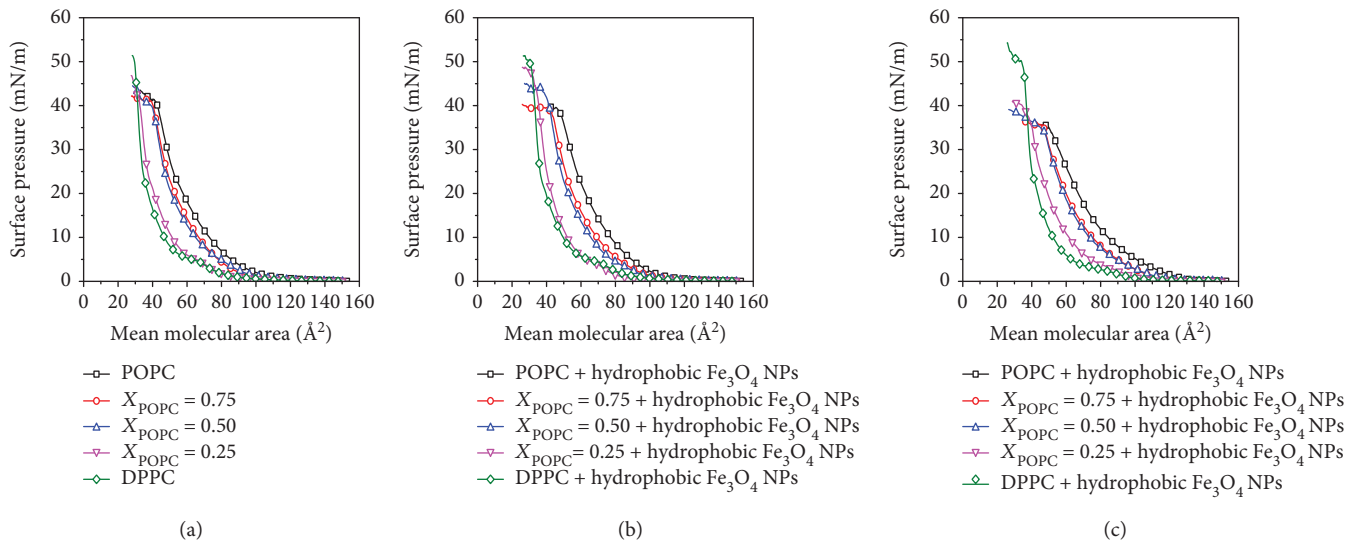


FIGURE 1: The surface pressure-area (π - A) isotherms of a mixed POPC/DPPC monolayer. (a) Pure lipids; (b) hydrophilic Fe₃O₄ NPs; (c) hydrophobic Fe₃O₄ NPs.

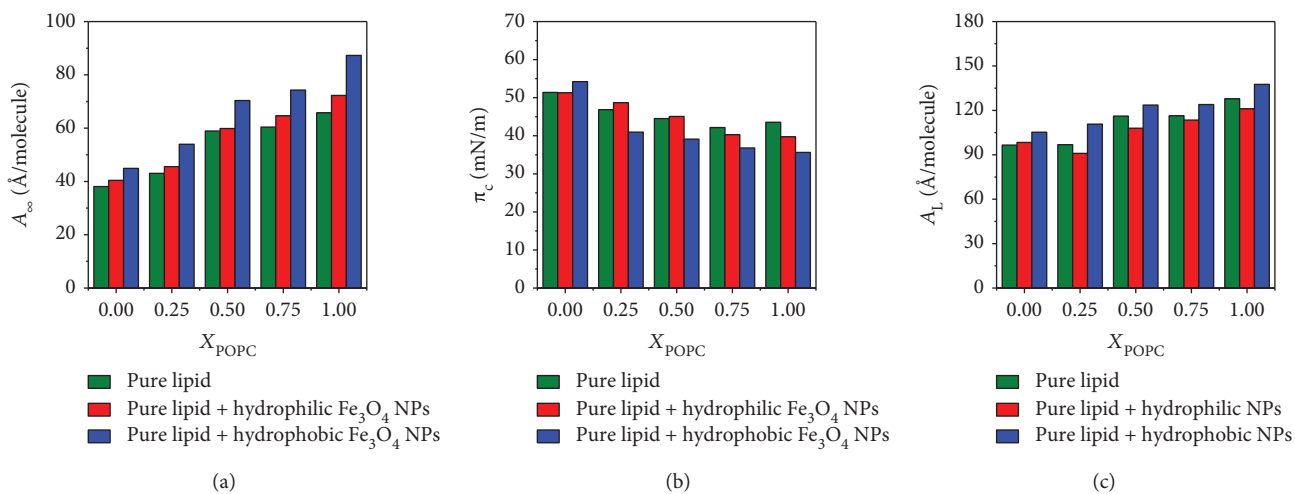


FIGURE 2: (a) Limiting area A_{∞} . (b) Collapse pressure π_c . (c) Lift-off area A_L of mixed POPC/DPPC monolayers with different subphases.

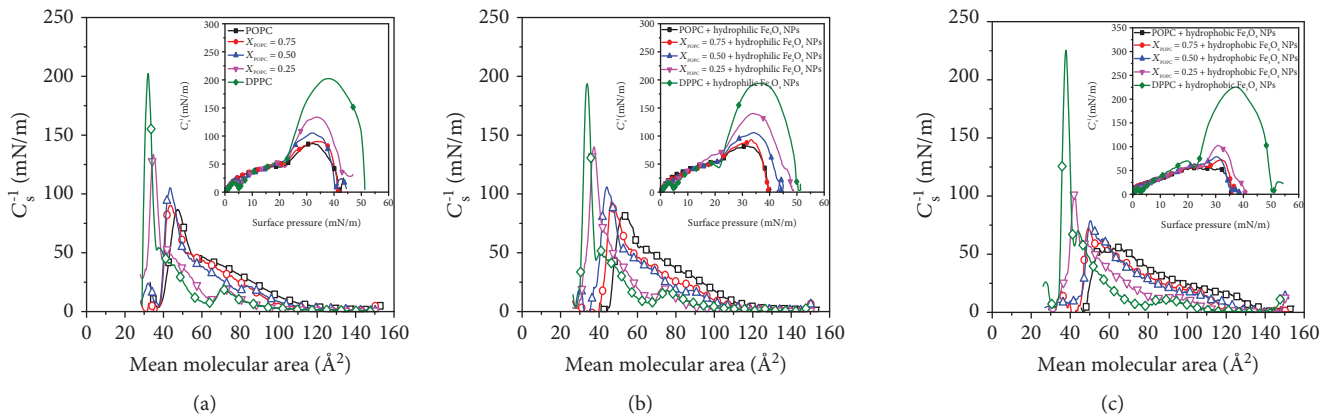


FIGURE 3: The compression modulus versus area (C_s^{-1} vs. A) of mixed POPC/DPPC (pure POPC black, DPPC olive, $X_{\text{POPC}} = 0.75$ red, $X_{\text{POPC}} = 0.5$ blue, and $X_{\text{POPC}} = 0.25$ magenta) with different subphases. (a) Water; (b) hydrophilic Fe₃O₄ NPs; (c) hydrophobic Fe₃O₄ NPs. Inset: plot of C_s^{-1} vs. π dependencies.

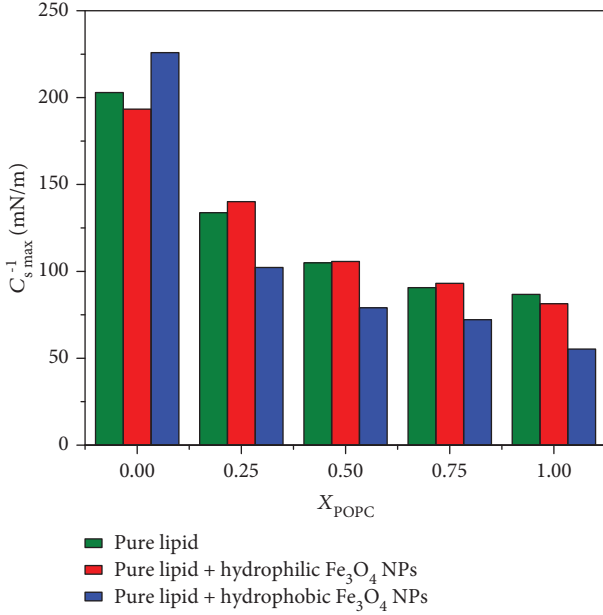


FIGURE 4: Compression modulus $C_{s, \max}^{-1}$ of mixed POPC/DPPC monolayers with different subphases.

they are in the liquid-gel phase and the liquid phase, respectively. As the proportion of POPC increases, the $C_{s, \max}^{-1}$ values of the mixed POPC/DPPC monolayers decrease, indicating that the phase transitions of mixed lipids are in the coexistence of the gel phase (DPPC) and liquid phase (POPC). The presence of POPC obviously enhances the fluidity of Langmuir monolayers. The compressive modulus of DPPC decreased slightly when hydrophilic Fe_3O_4 NPs were added into the subphase. However, the addition of hydrophobic Fe_3O_4 NPs can increase the rigidity of the DPPC monolayer.

3.2. The π - t Adsorption Curve of Mixed POPC/DPPC Monolayers. In our experiments, to understand the adsorption or permeability of exogenous substances such as drugs or nanoparticles to the cell membrane, the change of adsorption capacity is usually explained by the change of surface pressure over time [1, 22]. Figure 5 shows the surface pressure-time (π - t) adsorption curve of different molar ratios of mixed POPC/DPPC at the initial pressure of 5 mN/m and 20 mN/m. Figure 5(a) shows the change of surface pressure of the DPPC and POPC monolayers at an initial surface pressure of 5 mN/m. The surface pressure of the DPPC monolayer gradually decreases with increasing time. The surface pressure of the mixed lipid monolayers increases slightly as the proportion of POPC increases. We found that the adsorption curves of the mixed POPC/DPPC with hydrophilic/hydrophobic Fe_3O_4 NPs were different from the pure lipids (Figures 5(b) and 5(c)). The surface pressure of mixed lipids in the presence of hydrophilic Fe_3O_4 NPs is higher than that of pure lipids, while the surface pressure of mixed lipids with hydrophobic Fe_3O_4 NPs is significantly lower than that of pure lipids. The change in the adsorption curves of both pure and mixed POPC/DPPC at an initial surface pressure

of 20 mN/m is similar to the change in initial surface pressure of 5 mN/m, but the former is more varied than the latter. It is found from Figures 5(d) and 5(f) that the effect of hydrophilic and hydrophobic Fe_3O_4 NPs on the adsorption curve of mixed lipid monolayers is more notable at high surface pressure (20 mN/m).

At the initial surface pressure of 5 mN/m, the $\Delta\pi$ (surface pressure difference from 0 to 100 minutes) increases with the increases of X_{POPC} . However, at the initial surface pressure of 20 mN/m, the $\Delta\pi$ decreases with the increase of X_{POPC} . This may be due to the unsaturated tail chain of POPC molecules, which increases the fluidity of the monolayer and makes it easier for it to adsorb to the interface. It is also observed that hydrophobic Fe_3O_4 NPs have a greater influence on the interfacial adsorption capacity than hydrophilic Fe_3O_4 NPs. Due to the hydrophobic nature of nanoparticles, part of the lipid molecules are extruded from the interface or form NP-lipid complexes into the subphase. At the initial surface pressure of 20 mN/m, hydrophobic Fe_3O_4 NPs have a significant effect on the adsorption of lipid monolayers. The surface pressure of the adsorption curve have larger increases with the increase of X_{POPC} , compared with that of DPPC monolayers. The change of high surface pressure is much more than that of low surface pressure. Because of the tight intermolecular arrangement of lipid monolayers at high surface pressures, the electrostatic repulsion of lipid tail chains is enhanced.

3.3. The Thermodynamic Analysis of Mixed POPC/DPPC Monolayers. For the miscibility and stability of mixed lipid monolayers, we can clarify their thermodynamic properties with the excess mean molecular area (A_{exc}) and excess Gibbs free energy (ΔG_{ex}). For binary mixtures, we give the surface pressure π , ideal area per molecule A_{ideal} , excess mean molecular area A_{exc} , and excess Gibbs free energy ΔG_{ex} [16, 23, 24]; they are defined as follows:

$$\begin{aligned}
 A_{\text{ideal}}(\text{POPC/DPPC}) &= X_{\text{POPC}}A_{\text{POPC}} + X_{\text{DPPC}}A_{\text{DPPC}}, \\
 A_{\text{exc}}(\text{POPC/DPPC}) &= A_{12} - A_{\text{ideal}}(\text{POPC/DPPC}), \\
 \Delta G_{\text{ex}} &= N_A \int_0^\pi A_{\text{exc}} d\pi,
 \end{aligned} \tag{2}$$

where A_{POPC} and A_{DPPC} are the areas per molecule of POPC and DPPC in pure monolayers at the considered π , and X_{POPC} and X_{DPPC} are the molar fractions of POPC and DPPC in the binary mixtures, respectively; A_{12} is the experimental evaluation of the area per molecule of the binary mixtures, π is surface pressure, and N_A is the Avogadro number.

The A_{exc} values of the mixed lipids in the case of ideal miscibility or complete immiscibility is zero [25]. According to previous reports, $A_{\text{exc}} > 0$ indicates that the lipid molecules are repulsive interactions, and $A_{\text{exc}} < 0$ indicates that the lipid molecules are attractive interactions [26]. Figure 6 shows the excess mean molecular area and excess Gibbs free energy of lipid monolayers. A negative value of A_{exc} ($X_{\text{POPC}} = 0.25$) indicates that there is an attractive interaction. A positive value of A_{exc} ($X_{\text{POPC}} = 0.5$) indicates that the equimolar

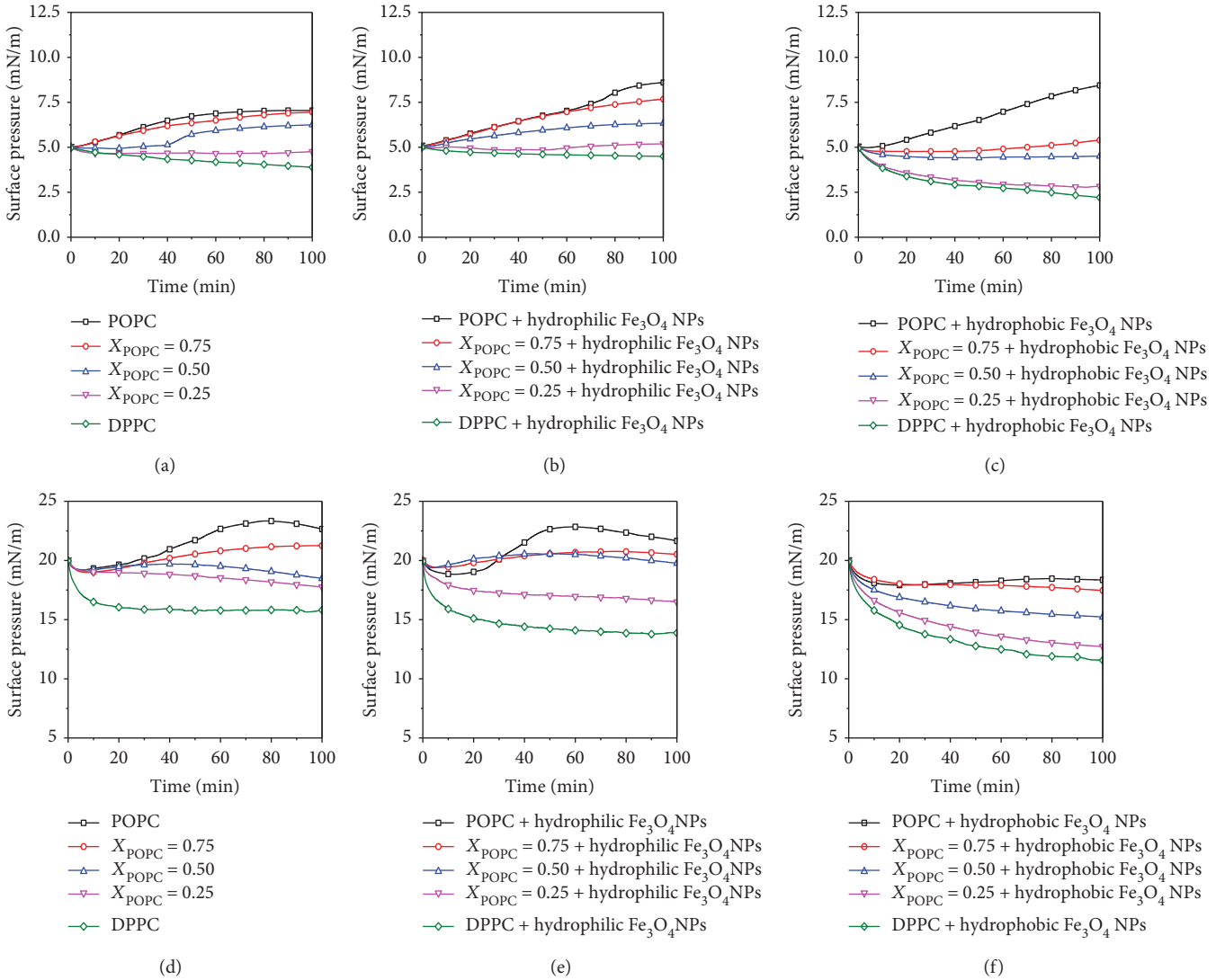


FIGURE 5: Surface pressure-time (π - t) adsorption curve of different molar ratios of mixed POPC/DPPC at the initial surface pressure of 5 mN/m and 20 mN/m. (a and d) Lipid, (b and e) hydrophilic Fe_3O_4 NPs, and (c and f) hydrophobic Fe_3O_4 NPs.

POPC and DPPC have a repulsive interaction. In the experiments, hydrophilic Fe_3O_4 NPs enhanced the attraction interaction of mixed POPC/DPPC ($X_{\text{POPC}} = 0.25$) monolayers. The content of POPC molecules in the monolayers was further increased, and the molecular interaction in the mixed monolayers were transformed from repulsive to attractive interactions (Figure 6(b)). This is because the interaction between hydrophilic Fe_3O_4 NPs and the polar head of mixed lipids weakens the interaction of lipid molecules. In the presence of hydrophobic Fe_3O_4 NPs (Figure 6(c)), the value of A_{exc} ($X_{\text{POPC}} = 0.25$) decreases to the negative value as the surface pressure increases, indicating that the interaction between the force changes from repulsive force to attractive force. At $X_{\text{POPC}} = 0.5$ and $X_{\text{POPC}} = 0.75$, the values of A_{exc} are positive and negative, respectively. In contrast to hydrophilic Fe_3O_4 NPs, the repulsion interaction between lipid molecules is enhanced or the attraction interaction is attenuated in the presence of hydrophobic Fe_3O_4 NPs. In

Figure 6(d), the value of ΔG_{ex} has a minimum at $X_{\text{POPC}} = 0.25$, indicating that the monolayers are most stable at POPC:DPPC (1:3), and the case of hydrophilic Fe_3O_4 NPs is similar to this condition. However, for the hydrophobic Fe_3O_4 NP subphase, the most stable lipid monolayers are POPC:DPPC (3:1).

3.4. The AFM Images of Pure POPC and DPPC and Different Molar Ratios of Mixed POPC/DPPC Monolayers with Hydrophilic and Hydrophobic Fe_3O_4 NPs at the Air-Water Interface. The AFM images of mixed POPC/DPPC monolayers at the initial pressures of 5 mN/m and 20 mN/m are shown in Figures 7 and 8, respectively.

In Figure 7(a), the pure DPPC monolayers at an initial surface pressure of 5 mN/m were in the LE-LC phase, and a polygonal irregular sheet-like structure was observed in the AFM image. With the increase of X_{POPC} , it can be observed that the DPPC domains are gradually reduced

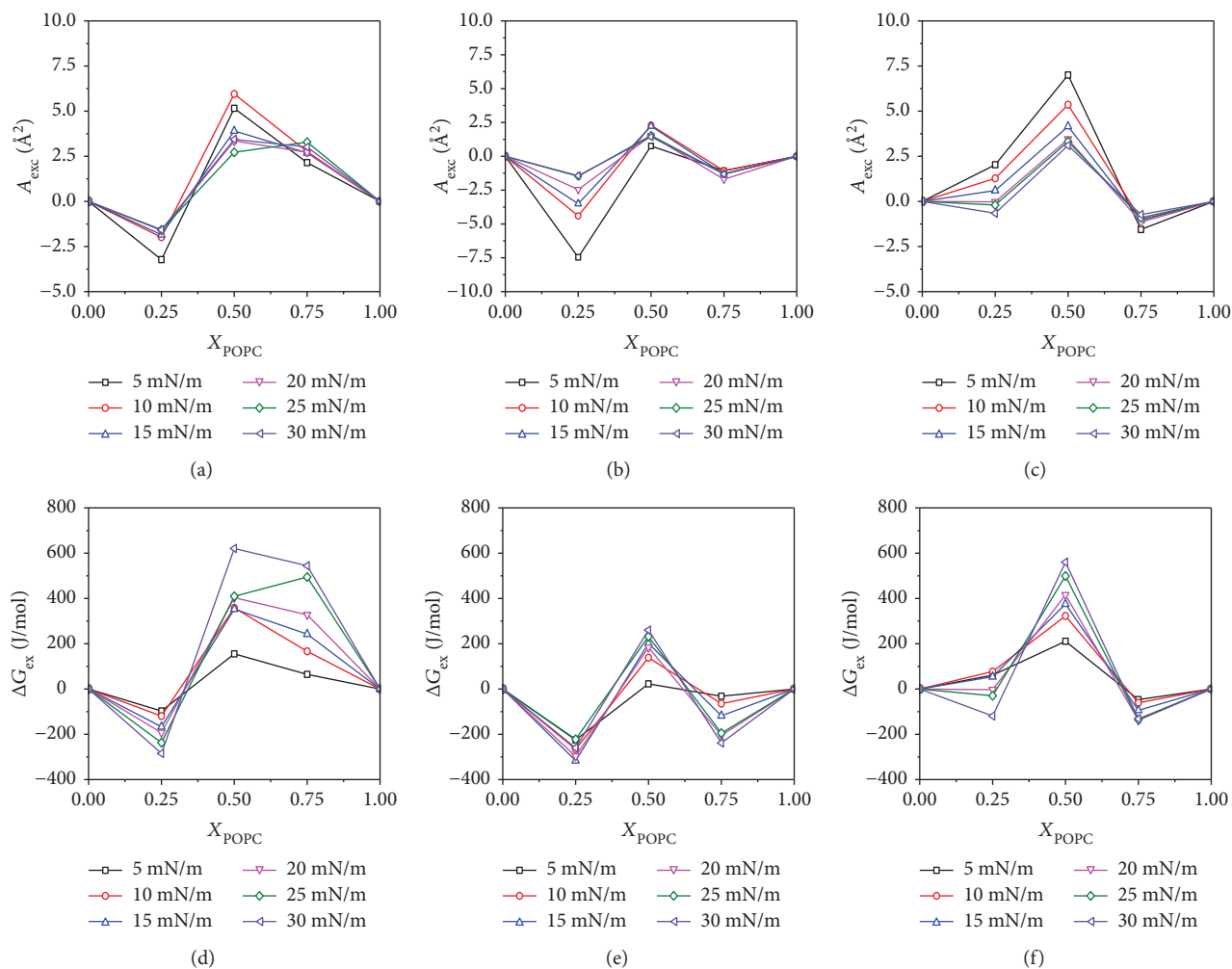


FIGURE 6: Excess mean molecular area (A_{exc}) and excess Gibbs free energy (ΔG_{exc}). (a and d) Lipid, (b and e) hydrophilic Fe_3O_4 NPs, and (c and f) hydrophobic Fe_3O_4 NPs.

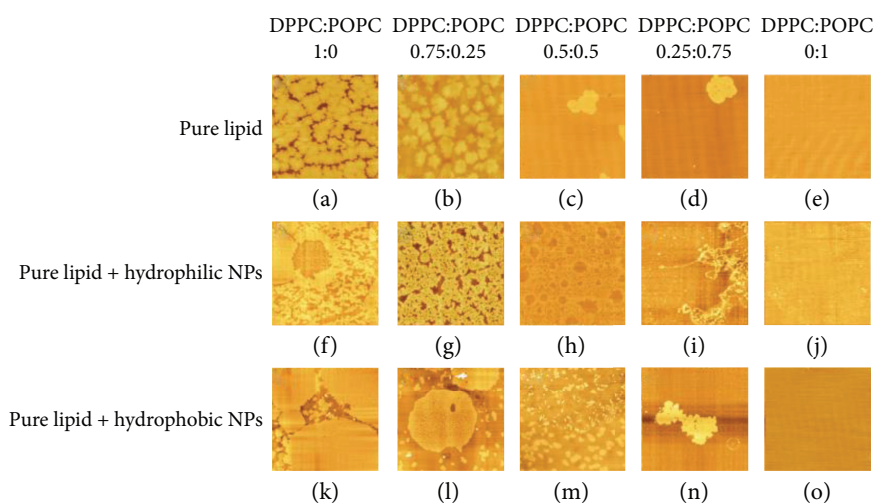


FIGURE 7: AFM images of mixed POPC/DPPC at the initial pressure of 5 mN/m.

and the POPC liquid phase appears. The AFM pattern of the DPPC monolayers with hydrophilic Fe_3O_4 NPs shows a partially dispersed platelet-like structure. The mixed

POPC/DPPC ($X_{POPC} = 0.25$) monolayers with hydrophilic Fe_3O_4 NPs showed a porous, irregular sheet-like structure, which was more compact than pure $X_{POPC} = 0.25$. Due to

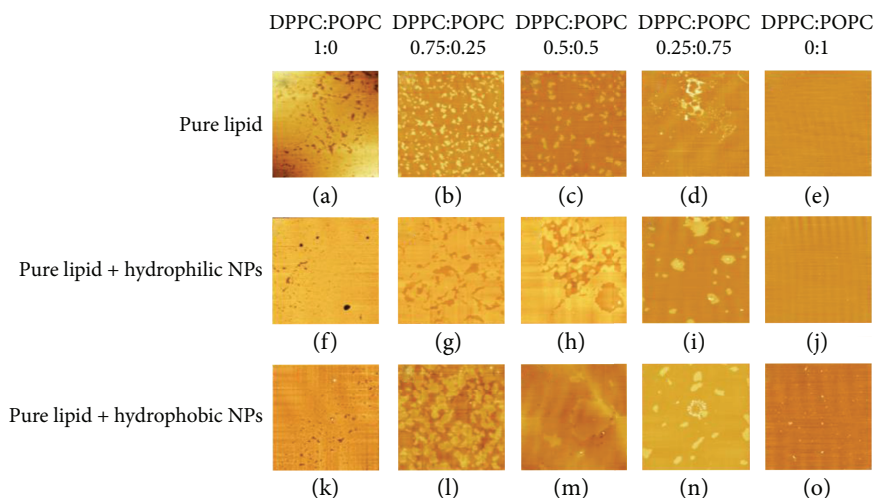


FIGURE 8: The AFM images of mixed POPC/DPPC monolayers at the initial pressure of 20 mN/m.

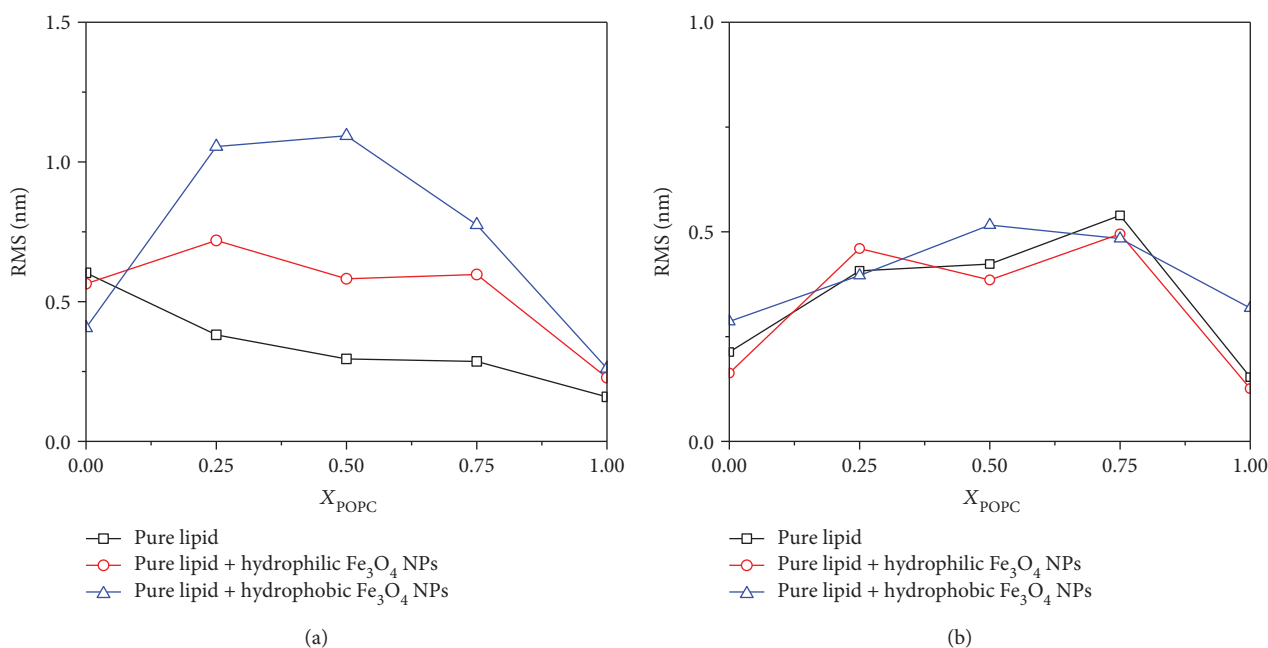


FIGURE 9: Surface roughness for the AFM images of mixed POPC/DPPC monolayers at the initial pressures of (a) 5 mN/m and (b) 20 mN/m.

the interaction between the hydrophilic Fe_3O_4 NPs and the head of the DPPC molecules, the DPPC molecules or NP-DPPC complexes enter the subphase, which affects the DPPC monolayers in the interface arrangement. For the hydrophobic Fe_3O_4 NP condition, it showed many large patches of uniform structure. With the increase of X_{POPC} , the large platform structure collapses into many small domains. This may be because of the repulsive interaction of hydrophobic Fe_3O_4 NPs with the tail chain of the mixed lipid molecules resulting in the lipid-NP complexes entering the subphase.

When the surface pressure is raised to 20 mN/m, the DPPC monolayers show a more uniform layered structure. With the increase of X_{POPC} , the monolayer forms more small-area structures. The monolayers have the phase

separation structure. At high surface pressure (20 mN/m), the lamellar structure of DPPC monolayers is more compact in the presence of hydrophilic Fe_3O_4 NPs. When the subphase is Fe_3O_4 NPs, the DPPC monolayers become more condensed. However, for the hydrophobic Fe_3O_4 NPs, the monolayer structure becomes more obvious. The interaction of hydrophilic Fe_3O_4 NPs with the lipid head enhances the attraction interaction between lipid molecules.

Figures 9(a) and 9(b) represent the surface roughness for the AFM images of mixed POPC/DPPC monolayers at the initial pressure of 5 mN/m and 20 mN/m, respectively.

In Figure 9, at an initial surface pressure of 5 mN/m, the presence of Fe_3O_4 NPs increases the surface roughness of the mixed POPC/DPPC monolayer, and the effect of hydrophobicity is stronger than that of hydrophilicity. However,

when the initial surface pressure is 20 mN/m, the effect of Fe_3O_4 NPs on the roughness of mixed POPC/DPPC is not obvious, and the variation range is only 0.15 nm. This may be due to the disordered arrangement of lipid molecules at low surface pressure. When the surface pressure increases, the order between the lipid molecules increases and leads to the dense distribution of lipid molecules, and the effect of Fe_3O_4 NPs on the roughness of the mixed POPC/DPPC monolayer is not significant.

4. Conclusion

In this paper, the influence of the subphase of mixed POPC/DPPC monolayers was studied using the LB technique. The different content has great influence on the structure of monolayers. The subphase especially contains Fe_3O_4 NPs with different properties. To further illustrate the interaction of lipids with Fe_3O_4 NPs, we used AFM to study the surface morphology between them. The results show that the repulsive interaction of hydrophobic Fe_3O_4 NPs with the tail chain of the mixed lipid molecules results in the lipid-NP complexes entering the subphase. The interaction of hydrophilic Fe_3O_4 NPs with the lipid head enhances the attraction interaction between lipid molecules. Meanwhile, Fe_3O_4 NPs can increase the roughness of the mixed POPC/DPPC monolayer at low surface pressure and the effect of hydrophobicity is stronger than that of hydrophilicity; however, the effect is not obvious under high surface pressure. This study helps us gain new insights for the interaction between nanoparticles and molecules. This could have a potential application in designing the targeted drug liposomes.

Data Availability

The data used to support the findings of this study are available from the corresponding author upon request.

Conflicts of Interest

The authors declare that they have no conflicts of interest.

Acknowledgments

This work was supported by the National Natural Science Foundation of China (No. 11874039), the Fundamental Research Funds for the Central Universities (GK2018 03021 and GK201806004), and the Experimental Technique Research Project of Shaanxi Normal University (SYJS201730).

References

- [1] C. Hao, J. Li, W. Mu et al., "Adsorption behavior of magnetite nanoparticles into the DPPC model membranes," *Applied Surface Science*, vol. 362, no. 30, pp. 121–125, 2016.
- [2] M. Liong, J. Lu, M. Kovochich et al., "Multifunctional inorganic nanoparticles for imaging, targeting, and drug delivery," *ACS Nano*, vol. 2, no. 5, pp. 889–896, 2008.
- [3] A. Roychoudhury, S. Basu, and S. K. Jha, "Dopamine biosensor based on surface functionalized nanostructured nickel oxide platform," *Biosensors and Bioelectronics*, vol. 84, pp. 72–81, 2016.
- [4] R. Sarkar, P. Pal, M. Mahato, T. Kamilya, A. Chaudhuri, and G. B. Talapatra, "On the origin of iron-oxide nanoparticle formation using phospholipid membrane template," *Colloids and Surfaces B: Biointerfaces*, vol. 79, no. 2, pp. 384–389, 2010.
- [5] D. P. Singh, C. E. Herrera, B. Singh, S. Singh, R. K. Singh, and R. Kumar, "Graphene oxide: an efficient material and recent approach for biotechnological and biomedical applications," *Materials Science and Engineering: C*, vol. 86, pp. 173–197, 2018.
- [6] M. Cao, Z. Li, J. Wang et al., "Food related applications of magnetic iron oxide nanoparticles: enzyme immobilization, protein purification, and food analysis," *Trends in Food Science & Technology*, vol. 27, no. 1, pp. 47–56, 2012.
- [7] C. Z. Ye and P. A. Ariya, "Co-adsorption of gaseous benzene, toluene, ethylbenzene, m-xylene (BTEX) and SO_2 on recyclable Fe_3O_4 nanoparticles at 0–101% relative humidities," *Journal of Environmental Sciences*, vol. 31, pp. 164–174, 2015.
- [8] L. Wu, F. Zhang, Z. Wei et al., "Magnetic delivery of Fe_3O_4 @polydopamine nanoparticle-loaded natural killer cells suggest a promising anticancer treatment," *Biomaterials Science*, vol. 6, no. 10, pp. 2714–2725, 2018.
- [9] H.-L. Liu, M. Y. Hua, H. W. Yang et al., "Magnetic resonance monitoring of focused ultrasound/magnetic nanoparticle targeting delivery of therapeutic agents to the brain," *Proceedings of the National Academy of Sciences of the United States of America*, vol. 107, no. 34, pp. 15205–15210, 2010.
- [10] D. Rose, J. Rendell, D. Lee, K. Nag, and V. Booth, "Molecular dynamics simulations of lung surfactant lipid monolayers," *Biophysical Chemistry*, vol. 138, no. 3, pp. 67–77, 2008.
- [11] A. Olżyńska, M. Zubek, M. Roeselova, J. Korchowiec, and L. Cwiklik, "Mixed DPPC/POPC monolayers: all-atom molecular dynamics simulations and Langmuir monolayer experiments," *Biochimica et Biophysica Acta (BBA) - Biomembranes*, vol. 1858, no. 12, pp. 3120–3130, 2016.
- [12] A. D. Roy, D. Dey, J. Saha, P. Debnath, D. Bhattacharjee, and S. A. Hussain, "Study of cholesterol derivative and phospholipid (DPPC) mixed film using LB technique and FRET: design of cholesterol sensor," *Sensors and Actuators B*, vol. 255, pp. 519–528, 2018.
- [13] C. Lim, S. Park, J. Park, J. Ko, D. W. Lee, and D. S. Hwang, "Probing nanomechanical interaction at the interface between biological membrane and potentially toxic chemical," *Journal of Hazardous Materials*, vol. 353, no. 5, pp. 271–279, 2018.
- [14] M. Kawaguchi, "Interfacial characteristics of binary polymer blend films spread at the air-water interface," *Advances in Colloid and Interface Science*, vol. 247, pp. 163–171, 2017.
- [15] Y. Wang, S. Wu, L. Xu, and Y. Zeng, "A new precise positioning method for piezoelectric scanner of AFM," *Ultramicroscopy*, vol. 196, pp. 67–73, 2019.
- [16] E. Guzmán, L. Liggieri, E. Santini, M. Ferrari, and F. Ravera, "Mixed DPPC-cholesterol Langmuir monolayers in presence of hydrophilic silica nanoparticles," *Colloids and Surfaces B: Biointerfaces*, vol. 105, pp. 284–293, 2013.
- [17] A. Wnętrzak, K. Łątka, and P. Dynarowicz-Łątka, "Interactions of alkylphosphocholines with model membranes—the Langmuir monolayer study," *The Journal of Membrane Biology*, vol. 246, no. 6, pp. 453–466, 2013.
- [18] K. A. Okotrub, S. Y. Amstislavsky, and N. V. Surovtsev, "Raman spectroscopy reveals the lipid phase transition in

- preimplantation mouse embryos during freezing,” *Archives of Biochemistry and Biophysics*, vol. 635, pp. 37–43, 2017.
- [19] R. Wang, Y. Guo, H. Liu, Y. Chen, Y. Shang, and H. Liu, “The effect of chitin nanoparticles on surface behavior of DPPC/DPPG Langmuir monolayers,” *Journal of Colloid and Interface Science*, vol. 519, pp. 186–193, 2018.
- [20] J. T. Davies and E. K. Rideal, *Interfacial Phenomena*, Academic Press, New York, NY, USA, 1963.
- [21] A. K. Panda, F. Possmayer, N. O. Petersen, K. Nag, and S. P. Moulik, “Physico-chemical studies on mixed oppositely charged surfactants: their uses in the preparation of surfactant ion selective membrane and monolayer behavior at the air water interface,” *Colloids and Surfaces A: Physicochemical and Engineering Aspects*, vol. 264, no. 1-3, pp. 106–113, 2005.
- [22] D. Jiang, K. L. Dinh, T. C. Ruthenburg et al., “A kinetic model for β -amyloid adsorption at the air/solution interface and its implication to the β -amyloid aggregation process,” *The Journal of Physical Chemistry B*, vol. 113, no. 10, pp. 3160–3168, 2009.
- [23] C. Hao, Q. Liu, Q. Li, J. Zhang, and R. Sun, “Thermodynamic and structural studies of DMPC and DSPC with DOTAP mixed monolayers at the air–water interface,” *Russian Journal of Physical Chemistry A*, vol. 90, no. 1, pp. 214–219, 2016.
- [24] M. Rojewska, M. Skrzypiec, and K. Prochaska, “Surface properties and morphology of mixed POSS-DPPC monolayers at the air/water interface,” *Colloids and Surfaces B: Biointerfaces*, vol. 150, pp. 334–343, 2017.
- [25] E. Guzmán, M. Ferrari, E. Santini, L. Liggieri, and F. Ravera, “Effect of silica nanoparticles on the interfacial properties of a canonical lipid mixture,” *Colloids and Surfaces B: Biointerfaces*, vol. 136, pp. 971–980, 2015.
- [26] G. Neunert, J. Makowiecki, E. Piosik, R. Hertmanowski, K. Polewski, and T. Martynski, “Miscibility of dl- α -tocopherol β -glucoside in DPPC monolayer at air/water and air/solid interfaces,” *Materials Science and Engineering C*, vol. 67, pp. 362–368, 2016.

Research Article

Nonlinear Biomechanical Characteristics of Deep Deformation of Native RBC Membranes in Normal State and under Modifier Action

Elena Kozlova ^{1,2}, Aleksandr Chernysh,^{1,2} Ekaterina Manchenko,^{1,2} Viktoria Sergunova,¹ and Viktor Moroz¹

¹Federal Research and Clinical Center of Intensive Care Medicine and Rehabilitology, V.A. Negovsky Research Institute of General Reanimatology, 107031, 25 Petrovka Str., Build. 2, Moscow, Russia

²Sechenov First Moscow State Medical University (Sechenov University), 119991, 2-4 Bolshaya Pirogovskaya st, Moscow, Russia

Correspondence should be addressed to Elena Kozlova; waterlake@mail.ru

Received 4 July 2018; Accepted 5 September 2018; Published 19 November 2018

Guest Editor: Andreas Stylianou

Copyright © 2018 Elena Kozlova et al. This is an open access article distributed under the Creative Commons Attribution License, which permits unrestricted use, distribution, and reproduction in any medium, provided the original work is properly cited.

The ability of membranes of native human red blood cells (RBCs) to bend into the cell to a depth comparable in size with physiological deformations was evaluated. For this, the methods of atomic force microscopy and atomic force spectroscopy were used. Nonlinear patterns of deep deformation (up to 600 nm) of RBC membranes were studied in normal state and under the action of modifiers: fixator (glutaraldehyde), natural oxidant (hemin), and exogenous intoxicator (zinc ions), *in vitro*. The experimental dependences of membrane bending for control RBC (normal) were approximated by the Hertz model to a depth up to 600 nm. The glutaraldehyde fixator and modifiers increased the absolute value of Young's modulus of membranes and changed the experimental dependences of probe indentation into the cells. Up to some depth h_{Hz} , the force curves were approximated by the Hertz model, and for deeper indentations $h > h_{Hz}$, the degree of the polynomial function was changed, the membrane stiffness increased, and the pattern of indentation became another and did not obey the Hertz model. Quantitative characteristics of nonlinear experimental dependences were calculated for deep bending of RBC membranes by approximating them by the degree polynomial function.

1. Introduction

The mechanical properties and structural organization of membranes determine the functional state of red blood cells (RBCs). Deformability is one of the key physiological and biophysical indicators of RBC [1]. Changes of the mechanical characteristics of cell membranes can lead to a decrease in the rate of capillary blood flow and to development of stagnant phenomena in the microcirculation, and it can also reduce the amount of oxygen delivered to the tissues.

During circulation, RBCs are constantly deformed, passing through narrow capillaries [2, 3]. Elastic properties of RBC are largely determined by the stiffness of their membranes and the state of the cytoskeleton lining the inner side of the cell [4]. In studies of RBC membrane stiffness, Young's modulus is often determined at probe indentation to depths

of 10–50 nm [5]. But, since RBCs undergo significant deformations in the capillaries, it is of particular interest to study the nonlinear laws of membrane deformation into native cells to depths comparable in size with the values of their physiological deformations (0.5 μm and more).

A true estimation of the elastic properties of RBC membranes can be obtained only by measurement of native cell properties. In this case, the result will be the closest to the characteristics of a living biological object.

Measurement of the mechanical properties of membranes of native blood cells is a technically and methodically complex task. During the scanning of cells in a liquid, they can be removed by a probe. To exclude this, fixators are used: glutaraldehyde, ethanol, and osmium tetroxide [6–9]. However, fixators introduce changes in the structure of cells, which in turn can lead to a shift in the estimation of Young's

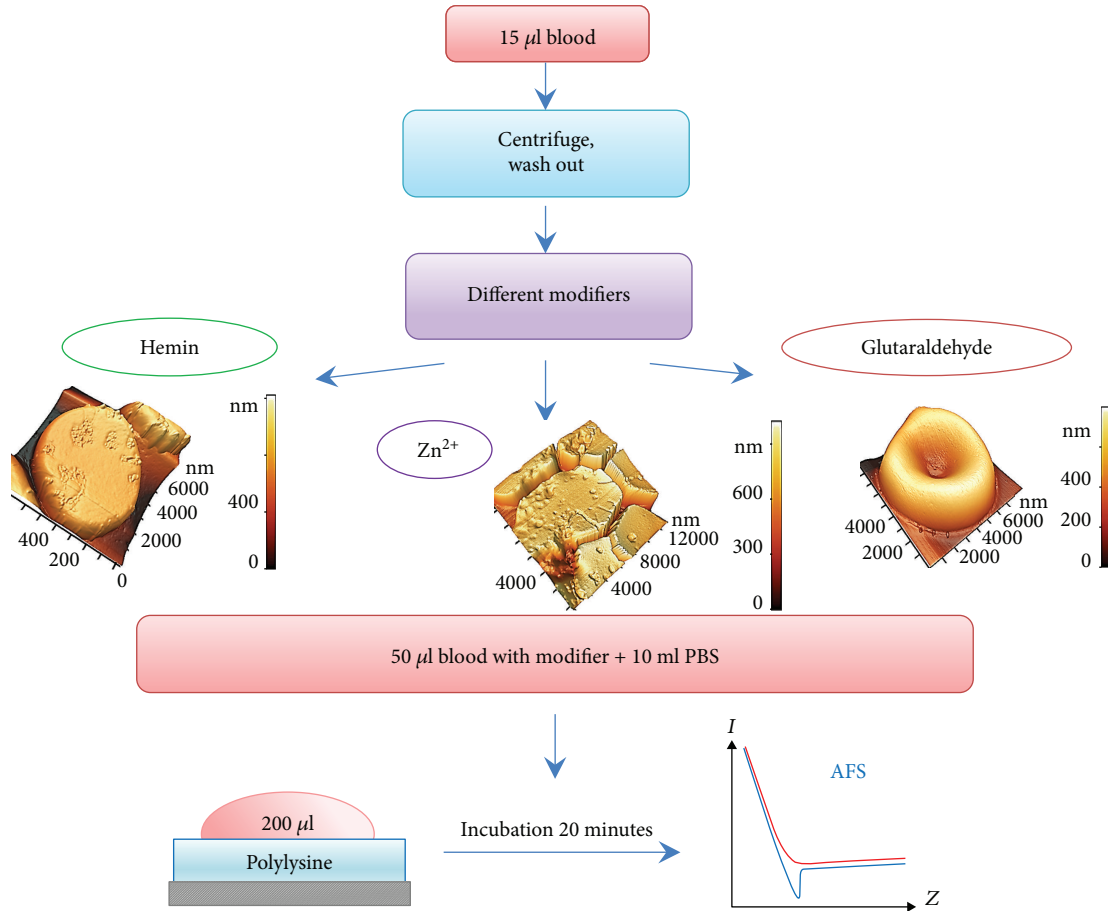


FIGURE 1: Scheme of experiments.

modulus of membranes. The stiffness of RBC membranes is also substantially dependent on the influence of oxidants, agents of intoxication, and various diseases [3, 7, 10–15]. Estimates of the absolute values of Young's modulus of RBC membranes in works that studied this problem differ dozens of times [16–19]. Therefore, the study of the ability of native RBC membranes to be bent to large depths after the action of external factors of various natures is an important biophysical and medical problem.

In this work, the stiffness of the RBC membrane was measured under physiological conditions using atomic force microscopy (AFM), *in vitro*. The main method for quantifying the mechanical characteristics of cellular surfaces is atomic force spectroscopy (AFS). Both visualization (AFM) and measurement of cell membrane stiffness (AFS) are realized on one set of equipment and allow obtaining results with the highest resolution available in modern studies [5].

The aim is to study nonlinear mechanical characteristics of deep deformation of native RBC membranes in normal state and under the action of modifiers, *in vitro*.

2. Materials and Methods

2.1. The Scheme of Experiments. Experiments *in vitro* were carried out according to the scheme shown in Figure 1. In the first stage of the experiment, a suspension of erythrocytes

was prepared. For this, 150 µl of fresh human blood was centrifuged at 3000 rpm during 5 minutes to separate blood cells from plasma. Plasma was removed, and the volume was brought to that of the original blood sample with PBS, pH 7.4 (PBS Tablets, MP Biomedicals, USA). Hence, in suspension, RBC concentration was the same as in initial blood. The RBCs were washed three times in PBS. In the second stage of the experiment, various modifiers were added to RBCs.

2.2. RBC Suspensions. Blood sampling was carried out in microvettes with EDTA (Sarstedt AG and Co., Germany) during a prophylactic examination from 8 donors. All experiments were carried out in accordance with guidelines and regulations of the Federal Research and Clinical Center of Intensive Care Medicine and Rehabilitology, V.A. Negovsky Scientific Research Institute of General Reanimatology, Moscow, Russian Federation. All experimental protocols were approved by this Institute.

2.3. Modifiers. Studies of local stiffness of RBC membranes were carried out for the native RBCs (control) and native cells after the action of modifiers. We used such agents as glutaraldehyde (GA) (RBC membrane fixator), hemin (natural oxidant), and Zn²⁺ (heavy metal ions). Glutaraldehyde modifies complexes of actin and band 3 (crosslink of cells proteins) [8], heavy metal ions Zn²⁺ are binding to

protein structures causing their aggregation [20], and hemin can destroy spectrin, influence on band 4.1, weaken connection spectrin-band 4.1, and weaken the stability of the membrane cytoskeleton [21].

In experimental series I, dry hemin (Sigma, USA) was used to prepare the work solution. First, 200 mg of NaOH was dissolved in 10 ml of distilled water and solution A was obtained. Then 50 mg of hemin powder was dissolved in 1 ml of solution A and 5 ml of distilled water was added, and solution B was obtained. 50 μl (H50) or 80 μl (H80) of solution B were added into microvettes with blood. The incubation time was 60 minutes.

In experimental series II, 180 mg of ZnSO_4 (Sigma, USA) was dissolved in 10 ml of phosphate buffer PBS, pH 7.4, to prepare the modifier. Then, 10 μl of the resulting solution was added to 100 μl of RBCs, which was previously centrifuged at 500 rpm for 5 minutes to remove plasma. The concentration of Zn^{2+} ions in blood *in vitro* was 4 mM.

In experimental series III, 0.2% and 1% glutaraldehyde (Panreac Quimica SLU, Spain) was used as a modifier. A solution of glutaraldehyde was added into blood in a volume ratio of 1:1. These suspensions were marked correspondingly as GA 0.2% and GA1%. The cell suspension was incubated up to 4 minutes.

2.4. Preparation of RBC Samples for AFS. Cover glasses were used as the substrate for formation of RBC monolayers. The glasses were previously left in solution of polylysine at a concentration of 1 mg/ml in a Petri dish for 12 hours, then the glasses were air-dried for 2 hours. Polylysine creates positive charges over the substrate that interacts with the negative charges found over the RBC membrane [22].

The method of sedimentation was used to prepare the monolayer. To do this, 50 μl of RBC was diluted in 10 ml of phosphate buffer PBS. Then, 200 μl of erythrocyte suspension was dropped on glass with polylysine and left for 20 min for sedimentation of the cells, the drop does not dry out. The resulting sample was washed in PBS during 10 seconds and scanned by AFM. If native RBC is displaced from the substrate, the optical method of cell indication was used.

2.5. Atomic Force Microscopy. The atomic force microscope (AFM) NTEGRA Prima (NT-MDT, Russian Federation) was used to obtain cell and membrane images and to measure local stiffness of RBC membranes in a liquid. To acquire images, NSG01 cantilevers (Nanosensors, Switzerland) with a force constant of 5 N/m and tip radius of 10 nm were used. The numbers of scan points were 512 and 1024. Measurements of local stiffness of RBC membranes were performed by ASF on the vertical displacement of a piezoscanner, where the sample was placed [14, 23]. To measure the deformation of the membrane, the type SD-R150-T3L450B-10 (Nanosensors, Switzerland) cantilever was used. The radius of the cantilever probe was 150 nm, the coefficient of elasticity was 1 N/m, the probe height was 15 μm , and the resonance frequency was 21 kHz.

To measure stiffness, RBCs were scanned in an AFM field $100 \times 100 \mu\text{m}^2$; a group of cells was selected for the study and scanned in the field of $30 \times 30 \mu\text{m}^2$. Then, in the atomic force

spectroscopy mode, a marker was placed on the cell image and the region was exposed to an indenter (probe) with the force F . The characteristics and peculiarities of deep penetrations of the probe into the membrane were studied. That is, curves of the piezoscanner's approach was used in the analysis of the experimental data, $I(z)$ and correspondingly $F(h)$.

2.6. The Process of Measurements and Probes. The elasticity coefficient K of the cantilever should be comparable with the mean stiffness coefficient K_m of the cell membrane [24, 25]. If $K_m \gg K$ (glass), then a dependence between the force F and the deviation of the cantilever L is determined by Hooke's law, $F = -KL$, and the force curve is linear. In this case, $L = Z$ and indentation depth $h \rightarrow 0$. If the probe interacts with the membrane and $K_m \ll K$, then $h \rightarrow Z$, and the membrane does not exhibit elastic properties. If the probe interacts with membrane and $K_m \approx K$, then $F = -[1/K + 1/K_m(h)]^{-1}L$, and the probe bends the cell membrane to a depth of h ($h < Z$).

Based on the experimental data, the optimal value of K for measuring the local stiffness of RBC membranes is in the range of 10–50 N/m for dry cells and 0.05–1.8 N/m for native cells.

The time of probe indentation was at least 5–10 seconds in our work. Fast indentation can change the mechanical reaction of RBC membranes [19]. The aim of the study was not to investigate the change in force curves as a function of the time of penetration. Therefore, long penetration times of the indenter were chosen. The speed of indenter penetration was 0.05–1 $\mu\text{m/s}$. With such penetration rates, no effects of viscosity-related friction forces were observed.

The tip radius R should be not less than 50–80 nm. A small R (10–30 nm) leads to probe penetration into the membrane structure [1, 25]. As a result, rupture of the membrane is possible. For the registration of the K_m membrane, it is necessary for R to be larger than the size of the spectrin matrix element.

The tip height should be not less than the height of the RBC (2–10 μm).

Cantilever calibration on highly rigid material (e.g., glass) must be carried out before and after each series of measurements [14, 23]. The empirical force curve is the dependence of photodiode deflection current I on the magnitude of the vertical displacement Z of the piezoscanner, $I(Z)$. These parameters can be varied during measurements on AFM, depending on the purpose and object of the study. For our experiment, the maximum limits of piezoscanner shift were set as $Z_{\text{max}} = 2000 \text{ nm}$ and current $I_{\text{max}} = 0.3 - 0.6 \text{ nA}$.

2.7. Statistical Analysis. In the work, the following groups of RBC from donors were analyzed: control—8 donors, after exposure by GA0.2%—3 donors, GA1%—3 donors, H50—3 donors, H80—3 donors, and Zn^{2+} —2 donors. In total, 22 RBC samples were analyzed. For each sample, 50 native cells were analyzed. For them, experimental force curves were registered. Moreover, experimental dependences $F(h)$ were created. In total, the quantitative characteristics of 1100 native cells were analyzed and calculated. All standard statistical calculations of all obtained experimental results

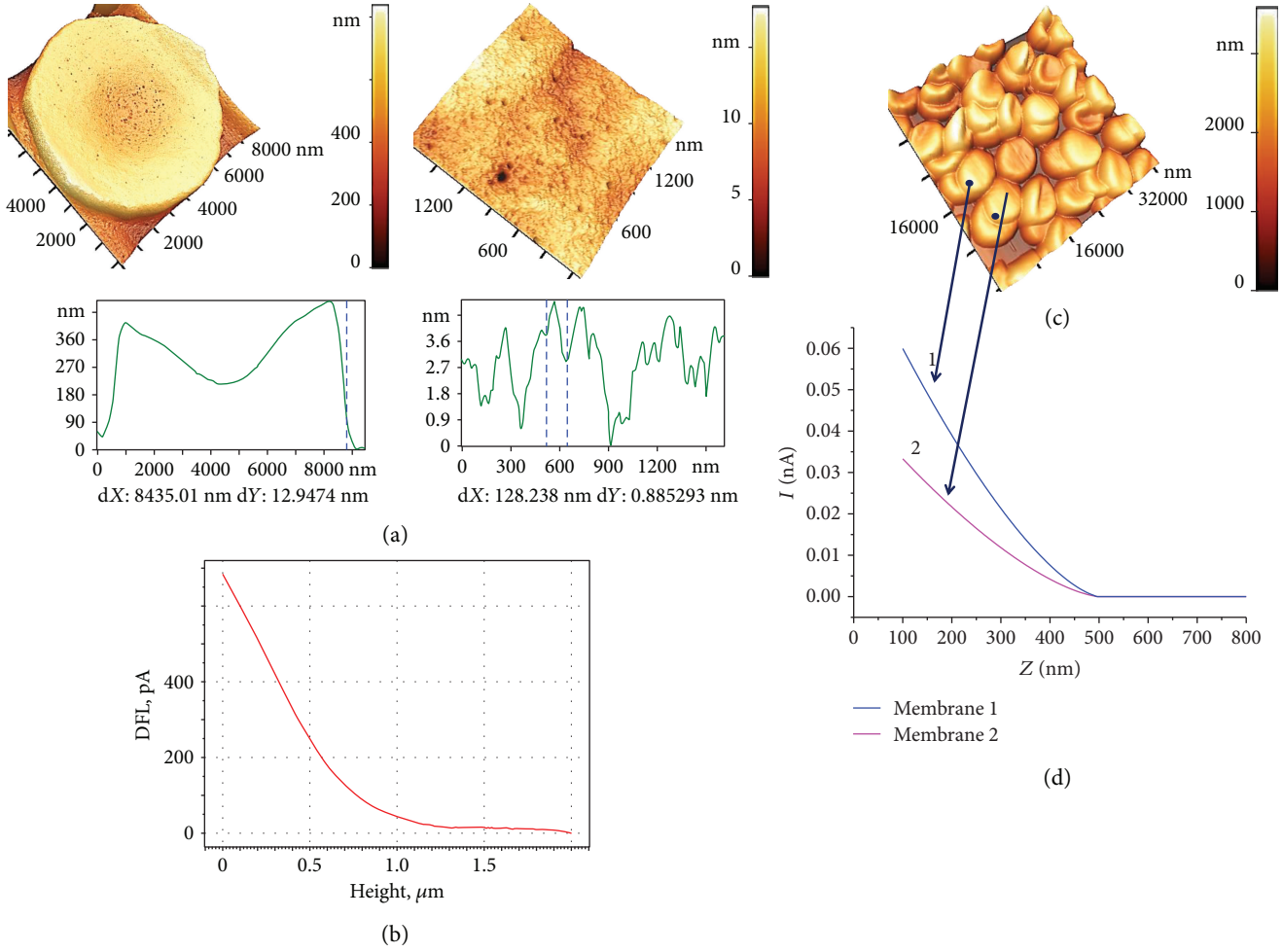


FIGURE 2: AFM images of RBC and force characteristics of the membranes. (a) 3D image of dry cells, 10 × 10 μm², of membrane fragments, and corresponding surface profiles. (b) Directly measured data $I(Z)$. (c) 3D images of native cells in a liquid medium, 50 × 50 μm². Arrows—points of application of force F from the probe. (d) Force curves $I(Z)$ after smoothing. I : the photodiode current (nA); Z : vertical displacement of the piezoscanner (nm).

and mathematical modeling were performed by Origin 9 (OriginLab, Northampton, MA). One-way ANOVA was used to determine statistical significance.

3. Results

3.1. Mechanical Characteristics of RBC Membrane Bending. Elastic properties of RBC membranes, namely, the ability of the membrane to bend into the cell under the action of the applied force, was estimated from empirical force curves. These characteristics were obtained by AFS. The local stiffness of RBC membranes was estimated by Young's modulus E (N/m²), calculated from the Hertz model [26]

$$F = \frac{4}{3}ER^{0.5}h^{1.5}, \quad (1)$$

where E is Young's modulus of the material, R is the tip radius, and h is the deformation depth (bending)

of the membrane. Such estimation is used for blood cell membranes [9, 25, 27–30].

AFS can be performed both on dry cells and on native RBC. Dry cells are easily fixed on a substrate (glass, mica, etc.), and, most importantly, they can be scanned with a thin (~10 nm) cantilever probe for analyzing their membrane nanostructure (Figures 2(a), 3(a), and 4(a)). In these cases, the resolution limit is a part of nanometers.

The method of sample preparation of native blood cells is described in Methods. It is almost impossible to record the nanostructure of native cells because of insufficient resolution of images. This is determined by the passage of the AFM laser beam through the liquid medium in which the RBCs are located. Another reason for the loss of high resolution is the use of probes with a large radius. In our works, the tip radius was 150 nm. Therefore, the image of native cells was blurred, but enough to set the points of tip probe action (Figure 2(c)).

When the piezoscanner rises, the cantilever probe acts on the application point of the RBC membrane with a given

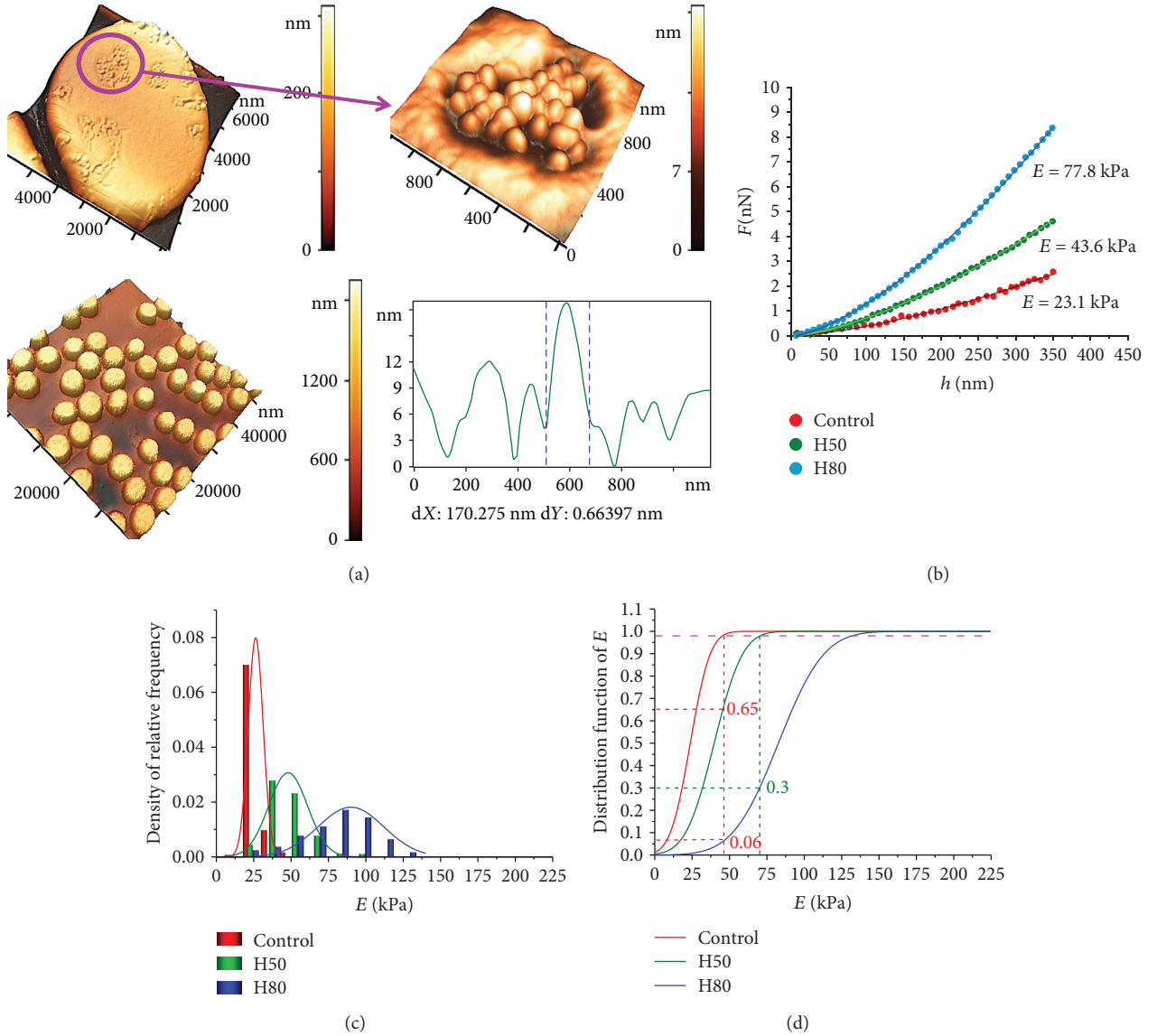


FIGURE 3: The influence of hemin on RBC membrane stiffness. (a) AFM images of RBCs, $50 \times 50 \mu\text{m}^2$, of a single cell, $10 \times 10 \mu\text{m}^2$, of a membrane defect in the form of a grain domain, and its profile. (b) Experimental curves $F(h)$ for one RBC control, for hemin H50, and for H80, and their approximation by the Hertz model. (c) Histograms of density of relative frequency of Young's modulus E for control, H50, and H80, approximated by the normal law of the Gaussian distribution. (d) Distribution function of Young's modulus E (approximation by the normal Gaussian law) for the control and after the influence of H50 and H80.

force F . As a result, the laser beam deflects, forming a photodiode electrical current I . In Figure 2(b), the primary (directly measured) data $I(Z)$ are shown.

In Figure 2(c), 3D images of native cells in a liquid medium, $50 \times 50 \mu\text{m}^2$, are shown, and arrows indicate point force F application from the probe. For two cells, force curves $I(Z)$ after smoothing by software are represented (Figure 2(d)). The intersection of the empirical curve and the level which is high than the baseline value of $0.02\Delta I$ were established as contact point Z_0 for further study. In this point, $I'(Z) > 0$. The value ΔI was set as $\Delta I = I_{\max} - I_{\text{baseline}}$.

To further analyze the probe indentation process and to calculate Young's modulus E , it is necessary to pass from

the empirical function $I(Z)$ (Figures 2(b) and 2(d)) to $F(Z)$ and $F(h)$, where F is the force acting on the sample and h is the probe (tip) indentation depth, or membrane bending. The transition from the photodiode current to the interaction force was described earlier [5].

The functions $F(Z)$ for glass and membranes of two different RBCs are shown in Figure 5(a). The difference between the Z coordinates for glass and the corresponding membrane (1 or 2) is the value of the membrane bending h into the cell due to probe action. From Figure 5(a), it follows that membrane 2 is softer than membrane 1, and therefore the bending of membrane 2 at a fixed force F is greater than the bending of membrane

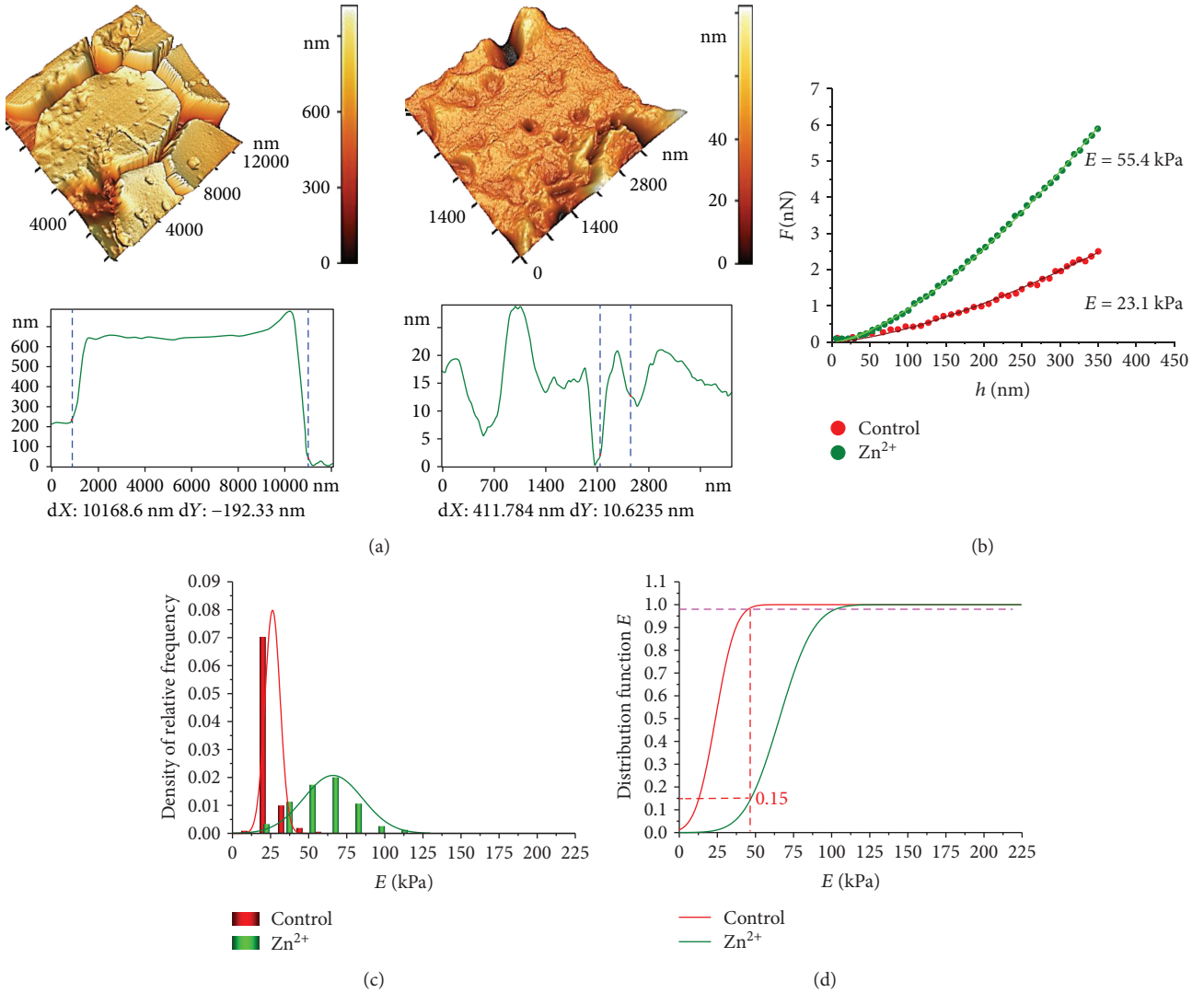


FIGURE 4: Influence of Zn²⁺ ions on RBC membrane stiffness. (a) AFM 3D images of RBC, 10 × 10 μm², of a membrane topological defect, 3 × 3 μm², and their profiles correspondingly. (b) Experimental curves $F(h)$ for membranes after control and zinc ion action. (c) Histograms of the density of relative frequency of Young's modulus E for the control and zinc ion action, approximated by the normal law of Gaussian distribution. (d) Distribution function of Young's modulus E (approximation by the normal Gaussian law) for the control and after influence of Zn²⁺.

1: $h_2 > h_1$ (Figure 5(c)). The force F determines the deviation L of the cantilever and simultaneously the deformation of the membrane itself, that is, penetration of the probe into cell to a depth h (Figure 5(a)):

$$h = Z - L. \quad (2)$$

As the probe bends the membrane into RBC, the curve $F(Z)$, for example, in Figure 5(a), can go to a straight line parallel to the glass straight line. This will mean that the process obeys Hooke's law, and the probe will stop penetrating into the cell structure, $h \rightarrow \text{const}$ and $\Delta h \rightarrow 0$.

The dependence $F(h)$ is carried out using specialized software developed by the authors. Figure 5(b) shows an example of the functions $F(h)$ for two membranes 1 and 2.

RBCs of each donor (in normal state and under different effects on blood) had initially different absolute values of the membrane modulus E . Therefore, an adequate estimation of RBC membrane stiffness of a given donor required the formation of a cell ensemble and further statistical processing. For each donor, 50 functions $F(h)$ were carried out by measurement of 50 cell force curves. For each function, Young's modulus was calculated according to 1; histograms of relative frequency density of the modulus E were plotted. The data were approximated by the Gaussian probability density function (Figures 3(c), 4(c), 5(d), and 6(c)).

3.2. *Deformation (Bending) of Normal RBC Membranes.* The results of measurements of Young's modulus E under bending of RBC membranes ($h = 600$ nm) for 8 healthy donors

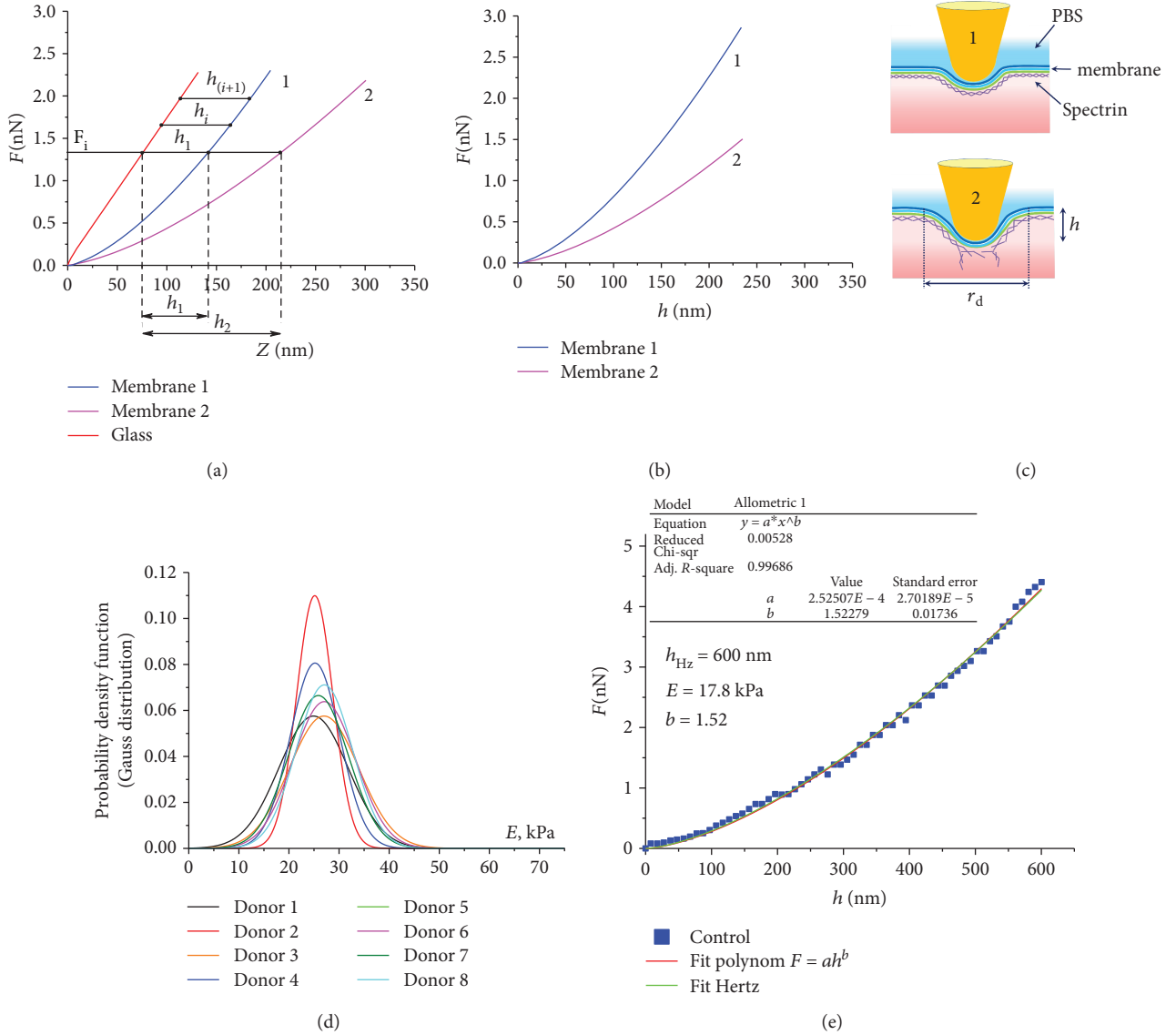


FIGURE 5: The process of RBC membrane bending under a probe action, and the construction of functions $F(h)$. (a) Experimental curves $F(Z)$ for highly stiff substance (glass), membranes of cells 1 and 2. (b) Experimental curves $F(h)$ for cell membranes 1 and 2. (c) Bending of membranes under the action of force F for stiff (1) and soft (2) membranes; F is the force acting on the membrane from the probe, Z is the vertical displacement of the piezoscanner, h is the depth of the membrane bending into RBC, PBS is the phosphate buffer solution, and r_d is the bending radius of the membrane. (d) Gaussian probability density functions of RBC membrane Young's modulus E , for 8 healthy donors. (e) The experimental curve $F(h)$ for one control (normal) RBC, its approximation by the Hertz model, and the polynomial $F = ah^b$.

(normal, or control data) are shown in Figure 5(d) according to the sample means E_m , and the standard deviations are presented in Table 1.

Approximation of the control experimental curves $F(h)$ by the Hertz model (1) was carried out. Figure 5(e) shows an example of one of these curves.

The same figure shows the approximation of the experimental graph by a polynomial of the form

$$F(h) = ah^b. \quad (3)$$

The approximation curve $F(h)_{\text{theor}}$ by the standard method of nonlinear fitting of the experimental data was

used. The status of the dependent variable was assigned to the experimental data function $F(h)_{\text{exper}}$. The degree b and coefficient a of the polynomial (3) were unknown variables. Unknown coefficients b and a are the parameters of the model, and they are chosen by the statistical program so that the theoretical curve $F(h)_{\text{theor}}$ describes the experimental data $F(h)_{\text{exper}}$ in the best way ($R^2 > 0.95$). The condition $a_i \geq 0$ must be satisfied in the approximation. The degree b and the coefficient a of the polynomial (3) were chosen by nonlinear fitting of the experimental curves (OriginLab, Northampton, MA).

Approximation by function (3) was carried out for all curves $F(h)$ (50 for each RBC sample). Depths h_{Hz} , to which

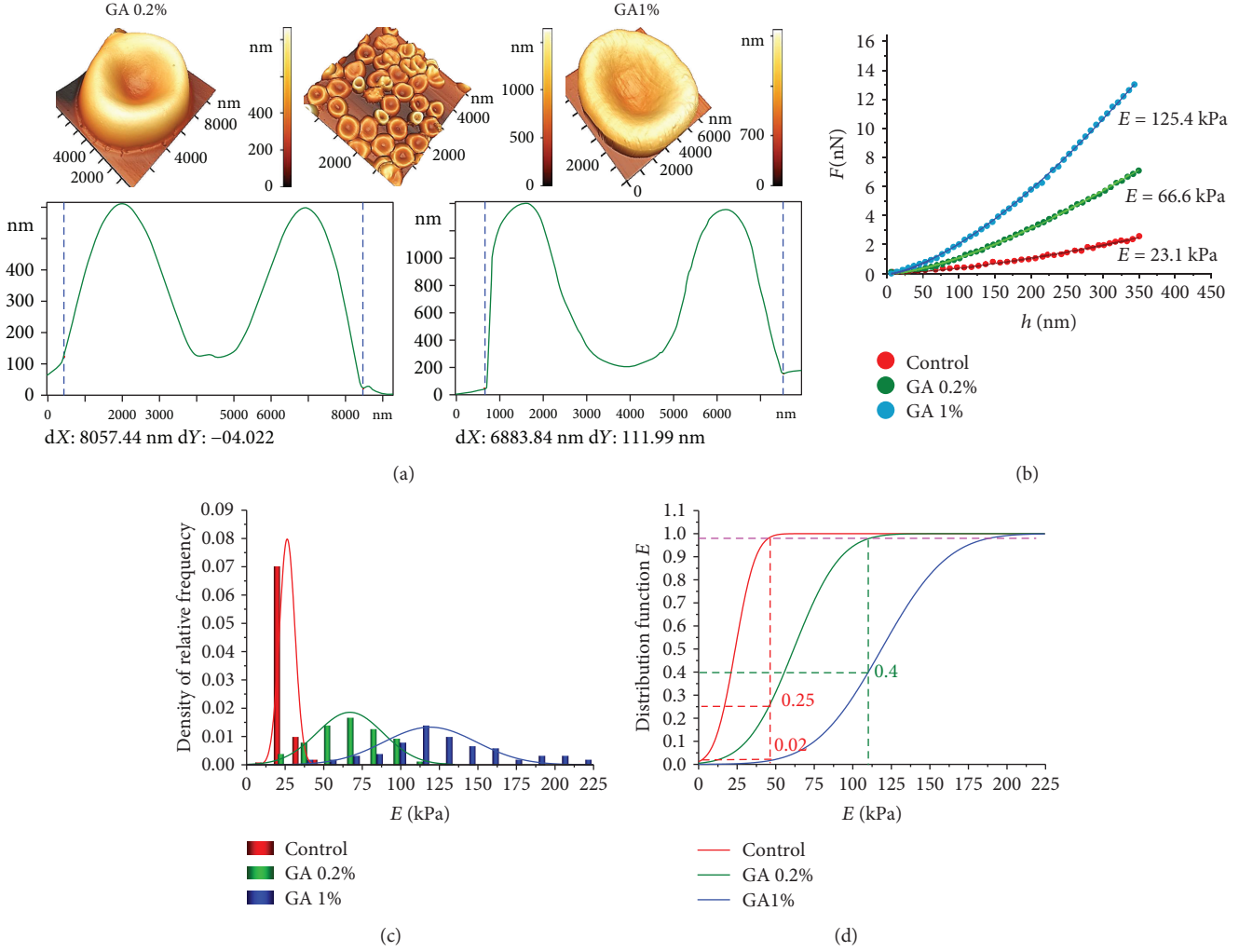


FIGURE 6: Influence of glutaraldehyde on RBC membrane stiffness. (a) AFM images of RBC, $50 \times 50 \mu\text{m}^2$ and $10 \times 10 \mu\text{m}^2$, after the action of 0.2% and 1% glutaraldehyde and their profiles, respectively. (b) Experimental curves $F(h)$ for control cell, for cell after GA0.2%, and for GA1% action, and their approximation by the Hertz model. (c) Histograms of the relative frequency density for control RBCs and under the action of GA 0.2% and GA1% on cells, approximated by the normal law of the Gaussian distribution. (d) Distribution functions of Young's modulus E (approximation by the normal Gaussian law), for control and action of GA 0.2% and GA1%, correspondingly.

TABLE 1: Young's modulus E for RBC membranes of healthy donors.

Donor	1	2	3	4	5	6	7	8
E (kN/m ²), sample mean E_m , and standard deviation	24.9 ± 6.9	25.1 ± 3.6	27 ± 6.9	25.2 ± 4.9	25.7 ± 4.3	27.1 ± 6.3	25.8 ± 6	27.1 ± 5.6

the curves $F(h)$ were adequately approximated by the Hertz model ($b = 1.50 \pm 0.02$), were calculated for each experimental curve. That is, the degree b was used as criterion for the adequacy of the Hertz model. Approximation of empirical data $F(h)$ represented in Figure 5(e) was obtained at $h = 600 \text{ nm}$: $b = 1.52$, $E_m = 17.8 \text{ kPa}$.

All the obtained control force curves $F(h)$ were adequately approximated by the function (1) and the polynomial (3) with the degree $b = 1.50 \pm 0.02$ at the level of the determination coefficient $R^2 \geq 0.95$.

3.3. *The Action of Glutaraldehyde on RBC Membranes* ($h \leq h_{Hz}$). Glutaraldehyde (GA) is used as a fixator for RBC membranes [7–9, 16]. Therefore, the work analyzes the effect of GA at concentrations 0.2% and 1% on Young's modulus of RBC membranes. The experimental data are shown in Figure 6. Figure 6(a) shows the AFM images of cells after the GA action.

With increasing GA concentration, Young's modulus E increased, and the histogram of the relative frequency density shifted towards larger values of E (Figure 6(c)). Values of E

for GA1% are statistically different from control and from GA0.2% data at $p < 0.01$.

For a detailed analysis of membrane stiffness changes under GA action in different concentrations on RBC, the distribution function $F_d(E)$ was constructed.

$$F_d(E) = \int_{-\infty}^E f(E) dE. \quad (4)$$

It was assumed that the histograms of relative frequency density (Figure 6(c)) are approximated by the normal Gaussian distribution law $f(E)$. To estimate the proportion of RBC on which the modulus E increased, the level of 0.98 was indicated on curves of functions (4). At this level, it was determined which part of the cells retained E corresponding to control data. So, after GA0.2% action, 25% of cells kept the control membrane stiffness. The membrane stiffness of 75% of cells was increased. For GA1%, the percentage of cell membrane with control E was only 2%. At the same time, for GA1%, 40% of cells have the same values E as for GA0.2%.

The experimental curves $F(h)$ (Figure 6(b)) were approximated by the Hertz model (1) and the polynomial (3) for GA0.2% and GA1%. Fifty functions $F(h)$ for each donor and for each concentration of GA were analyzed, with a total 300. The quantitative estimations of Young's modulus are shown as an example for one donor in Figure 6(b): for control $E_m = 23.1$ kPa, for GA 0.2% $E_m = 66.6$ kPa, and for GA 1% $E_m = 125.4$ kPa.

3.4. The Action of Hemin of the RBC Membrane ($h \leq h_{Hz}$). Hemin is a natural oxidant of biological structures and, in particular, an oxidizer of RBC membranes. The action of hemin H50 and H80 was studied. Figure 3(a) shows AFM 3D images of cells ($50 \times 50 \mu\text{m}^2$), of a single cell ($10 \times 10 \mu\text{m}^2$) after the hemin action. Also, there are shown images of topological nanodefects in the membrane ($1.2 \times 1.2 \mu\text{m}^2$) and their profiles. After hemin action on the blood, typical topological nanodefects in the form of domains with grain-like structures are formed in membranes [21]. Also, hemin may change simultaneously the elastic properties of RBC membranes.

An increase in the hemin concentration caused the growth of Young's modulus E (Figure 3(b)). So for H50 at the depth of $h = 300$ nm, E increased by 1.9 times in comparison with the control, and for H80 3.4 times.

Figure 3(c) shows histograms of density of the relative frequency of Young's modulus E for the control, H50, and H80, which are approximated by the normal Gaussian distribution law. The distribution of H50 and H80 is statistically different from the control and among themselves at level $p < 0.01$.

The distribution function F_d in accordance with 4 and the Hertz model (1) for control, H50, and H80 are shown in Figure 3(d). For H50, 65% of cells retained Young's modulus E the same as in the control. For H80, this fraction was 6%. For H80, in 30% of cells, modulus E was kept at the same level as after H50 action.

The experimental curves $F(h)$ for H50 and H80 action were adequately approximated by the Hertz model (1) and the polynomial (3) with $b = 1.50 \pm 0.02$, up to membrane bending to $h = 350$ nm (Figure 3(b)). Fifty functions $F(h)$ were analyzed for each donor and for each hemin concentration, with a total of 300.

3.5. The Action of Zn^{2+} Ions on RBC Membranes ($h \leq h_{Hz}$). Heavy metal ions, for example, zinc ions, cause membrane defects [20] and can increase their stiffness.

The AFM images of RBCs, membrane nanodefects, and their profiles after the action of Zn^{2+} (concentration 4 mM) are shown in Figure 4(a). Such concentration was chosen to obtain significant nanodefects in red blood cell membranes [20].

The functions $F(h)$ and the histograms of the relative frequency density approximated by Gauss's law are represented in Figures 4(b) and 4(c), correspondingly. Modulus E for control and zinc influence samples are statistically different at level $p < 0.01$.

Figure 4(d) shows the distribution functions $F_d(E)$ (4). After zinc ions' action, Young's modulus was maintained at the control level for 15% of cell membranes. The rest of the RBC membranes became stiffer by 2 times and more.

3.6. Deep Bending of RBC Membranes ($h \geq h_{Hz}$). In all studies, force F was chosen so that both in the control RBCs and under the action of the modifiers the probe was penetrated into the cell (membrane bending) to a depth $h \geq 600$ nm. Up to a certain depth h_{Hz} , the degree of the polynomial (3) was preserved at the level $b = 1.5$. After h_{Hz} , the degree may differ from 1.5. It was denoted by b_n , and the coefficient of the polynomial (3) is, respectively, a_n . All parameters of the curves $F(h)$ — E , h_{Hz} , b , b_n , a , and a_n —were calculated to the bending depth up to $h = 600$ nm.

In the control cell membrane (Figures 5(d) and 5(e)), practically all the $F(h)$ curves were approximated by the Hertz model from 0 to 600 nm at the level of the criterion $R^2 = 0.95$.

Under the modifier influence, this situation changed. On the empirical dependence of $F(h)$ at the indentation depth $h > h_{Hz}$, the degree b_n of the approximation polynomial (3) was changed. In Figures 7 and 8, three examples of empirical curves $F(h)$ are shown for the action of hemin H50, H80, glutaraldehyde GA1%, Zn^{2+} ions on the blood, and their approximation by the polynomial (3). In Table 2, the numerical parameters of these graphs are presented.

Statistical data of the values E for $h < h_{Hz}$ for control samples and for samples after action of agents are shown in Table 3. Also, there are indicated corresponding values h_{Hz} .

In a number of cases, the degree of the polynomial (3) ranged from 1.48 to 1.52. In these cases, the entire curve $F(h)$ obeyed the Hertz model. Such examples are given for H50 (Figure 7 and Table 2, no. 3), for H80 (Figure 7 and Table 2, no. 6), for GA1% (Figure 8 and Table 2, no. 9), and for Zn^{2+} (Figure 8 and Table 2, no. 12). The degree b_n of the polynomial (3) after h_{Hz} was less than 1.5 in 92% of cases and was in the range 1.01–1.45. In example no. 8 (Figure 8(a)) under the action of GA1%, $h_{Hz} = 463$ nm, and

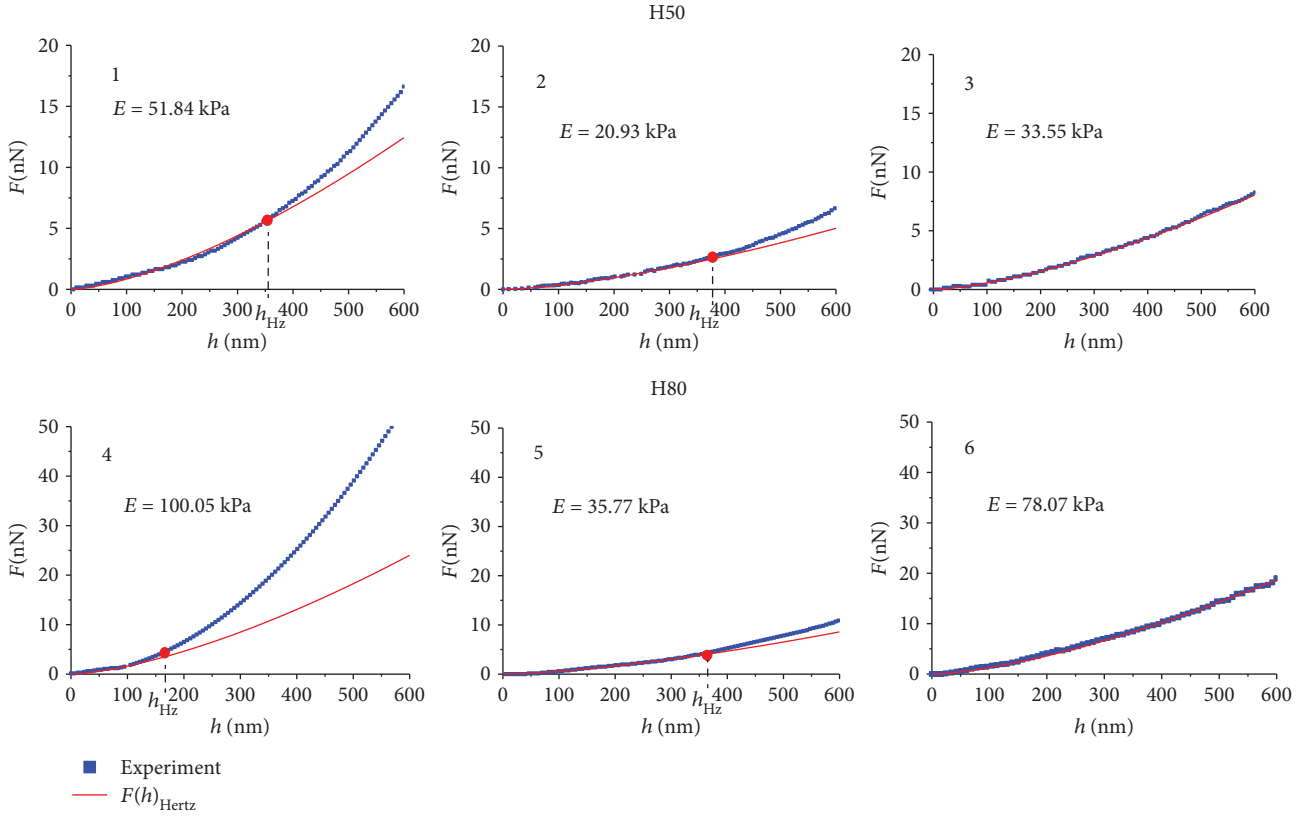


FIGURE 7: Experimental curves $F(h)$ and functions of their approximation by the Hertz model for hemin H50 (nos. 1, 2, and 3) and hemin H80 (nos. 4, 5, and 6); h_{Hz} is the boundary depth of membrane bending, deeper by which approximation by the Hertz model becomes inadequate.

$b_n = 1.03$. This degree indicates that this dependence $F(h)$ was linear after h_{Hz} . $F(h)$ obeyed Hooke's law. In nine cases, the degree was $b_n > 1.5$. So in example no. 10, after the Zn^{2+} action, $h_{Hz} = 169$ nm and $b_n = 1.94$, that is, almost parabolic function.

The values of the membrane bending h_{Hz} , up to which $F(h)$ obeyed the Hertz model, and after which point the degree of the approximating polynomial was varied, lay in a wide range. In the given examples (Figures 7 and 8), the range of h_{Hz} was from 169 nm to 463 nm. If $h_{Hz} = 600$ nm, this means that the total curve is approximated by the Hertz model. In all experiments, Young's modulus E was calculated by the Hertz model to the depth h_{Hz} . These data are indicated in Figures 7 and 8 and in Tables 2 and 3.

With increase in the penetration depth of the probe into the sample $h > h_{Hz}$, the modulus of elasticity was increased (Figures 7 and 8); experimental data (blue) are higher than corresponding function data (red).

To estimate the increase in modulus E after point h_{Hz} , function $F(h)$ was approximated in the interval $h_{Hz} = 600$ nm by a linear function. So for H50, after $h_{Hz} = 385$ nm, Young's modulus E increased 1.6 times (curve 2). For H80 after $h_{Hz} = 170$ nm, modulus E increased by 3.3 times (curve 4). For GA1% after $h_{Hz} = 329$ nm, modulus E increased by 1.8 times (curve 7), and for Zn^{2+} after $h_{Hz} = 169$ nm, modulus E increased by 5.5 times (curve 10). These are only the approximate estimations of the increase in

modulus E . It is not possible to calculate E exactly on this interval, since b_n has different values for each curve than the others. To create a single model for all different b_n is not possible.

4. Discussion

4.1. Elastic Properties of RBC Membranes. In this work, we estimated the membrane's ability to bend into the cell, by atomic force spectroscopy [23] with large radius probes ($R = 150$ nm). In all experiments, only native cells were used. Scanning and obtaining of the force curves $I(Z)$ were carried out only in a liquid medium, namely, buffer solution. It is known that the membrane stiffness strongly depends on the method of sample preparation. So the stiffness of the dry RBC membrane can reach tens of megapascals and more [31]. Moreover, the stiffness of the native cell membrane is of the order of several tens of kilopascals, that is, three or more orders less [5, 30]. Therefore, the first task was to develop a method to obtain samples of native cells on a substrate for further scanning. It was assumed that the use of fixatives and membrane modifiers for the RBCs is unacceptable. The solution of this problem is described in the section Materials and Methods.

Membrane fixatives and modifiers, natural oxidants, and heavy metal ions significantly increased the RBC membrane stiffness.

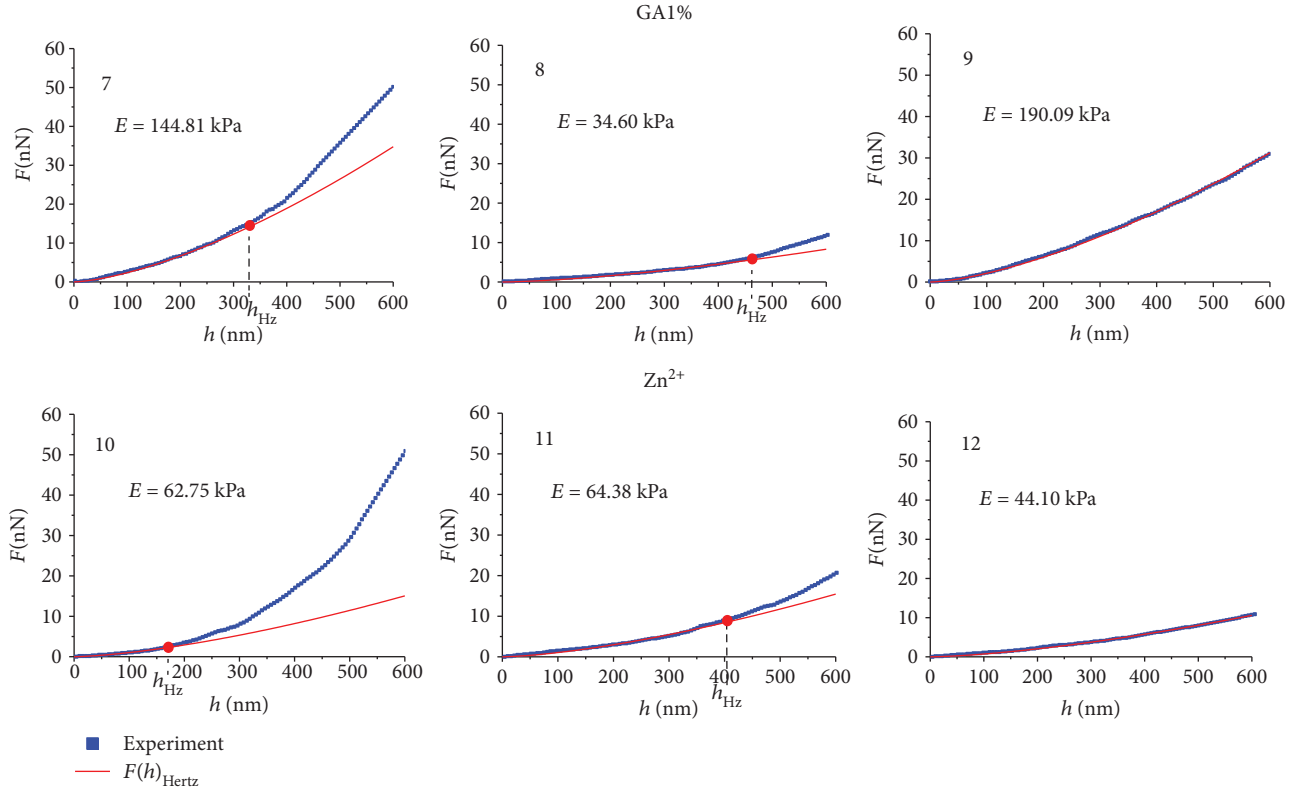


FIGURE 8: Experimental curves $F(h)$ and functions of their approximation by the Hertz model for glutaraldehyde GA1% (nos. 7, 8, and 9) and Zn^{2+} ions (nos. 10, 11, and 12); h_{Hz} is the boundary depth of membrane bending, deeper by which approximation by the Hertz model becomes inadequate.

TABLE 2: Parameters of empirical curves for H50, H80, GA1%, and Zn^{2+} .

	No.	b	a	E (kPa)	h_{Hz} (nm)	h_{max} (nm)	b_n	a_n
H50	1	1.49	$8.45E-04$	51.84	352	600	1.24	0.01
	2	1.50	$3.42E-04$	20.93	385	600	1.27	$3.86E-03$
	3	1.51	$5.48E-04$	33.55	600	600	1.51	$5.48E-04$
H80	4	1.52	$1.64E-03$	100.08	170	600	1.36	0.01
	5	1.51	$5.84E-04$	35.78	367	600	1.07	0.02
	6	1.48	$1.54E-03$	78.10	600	600	1.48	$1.54E-03$
GA 1%	7	1.51	$2.36E-03$	144.82	329	600	1.23	0.04
	8	1.51	$5.65E-04$	34.60	463	600	1.03	0.04
	9	1.49	$2.30E-03$	130.09	600	600	1.49	$2.30E-03$
Zn^{2+}	10	1.51	$1.02E-03$	62.75	169	600	1.94	$3.72E-04$
	11	1.50	$1.05E-03$	64.38	408	600	1.39	$7.66E-03$
	12	1.50	$7.19E-04$	44.10	600	600	1.50	$7.19E-04$

TABLE 3: Statistical data of the values E (for $h < h_{\text{Hz}}$) and h_{Hz} for control and after action of agents.

	Control	H50	H80	GA1%	Zn^{2+}
$E = Em \pm \sigma$, kPa $h < h_{\text{Hz}}$	26.3 ± 4.8	48 ± 13	90 ± 22	119 ± 30	66 ± 19
$h_{\text{Hz}} = h_{\text{Hzm}} \pm \sigma$, nm	≥ 600 nm	421 ± 62	362 ± 79	356 ± 69	371 ± 68

Glutaraldehyde as an RBC fixator at a concentration of 0.2% increased Young's modulus by 2.9 times and at a concentration of 1.0% by 5.4 times (Figure 6(c)).

Hemin is a natural oxidant. The action of hemin on blood leads to an increase in Young's modulus by 3 or more times (Figure 3(a)).

Zn^{2+} ions also increased Young's modulus of RBC membranes by 2.4 times compared to control cells.

Therefore, when GA is used as an RBC fixator in studies of body pathologies (oxidative processes), of exogenous intoxication (metal ions), the obtained absolute values of Young's modulus will always be shifted upwards. Such values cannot be true and can only be used as comparative values.

4.2. Young's Modulus of Native RBC in Control. Control cells were cells of healthy people of both sexes from 20 to 35 years of age. All absolute values of Young's modulus (for 8 people) in our experiment were from above 11 kPa to 41 kPa. The mechanical properties of RBC membranes, in particular their Young's modulus, can be used in clinical practice as a quantitative criterion for assessing the state of blood cell membranes. If E lies within these limits, then we can assume that the deformability of RBC is normal. If the values of Young's modulus differ from the indicated limits, then such cells are subject to additional studies.

4.3. Deep Bending of RBC Membranes ($h_{Hz} - 600$ nm). A characteristic peculiarity of dependences $F(h)$ for deep bending of RBC membranes is that approximating polynomial degree b_n (3) may be changed at depths larger than h_{Hz} , $h > h_{Hz}$ (Figures 7 and 8, Table 2).

But in normal, more than 92% of all RBC membranes of 8 donors gave an empirical curve adequately approximated by the Hertz model even at depths up to 600 nm with a determination coefficient $R^2 \geq 0.95$. Additional frictional forces did not arise (Figure 5(c)).

Under influence of modifiers, the increase in Young's modulus at $h > h_{Hz}$ was determined by additional resistance forces from the membrane itself. Membranes are a complex structure, similar to composites. They consist of a lipid bilayer, globular proteins, and a spectrin matrix, connected with a lipid bilayer by protein complexes of band 3, band 4.1, actin, and ankyrin. The property of the composite structures is their ability to acquire new mechanical properties when changing external conditions. For RBC membranes, such new properties arose at $h > h_{Hz}$ in the spectrin matrix, since it is the main elastic structure in RBC membranes. Additional resistance forces (Figures 7 and 8) were manifested as a result of changes in the elastic properties of the spectrin matrix under the action of modifiers. So $F(h)$ after H50 (small concentration) in 65% cases was approximated by the Hertz model, and only 35% of cases gave an increase in Young's modulus at $h > h_{Hz}$. $F(h)$ for hemin H80 (higher concentration) gave an increase in Young's modulus already in 94% of cases for $h > h_{Hz}$. Both glutaraldehyde GA1% and Zn^{2+} ions also increased the membrane stiffness at depths greater than h_{Hz} (Figure 8, Table 2). This could be caused by the additional tension of the spectrin network and the

penetration of the probe into the region of topological membrane defect (Figure 4(a)).

In 100% of cases, the empirical data curve $F(h)$ after point h_{Hz} was located on the graph above the approximation curve. This means that at the depths of the RBC membrane bending larger than h_{Hz} , the membranes became stiffer and their Young's modulus increased. Thus, to depths h_{Hz} , modulus $E = \text{const}$ and RBC membranes behaved as homogeneous elastic structures. RBCs had the maximum ability to deform. After this depth, modulus E increased, and for each cell according to its individual law (b_n and a_n for each cell had its own value). The membranes became stiffer. Thus, the ability of RBC to deform deeply is constant for healthy organisms and decreases with the action of modifiers and exogenous intoxications.

5. Conclusion

In this study, it was shown that the absolute values of Young's modulus of native RBC membranes strongly depend on the action of fixatives and factors of intoxication. The method of forming native RBC samples without fixatives was used. It was shown that under bending to depth $h_{Hz} \approx 0.5 \mu\text{m}$, native RBC membranes behave as homogeneous elastic structures with a constant Young's modulus. This is very important because this bending depth coincides with the typical deformation of RBC membrane in microcirculation.

The possibility of using modulus E as a quantitative criterion for estimating the membrane state of native cells without modifiers was discussed. At the depths of bending h greater than h_{Hz} , the mechanical characteristics of the membranes are no longer described by the Hertz model. Stiffness increases according to nonlinear laws, and membranes acquire new mechanical properties. The results of the work can be used in clinical practice, in assessing the quality of stored donor blood for transfusion, in biophysical studies of RBC properties.

Data Availability

All data used to support the findings of this study are included within the article.

Conflicts of Interest

The authors declare that there is no conflict of interest regarding the publication of this article.

Acknowledgments

The authors thank Olga Gudkova for help in preparation of the manuscript. This work has been supported by the Ministry of Science and Higher Education of the Russian Federation and by the Russian Academic Excellence Project 5-100.

References

- [1] S. Barns, M. A. Balanant, E. Sauret, R. Flower, S. Saha, and Y. T. Gu, "Investigation of red blood cell mechanical properties using AFM indentation and coarse-grained particle

- method," *BioMedical Engineering OnLine*, vol. 16, no. 1, p. 140, 2017.
- [2] C. H. Wang and A. S. Popel, "Effect of red blood cell shape on oxygen transport in capillaries," *Mathematical Biosciences*, vol. 116, no. 1, pp. 89–110, 1993.
 - [3] G. Tomaiuolo, "Biomechanical properties of red blood cells in health and disease towards microfluidics," *Biomicrofluidics*, vol. 8, no. 5, article 051501, 2014.
 - [4] N. Mohandas and J. A. Chasis, "Red blood cell deformability, membrane material properties and shape: regulation by transmembrane, skeletal and cytosolic proteins and lipids," *Seminars in Hematology*, vol. 30, no. 3, pp. 171–192, 1993.
 - [5] E. Kozlova, A. Chernysh, V. Moroz, V. Sergunova, O. Gudkova, and E. Manchenko, "Morphology, membrane nanostructure and stiffness for quality assessment of packed red blood cells," *Scientific Reports*, vol. 7, no. 1, p. 7846, 2017.
 - [6] M. Takeuchi, H. Miyamoto, Y. Sako, H. Komizu, and A. Kusumi, "Structure of the erythrocyte membrane skeleton as observed by atomic force microscopy," *Biophysical Journal*, vol. 74, no. 5, pp. 2171–2183, 1998.
 - [7] M. Li, L. Liu, N. Xi et al., "Atomic force microscopy imaging and mechanical properties measurement of red blood cells and aggressive cancer cells," *Science China Life Sciences*, vol. 55, no. 11, pp. 968–973, 2012.
 - [8] A. S. Kamruzzahan, F. Kienberger, C. M. Stroh et al., "Imaging morphological details and pathological differences of red blood cells using tapping-mode AFM," *Biological Chemistry*, vol. 385, no. 10, pp. 955–960, 2004.
 - [9] S. G. Shroff, D. R. Saner, and R. Lal, "Dynamic micromechanical properties of cultured rat atrial myocytes measured by atomic force microscopy," *American Journal of Physiology-Cell Physiology*, vol. 269, no. 1, pp. C286–C292, 1995.
 - [10] I. Dulińska, M. Targosz, W. Strojny et al., "Stiffness of normal and pathological erythrocytes studied by means of atomic force microscopy," *Journal of Biochemical and Biophysical Methods*, vol. 66, no. 1–3, pp. 1–11, 2006.
 - [11] X. Sisquella, T. Nebl, J. K. Thompson et al., "Plasmodium falciparum ligand binding to erythrocytes induce alterations in deformability essential for invasion," *eLife*, vol. 6, article e21083, 2017.
 - [12] A. Vayá, L. Rivera, R. de la Espriella et al., "Red blood cell distribution width and erythrocyte deformability in patients with acute myocardial infarction," *Clinical Hemorheology and Microcirculation*, vol. 59, no. 2, pp. 107–114, 2015.
 - [13] G. A. Barabino, M. O. Platt, and D. K. Kaul, "Sickle cell biomechanics," *Annual Review of Biomedical Engineering*, vol. 12, no. 1, pp. 345–367, 2010.
 - [14] M. Fornal, M. Lekka, G. Pyka-Foćiak et al., "Erythrocyte stiffness in diabetes mellitus studied with atomic force microscope," *Clinical Hemorheology and Microcirculation*, vol. 35, no. 1–2, pp. 273–276, 2006.
 - [15] M. Papi, G. Ciasca, V. Palmieri et al., "Nano-mechanical response of red blood cells," in *Mechanics of Biological Systems and Materials, Volume 6*, C. S. Korach, S. A. Tekalur, and P. Zavattieri, Eds., pp. 11–16, Springer, 2017.
 - [16] M. Girasole, S. Dinarelli, and G. Boumis, "Structure and function in native and pathological erythrocytes: a quantitative view from the nanoscale," *Micron*, vol. 43, no. 12, pp. 1273–1286, 2012.
 - [17] M. Starodubtseva, S. Chizhik, N. Yegorenkov, I. Nikitina, and E. Drozd, "Study of the mechanical properties of single cells as biocomposites by atomic force microscopy," *Microscopy: Science, Technology, Applications and Education*, vol. 1, pp. 470–477, 2010.
 - [18] V. A. Sergunova, E. K. Kozlova, E. A. Myagkova, and A. M. Chernysh, "In vitro measurement of the elastic properties of the native red blood cell membrane," *General Reanimatology*, vol. 11, no. 3, p. 39, 2015.
 - [19] C. C. Lien, M. C. Wu, and C. Ay, "Study on the Young's modulus of red blood cells using atomic force microscope," *Applied Mechanics and Materials*, vol. 627, pp. 197–201, 2014.
 - [20] E. K. Kozlova, A. M. Chernysh, V. V. Moroz, and A. N. Kuzovlev, "Analysis of nanostructure of red blood cells membranes by space Fourier transform of AFM images," *Micron*, vol. 44, pp. 218–227, 2013.
 - [21] E. Kozlova, A. Chernysh, V. Moroz, O. Gudkova, V. Sergunova, and A. Kuzovlev, "Transformation of membrane nanosurface of red blood cells under hemin action," *Scientific Reports*, vol. 4, no. 1, 2014.
 - [22] W. Zhang and F. Liu, "Effect of polylysine on blood clotting, and red blood cell morphology, aggregation and hemolysis," *Journal of Nanoscience and Nanotechnology*, vol. 17, no. 1, pp. 251–255, 2017.
 - [23] A. M. Chernysh, E. K. Kozlova, V. V. Moroz et al., "Nonlinear local deformations of erythrocyte membranes: normal erythrocytes (part 1)," *General Reanimatology*, vol. 13, no. 5, pp. 58–68, 2017.
 - [24] S. Garcia-Manyes and F. Sanz, "Nanomechanics of lipid bilayers by force spectroscopy with AFM: a perspective," *Biochimica et Biophysica Acta (BBA) - Biomembranes*, vol. 1798, no. 4, pp. 741–749, 2010.
 - [25] G. Thomas, N. A. Burnham, T. A. Camesano, and Q. Wen, "Measuring the mechanical properties of living cells using atomic force microscopy," *Journal of Visualized Experiments*, no. 76, article e50497, 2013.
 - [26] H. Hertz, "Ueber den kontakt elastischer koerper," *Journal für die Reine und Angewandte Mathematik*, vol. 92, pp. 245–260, 1881.
 - [27] V. C. Bui, Y. U. Kim, and S. S. Choi, "Physical characteristics of *Saccharomyces cerevisiae*," *Surface and Interface Analysis*, vol. 40, no. 10, pp. 1323–1327, 2008.
 - [28] M. Radmacher, M. Fritz, C. M. Kacher, J. P. Cleveland, and P. K. Hansma, "Measuring the viscoelastic properties of human platelets with the atomic force microscope," *Biophysical Journal*, vol. 70, no. 1, pp. 556–567, 1996.
 - [29] B. Codan, V. Martinelli, L. Mestroni, and O. Sbaizero, "Atomic force microscopy of 3T3 and SW-13 cell lines: an investigation of cell elasticity changes due to fixation," *Materials Science & Engineering. C, Materials for Biological Applications*, vol. 33, no. 6, pp. 3303–3308, 2013.
 - [30] T. G. Kuznetsova, M. N. Starodubtseva, N. I. Yegorenkov, S. A. Chizhik, and R. I. Zhdanov, "Atomic force microscopy probing of cell elasticity," *Micron*, vol. 38, no. 8, pp. 824–833, 2007.
 - [31] S. Strasser, A. Zink, G. Kada et al., "Age determination of blood spots in forensic medicine by force spectroscopy," *Forensic Science International*, vol. 170, no. 1, pp. 8–14, 2007.

Research Article

AFM Characterization of the Internal Mammary Artery as a Novel Target for Arterial Stiffening

Zhuo Chang,^{1,2} Paolo Paoletti,¹ Maria Lyck Hansen,³ Hans Christian Beck,³ Po-Yu Chen,² Lars Melholt Rasmussen,³ and Riaz Akhtar ¹

¹Department of Mechanical, Materials and Aerospace Engineering, School of Engineering, University of Liverpool, L69 3GH, UK

²Department of Materials Science and Engineering, National Tsing Hua University, Hsinchu 30013, Taiwan

³Department of Clinical Biochemistry and Pharmacology, Center for Individualized Medicine in Arterial Diseases, Odense University Hospital, University of Southern Denmark, Denmark

Correspondence should be addressed to Riaz Akhtar; r.akhtar@liverpool.ac.uk

Received 1 July 2018; Accepted 6 September 2018; Published 5 November 2018

Guest Editor: Andreas Stylianou

Copyright © 2018 Zhuo Chang et al. This is an open access article distributed under the Creative Commons Attribution License, which permits unrestricted use, distribution, and reproduction in any medium, provided the original work is properly cited.

Using the atomic force microscopy- (AFM-) PeakForce quantitative nanomechanical mapping (QNM) technique, we have previously shown that the adventitia of the human internal mammary artery (IMA), tested under dehydrated conditions, is altered in patients with a high degree of arterial stiffening. In this study, we explored the nanoscale elastic modulus of the tunica media of the IMA in hydrated and dehydrated conditions from the patients with low and high arterial stiffening, as assessed *in vivo* by carotid-femoral pulse wave velocity (PWV). In both hydrated and dehydrated conditions, the medial layer was significantly stiffer in the high PWV group. The elastic modulus of the hydrated and dehydrated tunica media was significantly correlated with PWV. In the hydrated condition, the expression activity of certain small leucine-rich repeat proteoglycans (SLRPs), which are associated with arterial stiffening, were found to be negatively correlated to the medial elastic modulus. We also compared the data with our previous work on the IMA adventitia. We found that the hydrated media and dehydrated adventitia are both suitable for reflecting the development of arterial stiffening and SLRP expression. This comprehensive study of the nanomechanical properties integrated with the proteomic analysis in the IMAs demonstrates the possibility of linking structural properties and function in small biological samples with novel AFM methods. The IMA is a suitable target for predicting arterial stiffening.

1. Introduction

In clinical practice, arterial stiffening is commonly assessed with pulse wave velocity (PWV). PWV measurements are made *in vivo* by recording the transit time of blood across two points in the vascular system, typically from the carotid to the femoral artery. PWV is considered a powerful predictor of risk of morbidity and mortality in a general population [1, 2]. However, arteries are associated with complex structural and biomechanical processes that occur as arteries stiffen with age and disease. These alterations are not captured with PWV which simply averages the properties of the vasculature across a relatively large distance. High spatial resolution techniques such as atomic force microscopy (AFM) can bridge the gap in our understanding by enabling

localized biomechanical and ultrastructural measurements on isolated sections of vascular tissue.

A number of studies have utilized high spatial resolution techniques to probe arterial stiffening *in vitro*, e.g., [3, 4]. However, these studies are generally restricted to animal models due to obvious challenges in conducting measurements on human aortic tissues. Hence, a direct link between clinical PWV and *in vitro* micro-/nanomechanical properties has long remained a challenge. Recently, the internal mammary artery (IMA) has emerged as an excellent vessel for studying the pathogenesis of arterial stiffening, especially at the molecular level [5–9]. It is readily accessible as the repair artery during coronary artery bypass graft (CABG) operations. Although it is not involved in the carotid-femoral PWV pathway, we have recently shown using AFM that

alterations in nanomechanical properties and collagen fibril morphology in the IMA adventitia are strongly correlated with high PWV [1]. Furthermore, the IMA has been used in a parallel study to identify small leucine-rich proteoglycans (SLRPs) which are associated with arterial stiffening [9]. Thus, the IMA can be used to directly measure relevant properties at the ultrastructural and molecular level in patients with high PWV, overcoming the impracticability of obtaining vascular tissue from the PWV pathway.

Although the PeakForce QNM has been recently used to probe biological samples under physiological conditions [10–14], our previous study was the first to apply PeakForce QNM to vascular tissues [1]. This paper builds on that study [1] which demonstrated with PeakForce QNM AFM [15, 16] that the adventitia of the IMA is altered in patients with high PWV, in terms of both the nanoscale elastic modulus and the collagen fibril morphology. We now extend the approach and apply PeakForce QNM to the medial layer of the IMA in both dehydrated and hydrated conditions. To the best of our knowledge, this is the first study to apply the PeakForce QNM for soft tissue nanomechanical characterization in fully hydrated conditions. The paper compares the nanoscale elastic modulus of the medial layer in dehydrated and hydrated conditions, and for both conditions, the relation between this AFM data, patient metadata and proteomics data is explored. Furthermore, the dehydrated medial measurements are compared with the dehydrated adventitia measurements to determine the best approach when utilizing the IMA as an arterial stiffening target with AFM. The literature on the layer-specific biomechanical properties of the human artery is sparse, and thus this gap is addressed.

2. Materials and Methods

2.1. Patient Information. The IMA is the repair artery for CABG operations. In this study, all of the IMAs were collected from 17 patients as waste materials after the CABG operation at the Centre of Individualized Medicine in Arterial Diseases (Odense University Hospital, Odense, Denmark), as part of a project approved by the Local Ethical Committee in Region Southern Denmark (S-2010044).

Before the coronary artery bypass graft, patients were assessed by carotid-femoral PWV by using the SphygmoCor system under standardized conditions as previously described in [9]. Clinical data, including age, gender, diabetes, and hypertension, were collected before the surgery. Based on the reference and normal values for carotid-femoral PWV [17], the 17 patients were split into two groups: low PWV ($8.5 \pm 0.7 \text{ ms}^{-1}$, $n = 8$ patients) and high PWV ($13.4 \pm 3.0 \text{ ms}^{-1}$, $n = 9$ patients). Full patient clinical parameters are presented in [1]. It should be noted that the tissue samples and patient cohorts are identical to those in our previous paper which focussed on the IMA adventitia [1]. However, the testing location (medial layer) and methodology (dehydrated and hydrated) are different.

2.2. PeakForce QNM in Ambient Conditions. AFM testing was conducted on $5 \mu\text{m}$ cryosections with the PeakForce

QNM method using a MultiMode 8 Atomic Force Microscopy (AFM) (NanoScope VIII MultiMode AFM, Bruker Nano Inc., Nano Surface Division, Santa Barbara, CA). The method has been explained in detail elsewhere [1]. All measurements were conducted with Bruker RTESPA-150 etched silicon probes. These probes have a nominal radius of 8 nm and a cantilever with a nominal spring constant of 5 Nm^{-1} and resonant frequency of 150 kHz . The spring constant and tip radius of the probe were calibrated before measurements. In addition, a photostress coating polymer reference sample (PS1, Vishay Precision Group, Heilbronn, Germany) with known elastic modulus was used to calibrate the mechanical measurements [1].

For these measurements, the scan rate was fixed at 0.93 Hz , and the resolution was set at 256 pixels per line with fixed scan size ($2 \times 2 \mu\text{m}^2$). For mechanical characterization, 65,536 measurements (256×256 independent force curves) were obtained for each image to yield the mean elastic modulus. All AFM raw files were processed with the Bruker NanoScope Analysis version 1.5. To identify the internal elastic lamellae (IEL) and external elastic lamellae (EEL) for localized measurement, the optical microscopy integrated with the AFM setup was utilized (Figure 1). Three random localized areas were probed in the media of each tissue section. Two sections were studied for each patient. Thus, there were six measurements of nanomechanical properties for each patient.

2.3. PeakForce QNM in Fluid Conditions. With the same AFM system, testing in fluid conditions was possible in a fluid cell (MTFEM, Bruker). A Bruker ScanAsyst-Fluid probe with an intentionally blunt tip (nominal tip radius = 20 nm) and extremely low spring constant (nominal spring constant = 0.7 Nm^{-1} , resonant frequency = 150 kHz) was applied to image the delicate hydrated tissue sections in distilled water. The tip radius and spring constant of the probe were calibrated using the same procedure as used in ambient conditions [1]. Following this, a polydimethylsiloxane (PDMS) sample was used as the reference sample for modulus measurement calibration. The elastic modulus of PDMS was determined independently via nanoindentation (Nano Indenter G200 with a DCM II Head, KLA-Tencor, Milpitas, CA, USA) utilizing a $100 \mu\text{m}$ flat punch (Synton-MDP Ltd, Nidau, Switzerland) before the calibration. The testing was conducted at 110 Hz using an oscillatory nanoindentation method [1]. The nanoindentation data yielded an average elastic modulus of $5.1 \pm 0.36 \text{ MPa}$.

During liquid testing, sharp tips can drag across the hydrated soft tissue and cause damage to the tissue, thus causing errors in mechanical mapping. With the scan size set to $2 \times 2 \mu\text{m}$ with a slow scanning rate (less than 0.501 Hz), the mechanical mapping in liquid was found to be more reliable. Hence, for comparative purposes, imaging in ambient conditions was also kept at $2 \times 2 \mu\text{m}$. The scan rate for the fluid tests was kept constant at 0.501 Hz . Further, due to the highly sensitive surface of the hydrated tissue samples, a higher scanning resolution was applied in the fluid conditions as compared with the measurements in ambient conditions. Thus, 384 samples/line were selected

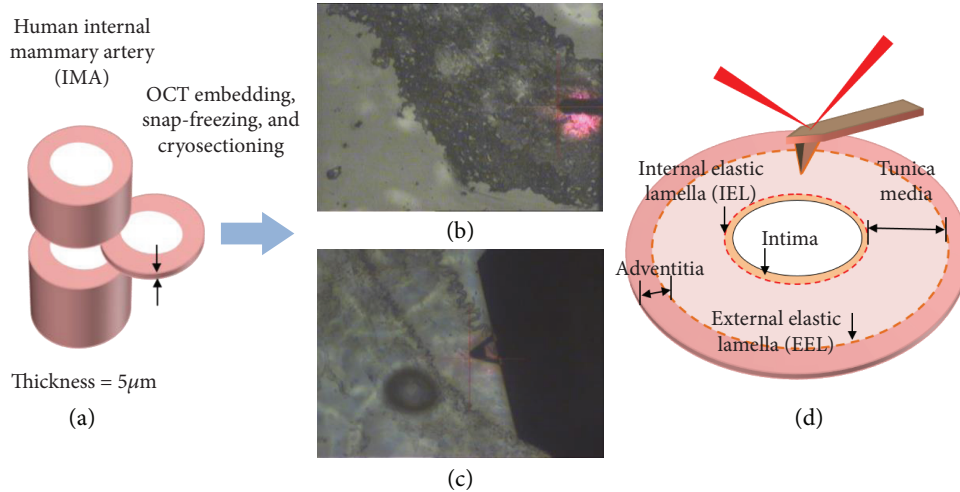


FIGURE 1: The approach for localized nanomechanical mapping of the tunica media in human IMA. (a) The human internal mammary artery (IMA) was cryo-sectioned to 5 μm thickness tissue sections. Optical images captured with the microscope integrated with the AFM for the (b) dehydrated and (c) hydrated tissue sections. The IEL and EEL distinctly separate the tunica intima, tunica media, and tunica adventitia in the IMA. (d) Schematic diagram of AFM imaging and the IMA histology.

and 147,456 (384×384) independent force curves were obtained in each image to yield the mean elastic modulus. Example force-indentation curves are shown in Figure 2 for our reference samples in ambient and fluid conditions.

For each patient, two tissue sections were imaged with three random locations selected per tissue section. Thus, there were a total of six measurements per patient. However, samples from three patients (ID: 552 in low PWV, and 620 and 643 in high PWV; see Supporting Information, Table S1 in [1]) were unintentionally damaged during the hydration process and could not be studied. Thus, in total, seven patients in the low and high PWV groups were examined in the fluid condition.

2.4. Integration of Quantitative Proteomics, Nanomechanical Data, and Patient Metadata. Quantitative proteomics data for some of the patient cohort analyzed in this study were available from a larger cohort study published by Hansen et al. [9]. Full methodological data for these measurements can be found in their paper. The data available was for the 7 SLRP proteins that were found to be downregulated in the high PWV patients, namely, lumican, mimecan, prolargin, asporin, podocan, decorin, and biglycan [9]. To integrate the nanomechanical data acquired in this study with both proteomics data and patient metadata, a multivariate transformation called principal component analysis (PCA) was used.

2.5. Statistical Methods. Patient characteristics were presented as mean \pm SD, and all the bar charts were presented as mean \pm SEM. All patient measurements were averaged prior to statistical analysis. Group differences were assessed via a suitable 2-sample independent test selected after appraisal of data normality and homoscedasticity. Differences between nanomechanical properties of hydrated and dehydrated media of the low and high PWV group were tested with the Mann-Whitney U test. Kolmogorov-Smirnov

(K-S) tests were applied to assess the statistical significance in distribution of nanomechanical properties of hydrated and dehydrated media between the low and high PWV groups. Spearman's correlation coefficient was used to test relationships between the measured elastic modulus of hydrated and dehydrated media and the PWV as well as with SLRPs expression activity. Proteomics data were analyzed in junction with nanomechanical variables and quantitative metadata variables (i.e., age, BMI, cholesterol, and HbA1c) of all the patients via the unsupervised data transformation PCA. All statistical analyses were tested using OriginPro version 9 (OriginLab, Northampton, MA).

3. Results and Discussion

In this study, the nanomechanical properties of hydrated and dehydrated media were assessed to determine the utility of this AFM for testing hydrated tissues. Assessment of the IMA medial layer in the different conditions is also compared with the adventitia data and evaluated with correlation analysis to assess the best approach for determining arterial stiffness from IMA samples. Histological assessment can be found in [1].

3.1. Nanomechanical Properties of Dehydrated Media. In ambient conditions, patients with high PWV had a stiffer medial ultrastructure than that of the low PWV group (low PWV = 2116.2 ± 523.1 MPa; high PWV = 3163.6 ± 548.7 MPa, Mann-Whitney U test, $p = 0.003$) (Figure 3(a)). The elastic modulus ranged from 1325.5 to 2770.7 MPa and 2520.3 to 4030.0 MPa in the low and high PWV groups, respectively. Modulus distribution between these two groups was also found to be significantly different (Kolmogorov-Smirnov test, $p < 0.0001$) (Figure 3(b)).

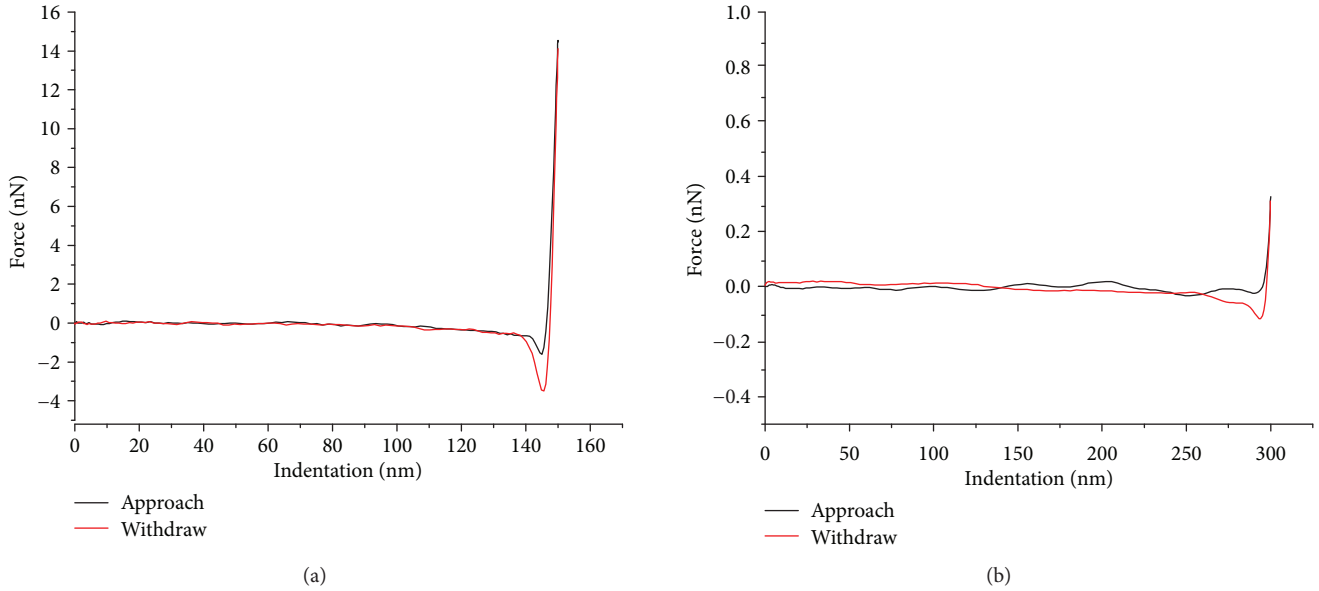


FIGURE 2: Examples of AFM force-indentation curves obtained from (a) PS1 and (b) PDMS reference samples in ambient and fluid conditions, respectively.

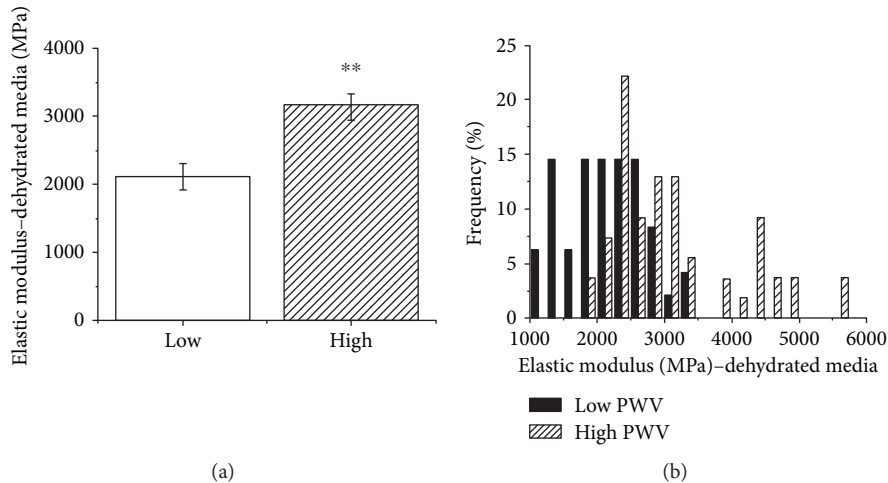


FIGURE 3: Nanomechanical properties of the dehydrated media in both groups in ambient condition. (a) Bar graph showing a significant difference in elastic modulus of patients as mean \pm SEM ($n=8$ patients in low PWV group; $n=9$ patients in high PWV group). (b) Distribution of measured elastic modulus for both groups; significant differences were found between modulus distributions of two groups overall in the dehydrated media (Kolmogorov-Smirnov test, $p < 0.0001$).

3.2. Nanomechanical Properties of Hydrated Media. With the hydrated samples, similar trends were observed as those in ambient conditions; i.e., the elastic modulus was higher in the high PWV group. However, the trends were more pronounced in these conditions. In the high PWV group, the medial layer was approximately three times stiffer than that in the low PWV group (low PWV group = 250.6 ± 39.0 kPa; high PWV group = 721.7 ± 291.9 kPa, Mann-Whitney U test, $p = 0.005$) (Figure 4(a)). The measured elastic modulus of the patients ranged from 180.1 to 292.7 kPa and 286.6 to 1114.7 kPa in the low and high PWV groups, respectively. A significant difference was found between modulus distributions in the two groups (Kolmogorov-Smirnov test, $p < 0.0001$) (Figure 4(b)).

The mean elastic modulus was found to be 188% larger in the high PWV group as compared to the low PWV group. In comparison, an increase of 52% was observed when the tissues were dehydrated. The absolute values differed vastly in the two conditions with the elastic modulus being around three times higher when the tissue was tested dehydrated (Table 1). These data highlight the importance of water content in governing the mechanical properties of soft biological tissues.

The distribution of data was further assessed by examining the skewness and kurtosis as shown in Table 1. The low PWV group had a negative skewness in both hydration conditions whereas the high PWV group had a positive skewness. The kurtosis parameter was negative and

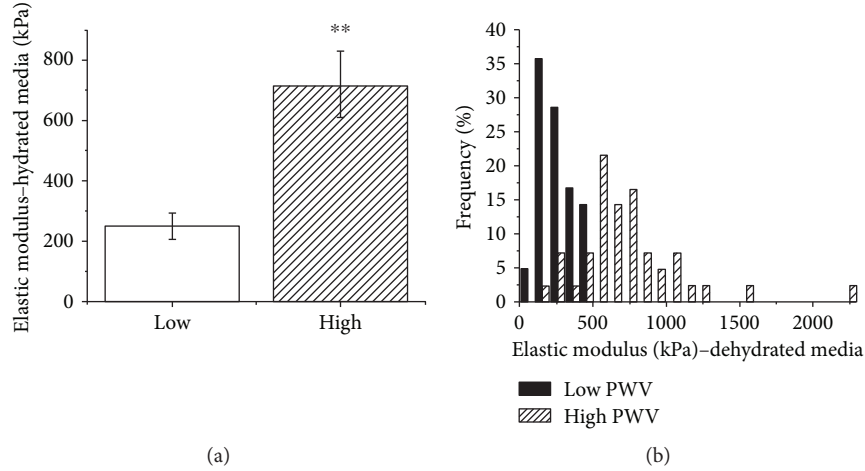


FIGURE 4: Nanomechanical properties of the hydrated media in the fluid condition in all available patients. (a) The elastic modulus of hydrated media in each patient ($n = 7$ patients per group, Mann–Whitney test, $p = 0.005$). (b) Modulus distribution of the medial layer in low and high PWV groups ($n = 42$ measurements per group, Kolmogorov–Smirnov test, $p < 0.0001$).

TABLE 1: Mean, median, standard deviation (SD), standard error (SE), skewness, and kurtosis for the elastic modulus data are presented for the hydrated and dehydrated IMA media.

		n	Mean	Median	SD	SE	Skewness	Kurtosis
Hydrated media (kPa)	Low PWV	7	250.5	255.4	39.1	14.8	-0.9	0.8
	High PWV	7	721.7	649.6	291.9	110.3	0.2	-0.4
Dehydrated media (MPa)	Low PWV	8	2116.2	2142.3	523.1	184.9	-0.3	-1.2
	High PWV	9	3163.6	3044.5	548.7	182.9	0.6	-1.1

approximately equivalent for the dehydrated media in both the low and high PWV groups. However, for the hydrated media, the kurtosis parameter was positive in the low PWV group and closer to zero in the high PWV group. Thus, in hydrated conditions, the tails in the elastic modulus distributions are more pronounced.

Figure 5 shows example AFM images for the medial layer in both dehydrated and hydrated conditions. The IMA is a transition artery, and in many patients, it is not classified as an elastic artery and hence does not have any elastic lamellae present [1]. Hence, the AFM images show an amorphous-type structure with little evidence of any fibrillar structure. This is more pronounced in the dehydrated images where the topographical variation is less pronounced (Figures 5(d) and 5(e)).

Although there are no other studies in the literature which have reported the elastic modulus of the human IMA medial layer, we can compare our values with other relevant published studies. Sicard et al. [18] reported values for human pulmonary arteries measured with AFM using a sharp pyramidal tip as being 67.66 ± 122.26 kPa with a range of 4.24–804.00 kPa. Akhtar et al. [4] used a frequency-modulated AFM method for characterizing the medial layer of young and old sheep aorta and reported a geometric mean of 42.9 ± 2.26 kPa for young sheep and 113.9 ± 2.57 kPa for old sheep. Grant and Twigg [19] used AFM with a $10 \mu\text{m}$ tip to characterize the adventitial layer of porcine pulmonary arteries and porcine aorta. For the

pulmonary arteries, they reported a range of 2.3–1130 kPa with a mean of 88.9 kPa, and for the porcine aorta a range of 0.7–391 kPa with a mean of 15.8 kPa. Our mean values are higher than each of these studies but within an acceptable range. Further work is needed to determine whether the difference is due to the test methods or the type of artery. Grant and Twigg [19] highlighted that there was considerable heterogeneity within arteries which also explains the large range of values.

3.3. Comparison of the Dehydrated Medial Layer vs. Dehydrated Adventitial Layer. We have previously published data demonstrating the utility of the IMA adventitial layer as a potential target for arterial stiffening studies [1]. Here, we now compare the mechanical data of dehydrated media with the adventitial data for the same patients [1], as well as the trends when the data are averaged for both layers (media and adventitia). These data are shown in Table 2. Overall, the elastic modulus in each condition was significantly increased in the high PWV relative to the low PWV group (low PWV: $n = 8$ patients; high PWV: $n = 9$ patients). Although there was no statistical difference in the measured elastic modulus between the dehydrated media and adventitia in each group (Mann–Whitney U test, $p > 0.05$), the dehydrated media was slightly stiffer than the dehydrated adventitia in the high PWV group. In the high PWV group, the ultrastructural stiffness increased by 49.5% and 34.1% for the dehydrated

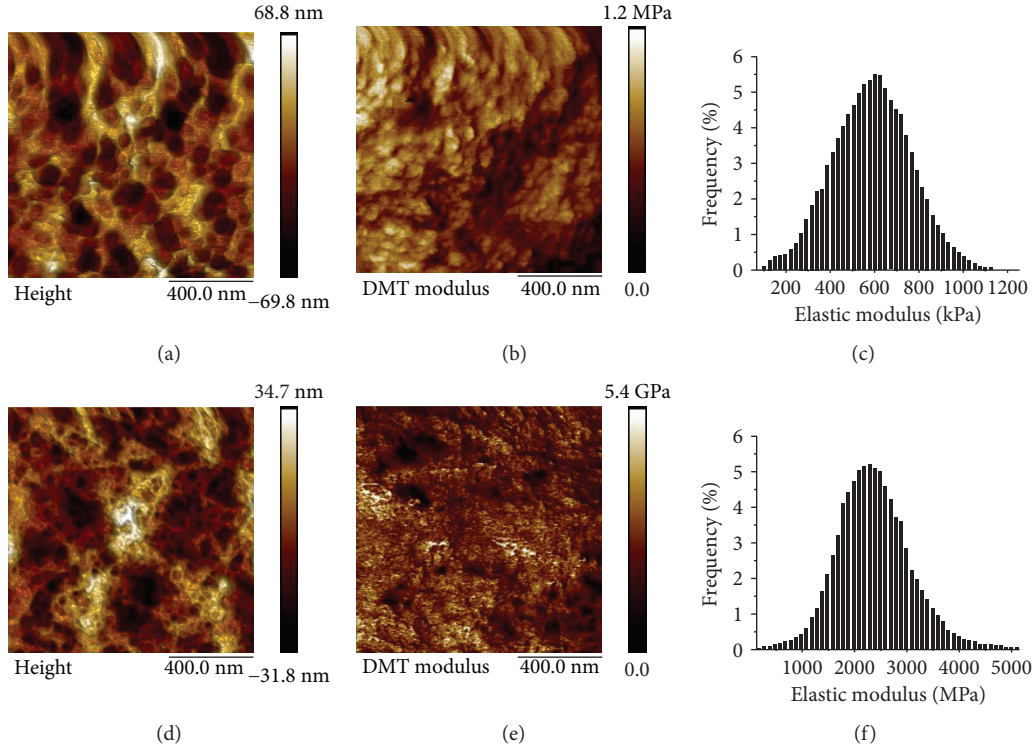


FIGURE 5: Example images showing the hydrated media (a) topography, (b) DMT modulus map, (c) histogram showing the elastic modulus distribution and for the dehydrated media, (d) topography, (e) DMT modulus map, and (f) histogram showing the elastic modulus distribution and for the dehydrated media mapping of topography. All images are for patient 627.

TABLE 2: Elastic modulus for the media, adventitia, and media + adventitia for the IMA tested when dehydrated. The Mann-Whitney U test was used to test the statistical difference between each layer of the low and high PWV groups.

	Media	Adventitia	Media and adventitia
Low PWV			
n	8	8	8
Mean (MPa)	2116.2	2159.3	2137.7
SD (MPa)	523.1	282.5	353.0
Coefficient of variation (%)	24.7	13.1	16.5
High PWV			
n	9	9	9
Mean (MPa)	3163.6	2895.2	3029.4
SD (MPa)	548.7	414.4	380.7
Coefficient of variation (%)	17.3	14.3	12.6
p value	0.003	0.002	0.002

media and adventitia, respectively. For the combined layer group, the elastic modulus increased by 41.7% in the high PWV group.

3.4. Correlation Analysis. To assess the relationships between nanomechanical properties (PWV) and SLRP expression activity, Spearman's rank-order correlation was used to

calculate the correlation coefficient for the relationships to test their significance (Table 3).

Overall, as shown in Table 3, the nanomechanical properties of hydrated and dehydrated media were significantly and positively correlated with the patient's PWV value, which was similar to the dehydrated adventitia [1]. The elastic modulus of the combined dehydrated media and adventitia was also positively related to the PWV data. These findings suggest that all four methods can be utilized to reflect clinical arterial stiffness, i.e., dehydrated adventitia, dehydrated media, or hydrated media.

For correlations between SLRP expression and nanomechanical properties of different layers in all the available patients ($n = 12$ patients for both conditions) (Table 3), 4 of 7 SLRPs showed a significant and negative correlation with measured elastic modulus of hydrated media. This corresponds to our previous study [9] where 5 of 7 SLRPs (lumican, mimecan, prolargin, aspirin, and decorin) were downregulated in patients with high PWV.

SLRPs as a family of complex and diverse macromolecules in arterial wall play an essential role in atherosclerosis [20] and arterial ECM remodeling [21]. The quantitative proteomics data collected from our previous study [9] from the entire IMA tissue have now been compared with nanomechanical measurements for the media (dehydrated and hydrated) and the adventitia (dehydrated), as well as for the media and adventitia combined (dehydrated). The correlation analysis indicates that the nanomechanical properties of the hydrated media are more related to the

TABLE 3: Spearman’s rank-order correlation for assessing correlations of elastic modulus (E) of the different layers, PWV and SLRP expressions.

		Hydrated media	Dehydrated media	Dehydrated adventitia	Dehydrated media and adventitia
Number of patients	<i>n</i>	14	17	17	17
PWV	<i>r</i>	0.63	0.62	0.56	0.62
	<i>p</i>	0.017*	0.008**	0.02*	0.009**
Number of patients	<i>n</i>	12	12	12	12
Lumican	<i>r</i>	-0.71	-0.20	-0.50	-0.30
	<i>p</i>	0.01**	0.54	0.10	0.34
Mimecan	<i>r</i>	-0.54	-0.02	-0.45	-0.22
	<i>p</i>	0.07	0.95	0.15	0.50
Prolargin	<i>r</i>	-0.72	-0.48	-0.52	-0.38
	<i>p</i>	0.008**	0.12	0.09	0.23
Asporin	<i>r</i>	-0.62	-0.51	-0.39	-0.37
	<i>p</i>	0.033*	0.09	0.21	0.24
Podocan	<i>r</i>	-0.48	-0.27	-0.34	-0.18
	<i>p</i>	0.11	0.39	0.28	0.57
Decorin	<i>r</i>	-0.63	-0.22	-0.34	-0.22
	<i>p</i>	0.028*	0.48	0.29	0.48
Biglycan	<i>r</i>	-0.15	-0.12	-0.20	-0.07
	<i>p</i>	0.63	0.71	0.53	0.83

expression activity of SLRPs than the dehydrated media. This further highlights the importance of testing the tissue in conditions that mimic the physiological environment as much as possible.

SLRPs are essential in the structural integrity and functionality of the arterial wall by modulating synthesis, assembly, and remodeling of arterial ECM components such as collagen, elastin, and SMCs. The role of SLRPs in arterial stiffening, as well as on regulating collagen fibril assembly and architecture, has been discussed in detail elsewhere [9], and their relationship to adventitial collagen fibril morphology and nanomechanics has recently been established [1]. Alongside controlling collagen fibrillogenesis and collagen organization, studies have revealed the importance of SLRPs in regulating proliferation and migration of SMCs, which are predominant in the media of muscular arteries. Accumulated lumican, which is expressed in the SMCs, is located in the fibrous thickened intima and media where it associates with intimal thickening and is capable of maintaining adventitial mechanical properties in patients with atherosclerosis [22]. Highly expressed mimecan found in human SMCs is shown to accelerate cell proliferation, migration, and death, thereby regulating atherosclerosis [23] and atherosclerotic plaques [24]. Biglycan promotes SMC proliferation and migration in arteriosclerotic lesions related to arterial repair and pathogenesis of vascular injury [25]. Upregulated decorin is discovered in calcified regions in human atherosclerotic lesions, where it accelerates SMC calcification [26]. These important roles of SLRPs in the medial layer help shed

light on why the SLRP expression is highly correlated with the medial layer nanomechanical properties.

3.5. Principle Component Analysis (PCA). The variables measured in this study were summarized and integrated with the SLRP data by PCA. The score plot for this transformation is shown in Figure 6(a) which clearly shows a difference between high and low PWV patients. The variables contributing the most to this separation are shown in the loading plot (Figure 6(b)) where, not surprisingly, it can be seen that PWV is one of the major contributors to the separation of the patients. Interestingly and in agreement with assessed data in this study, it is closely correlated with the elastic modulus of dehydrated layers. Furthermore, PCA on the data without the PWV variable shows similar separation between both high and low PWV patients and exhibits elastic modulus of the hydrated and dehydrated layers as three of the key variables to the separation (Figures 6(c) and 6(d)). The elastic modulus of hydrated media was closely related to age. In addition, the nanomechanical properties of dehydrated media and adventitia were closely correlated. Most SLRPs were closely grouped in the PCA analysis with some differences in mimecan and biglycan, which was similar to the PCA data of the adventitia.

4. Conclusions

This study probed the nanoscale stiffening-related ultrastructural changes in the tunica media of human IMAs in ambient

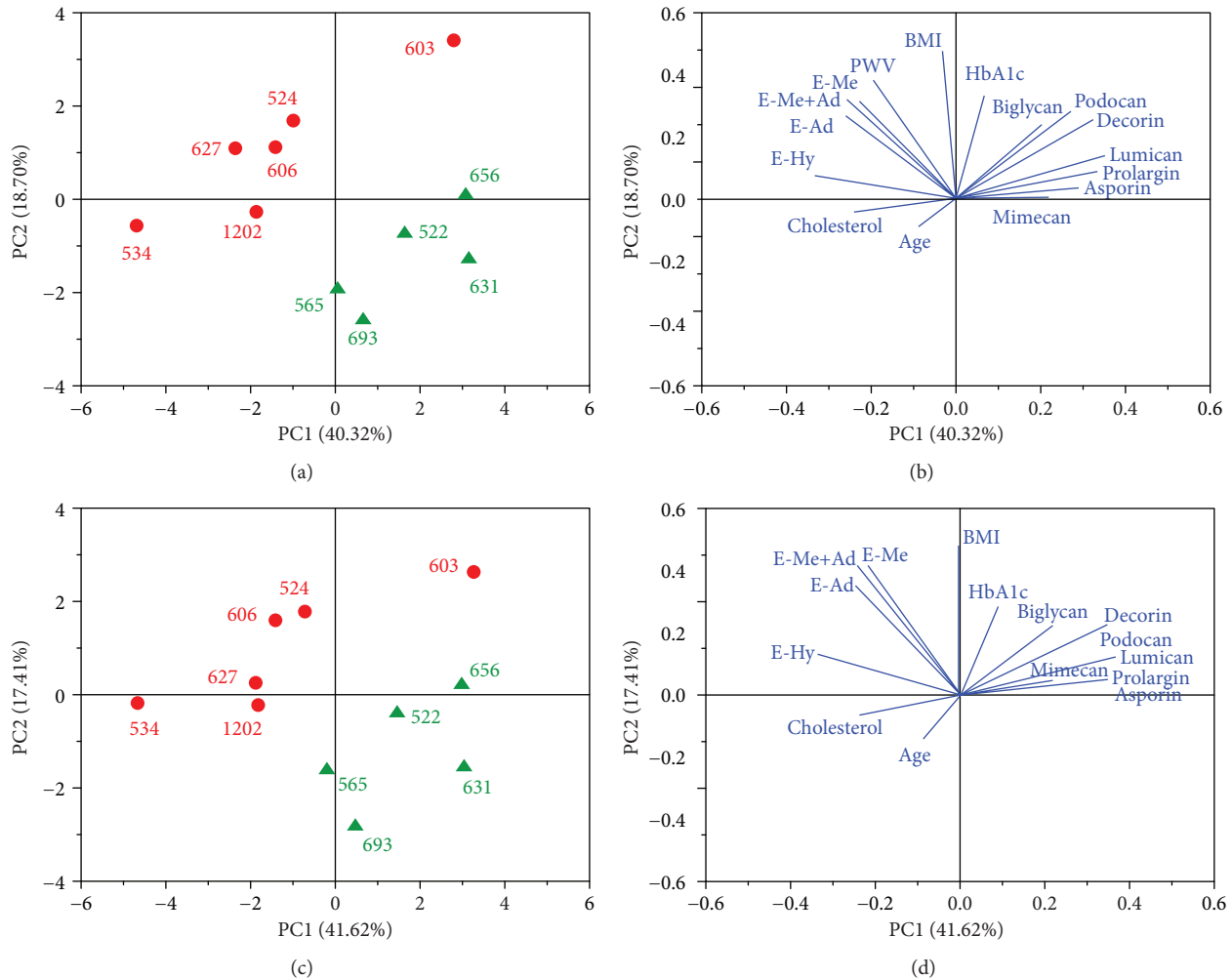


FIGURE 6: PCA of patient proteomics, quantitative metadata, and nanomechanical variables. (a) Score plot of the two first components. Each dot represents a patient. Patients colored by group (red - high PWV, green - low PWV). (b) Loading plot of (a) showing the variables that contribute the most of the structured observed in (a); PWV and elastic modulus of hydrated media (E-Hy), dehydrated media (E-Me), adventitia (E-Ad), and combined dehydrated media and adventitia (E-Me+Ad) are four of the most contributing variables to the separation between both groups. (c) Score plot of the two principal components of patient data without the PWV variable. Similar separation between both groups can be observed. (d) Loading plot of (c) shows that E-Hy, E-Me, E-Ad, and E-Me+Ad are four of the most contributing variables to the separation observed. E-Me and E-Ad were highly correlated. Of the SLRPs, mimecan presents the most contribution to the separation between groups observed.

and fluid conditions in patients with a high PWV. We show that PeakForce QNM can be used for mechanical property characterization of hydrated biological tissues. The study clearly demonstrates that AFM methods can be used as a tool for assessing arterial stiffness, with good agreement with expected trends based on *in vivo* measurements. The mechanical properties of the medial ultrastructure in both hydrated and dehydrated conditions correlated well with the carotid-femoral PWV. The AFM-derived nanomechanical properties were also correlated with SLRP expression, which is related to arterial stiffness. Based on the correlation tests, we suggest that the medial and adventitial layers are both suitable for AFM analysis to characterize nanoscale arterial stiffening. Overall, this study demonstrates the utility of AFM methods for arterial stiffening studies.

Data Availability

The Excel data used to support the findings of this study are included within the supplementary information file.

Conflicts of Interest

There are no conflicts of interest to declare.

Acknowledgments

Z.C is funded by the University of Liverpool/National Tsing Hua University Dual PhD scheme. RA is grateful to the Royal Academy of Engineering/Leverhulme Trust for a Senior Research Fellowship (LTSRF1617/13/76) and to the British

Heart Foundation (PG/16/107/32681). The authors (ZC and PYC) sincerely thank the financial support from the Ministry of Science and Technology, Taiwan (MOST105-2221-E-007-012-MY4 and MOST107-2218-E-007-049), and High Entropy Materials Center (MOST107-3017-F-007-003). The authors would like to thank Ahmed Kazaili and Zhuola (School of Engineering, University of Liverpool) for assistance with collecting AFM force-indentation curves.

Supplementary Materials

The supplementary material is simply the raw data in an Excel spreadsheet in accordance with the journal's "Data Availability" policy. (*Supplementary Materials*)

References

- [1] Z. Chang, P. Paoletti, S. D. Barrett et al., "Nanomechanics and ultrastructure of the internal mammary artery adventitia in patients with low and high pulse wave velocity," *Acta Biomaterialia*, vol. 73, pp. 437–448, 2018.
- [2] C. Palombo and M. Kozakova, "Arterial stiffness, atherosclerosis and cardiovascular risk: pathophysiologic mechanisms and emerging clinical indications," *Vascular Pharmacology*, vol. 77, pp. 1–7, 2016.
- [3] H. K. Graham, R. Akhtar, C. Kridiotis et al., "Localised micro-mechanical stiffening in the ageing aorta," *Mechanisms of Ageing and Development*, vol. 132, no. 10, pp. 459–467, 2011.
- [4] R. Akhtar, H. K. Graham, B. Derby et al., "Frequency-modulated atomic force microscopy localises viscoelastic remodelling in the ageing sheep aorta," *Journal of the Mechanical Behavior of Biomedical Materials*, vol. 64, pp. 10–17, 2016.
- [5] A. W. Chung, A. D. Booth, C. Rose, C. R. Thompson, A. Levin, and C. van Breemen, "Increased matrix metalloproteinase 2 activity in the human internal mammary artery is associated with ageing, hypertension, diabetes and kidney dysfunction," *Journal of Vascular Research*, vol. 45, no. 4, pp. 357–362, 2008.
- [6] A. J. Engler, L. Richert, J. Y. Wong, C. Picart, and D. E. Discher, "Surface probe measurements of the elasticity of sectioned tissue, thin gels and polyelectrolyte multilayer films: correlations between substrate stiffness and cell adhesion," *Surface Science*, vol. 570, no. 1–2, pp. 142–154, 2004.
- [7] A.-S. A. Faarvang, S. A. Rørdam Preil, P. S. Nielsen, H. C. Beck, L. P. Kristensen, and L. M. Rasmussen, "Smoking is associated with lower amounts of arterial type I collagen and decorin," *Atherosclerosis*, vol. 247, pp. 201–206, 2016.
- [8] S. A. R. Preil, L. P. Kristensen, H. C. Beck et al., "Quantitative proteome analysis reveals increased content of basement membrane proteins in arteries from patients with type 2 diabetes mellitus and lower levels among metformin users," *Circulation: Cardiovascular Genetics*, vol. 8, no. 5, pp. 727–735, 2015.
- [9] M. Lyck Hansen, H. C. Beck, A. Irmukhamedov, P. S. Jensen, M. H. Olsen, and L. M. Rasmussen, "Proteome analysis of human arterial tissue discloses associations between the vascular content of small leucine-rich repeat proteoglycans and pulse wave velocity," *Arteriosclerosis, Thrombosis, and Vascular Biology*, vol. 35, no. 8, pp. 1896–1903, 2015.
- [10] K. Sweers, K. Van Der Werf, M. Bennink, and V. Subramaniam, "Nanomechanical properties of α -synuclein amyloid fibrils: a comparative study by nanoindentation, harmonic force microscopy, and Peakforce QNM," *Nanoscale Research Letters*, vol. 6, no. 1, p. 270, 2011.
- [11] F. Eghiaian, A. Rigato, and S. Scheuring, "Structural, mechanical, and dynamical variability of the actin cortex in living cells," *Biophysical Journal*, vol. 108, no. 6, pp. 1330–1340, 2015.
- [12] A. L. Lavanya Devi, U. Nongthomba, and M. S. Bobji, "Quantitative characterization of adhesion and stiffness of corneal lens of *Drosophila melanogaster* using atomic force microscopy," *Journal of the Mechanical Behavior of Biomedical Materials*, vol. 53, pp. 161–173, 2016.
- [13] G. Pletikapić, A. Berquand, T. M. Radić, and V. Svetličić, "Quantitative nanomechanical mapping of marine diatom in seawater using peak force tapping atomic force microscopy," *Journal of Phycology*, vol. 48, no. 1, pp. 174–185, 2012.
- [14] V. R. Adineh, B. Liu, R. Rajan, W. Yan, and J. Fu, "Multidimensional characterisation of biomechanical structures by combining atomic force microscopy and focused ion beam: a study of the rat whisker," *Acta Biomaterialia*, vol. 21, pp. 132–141, 2015.
- [15] T. J. Young, M. A. Monclus, T. L. Burnett, W. R. Broughton, S. L. Ogin, and P. A. Smith, "The use of the PeakForce™ quantitative nanomechanical mapping AFM-based method for high-resolution Young's modulus measurement of polymers," *Measurement Science and Technology*, vol. 22, no. 12, article 125703, 2011.
- [16] M. Papi, P. Paoletti, B. Geraghty, and R. Akhtar, "Nanoscale characterization of the biomechanical properties of collagen fibrils in the sclera," *Applied Physics Letters*, vol. 104, no. 10, article 103703, 2014.
- [17] The Reference Values for Arterial Stiffness' Collaboration, "Determinants of pulse wave velocity in healthy people and in the presence of cardiovascular risk factors: 'establishing normal and reference values'," *European Heart Journal*, vol. 31, no. 19, pp. 2338–2350, 2010.
- [18] D. Sicard, L. E. Fredenburgh, and D. J. Tschumperlin, "Measured pulmonary arterial tissue stiffness is highly sensitive to AFM indenter dimensions," *Journal of the Mechanical Behavior of Biomedical Materials*, vol. 74, pp. 118–127, 2017.
- [19] C. A. Grant and P. C. Twigg, "Pseudostatic and dynamic nanomechanics of the tunica adventitia in elastic arteries using atomic force microscopy," *ACS Nano*, vol. 7, no. 1, pp. 456–464, 2012.
- [20] P. Talusan, S. Bedri, S. Yang et al., "Analysis of intimal proteoglycans in atherosclerosis-prone and atherosclerosis-resistant human arteries by mass spectrometry," *Molecular & Cellular Proteomics*, vol. 4, no. 9, pp. 1350–1357, 2005.
- [21] J. Barallobre-Barreiro, A. Didangelos, F. A. Schoendube et al., "Proteomics analysis of cardiac extracellular matrix remodeling in a porcine model of ischemia/reperfusion injury," *Circulation*, vol. 125, no. 6, pp. 789–802, 2012.
- [22] M. Onda, T. Ishiwata, K. Kawahara, R. Wang, Z. Naito, and Y. Sugisaki, "Expression of lumican in thickened intima and smooth muscle cells in human coronary atherosclerosis," *Experimental and Molecular Pathology*, vol. 72, no. 2, pp. 142–149, 2002.
- [23] H. J. Zhang, J. Wang, H. F. Liu, X. N. Zhang, M. Zhan, and F. L. Chen, "Overexpression of mimecan in human aortic smooth muscle cells inhibits cell proliferation and enhances apoptosis and migration," *Experimental and Therapeutic Medicine*, vol. 10, no. 1, pp. 187–192, 2015.

- [24] B. Fernández, A. Kampmann, F. Pipp, R. Zimmermann, and W. Schaper, "Osteoglycin expression and localization in rabbit tissues and atherosclerotic plaques," in *Vascular Biochemistry*, P. Zahradka, J. Wigle, and G. N. Pierce, Eds., vol. 41 of *Molecular and Cellular Biochemistry: An International Journal for Chemical Biology in Health and Disease*, pp. 3–11, Springer, Boston, MA, USA, 2003.
- [25] R. Shimizu-Hirota, H. Sasamura, M. Kuroda, E. Kobayashi, M. Hayashi, and T. Saruta, "Extracellular matrix glycoprotein biglycan enhances vascular smooth muscle cell proliferation and migration," *Circulation Research*, vol. 94, no. 8, pp. 1067–1074, 2004.
- [26] J. W. Fischer, S. A. Steitz, P. Y. Johnson et al., "Decorin promotes aortic smooth muscle cell calcification and colocalizes to calcified regions in human atherosclerotic lesions," *Arteriosclerosis, Thrombosis, and Vascular Biology*, vol. 24, no. 12, pp. 2391–2396, 2004.